Design, Construction, Calibration and Testing of a Wind Tunnel Force Balance

André Filipe Rocha Oliveira

Thesis to obtain the Master of Science Degree in

Aerospace Engineering

Supervisors: Prof. André Calado Marta
Eng. João Pedro Ribeiro Marques

Examination Committee

Chairperson: Prof. Filipe Szolnoky Ramos Pinto Cunha
Supervisor: Prof. André Calado Marta
Member of the Committee: Prof. Virgínia Isabel Monteiro Nabais Infante

September 2020

Dedicated to what seems impossible.

Acknowledgments

Firstly, I would like to express my profound gratitude to Professor André Calado Marta, for this amazing subject and all the support and guidance during this thesis. It was a privilege to share my work with the most dedicated and enthusiastic Professor I have ever meet. May he continue to inspire many students.

Thanks to engineer João Marques for all the support during instrumentation and all the wise advice in programming and using of sensors. Also, thanks to Professors and PhD students of Laboratório de Ensaios Mecânicos e de Materiais of the mechanical department for the use of facilities and equipment.

A special word to João and Pedro, the supervisors of Laboratório de Técnicas Oficinais, for all their support and guidance in construction and assembly of components and their patience when I used the machinery. Without them, the project would remain on paper.

To all the friends that I met in Lisbon and especially to my técnico colleagues for the long walk side by side passing all the problems together and for making me grow intellectually. Thanks for the support even when our path was divided into the master's thesis and despite your endless work, the time spent beside me is priceless.

To my family, for the love, kindness and presence throughout my academic life and all the happiness they manifest when I briefly explained my confuse work to them. Their motivation and help made me raise and continue in my worst moments.

To my Porto friends, for the care and concern in my work during my absence and for being distant but present when I need to.

Resumo

Atividades experimentais são essenciais na indústria aeroespacial, sendo os tuneis de vento o equipamento mais utilizado para a validação de conceitos e projetos. Neste contexto, este trabalho tem como objetivo dotar o túnel de vento do Laboratório de Engenharia Aeroespacial do Instituto Superior Técnico com uma balança aerodinâmica capaz de medir forças e momentos.

O projeto da balança foi adaptado de um dimensionamento já existente segundo uma plataforma de *Stewart*, mas reajustado para as necessidades atuais. A modelação e validação do projeto mecânico foi feita inicialmente de forma computacional usando o *SolidWorks*®, sendo procedido alguns testes experimentais para verificação.

Além da construção, também foi feita a instrumentação da balança para medir forças e momentos das atividades experimentais, e outras grandezas adicionais, tais como velocidade, temperatura e atitude. Para tal, foram usados extensómetros e outros sensores, e um interface com o utilizador em *LabVIEW*™ foi criado para visualização em tempo real e gravação dos resultados.

Para tornar as medições da balança fiáveis, foi executada uma calibração estática onde são relacionadas cargas conhecidas com a resposta dos extensómetros. Usando estes dados e o método dos mínimos quadrados com um polinómio de segundo grau, uma matriz de coeficientes de calibração foi obtida para as componentes aerodinâmicas.

Por fim, foi realizado um ensaio experimental com um modelo da asa traseira de um carro de corrida para confirmar a otimização de C_L/C_D quando usado placas laterais de perfil curvas em vez de perfil reto. A influência da velocidade no desempenho da asa traseira é também analisada e é feita uma comparação com o CFD.

Palavras-chave: Túnel de vento, Balança de força aerodinâmica, Projeto mecânico, Sensores e instrumentação, Calibração, Ensaios experimentais

Abstract

Experimental activities are essential in the aerospace industry, with wind tunnels being the most used devices in the validation of concepts and design. Therefore, this work aims to endow the Aerospace Engineering Laboratory at Instituto Superior Técnico with an aerodynamic balance capable of measuring forces and moments.

The balance follows an existing *Stewart* platform configuration design, here readjusted to the current requirements. The design and validation of mechanical performance were initially done computationally using *SolidWorks*®, then some experimental tests were performed for verification.

In addition to the construction, the instrumentation of the balance was necessary to compute forces and moments, as well as additional quantities for the tests, such as speed, temperature and attitude. To this end, strain gauges and several sensors were studied and implemented. The balance user interface was done in *LabVIEW*™.

To make the balance as accurate as possible, a static calibration was performed to relate the application of well-known loads on the balance with the response of the strain gauges. This way, it was possible to obtain a matrix with calibration coefficients for all aerodynamic components using the collected data and the least squares method with a second-order polynomial.

Finally, an experimental test was performed with a model of the rear wing of a racing car to confirm the optimisation in C_L/C_D when using endplates with a curved profile instead of a flat profile. The influence of velocity in the rear wing performance was also analysed and a comparison with CFD was carried out.

x

Contents

List of Tables

List of Figures

Nomenclature

Greek symbols

α Angle of attack.

β Angle of side-slip.

δ_a Deflection of aileron.

δ_c Deflection of elevator.

δ_r Deflection of rudder.

δ_t Engine throttle.

ϵ Strain.

θ Pitch angle.

θ_y Variation of the angle of attack.

θ_z Variation of the side-slip angle.

μ Dynamic viscosity.

ρ Density.

ρ_w Resistivity of wire.

σ Stress.

σ_i Standard deviation.

ϕ Roll angle.

χ^2 Chi-square.

χ_v^2 Reduced chi-square.

ψ Yaw angle.

Roman symbols

A Cross-section area.

a	Speed of sound.
AR	Aspect ratio.
b	Wing span.
C	Calibration coefficients matrix.
c	Wing chord.
C_D	Coefficient of drag.
C_L	Coefficient of lift.
C_m	Coefficient of moment.
C_{fix}	Constant of column fixation conditions.
D	Sensitivity coefficients matrix.
D_t	Outer diameter of a tube.
d_t	Inner diameter of a tube.
E	Young's modulus.
F	Matrix of the aerodynamic components.
$\hat{F}$	Matrix of estimated aerodynamic components.
Fr	Froude number.
f_i	Aerodynamic components.
$\hat{f}_i$	Estimated aerodynamic components.
f_w	Wind tunnel inverter frequency.
F_X	Stream line force.
F_Y	Side force.
F_Z	Vertical force.
g	Acceleration of gravity.
I	Area moment of inertia.
k	Strain gauge factor.
l	Characteristic length.
L, M, N	Aerodynamic Moments.
Ma	Mach number.

m Number of parameters to be fitted.

M_X Stream line moment.

M_Y Side moment.

M_Z Vertical moment.

N Number of sets of applied loads.

p, q, r Components of angular velocity.

p_0 Stagnation or total pressure.

p_s Static pressure.

P_{Cr} Critical force to occur buckling.

R Readings matrix.

Re Reynolds number.

R_g Strain gauge eletrical resistance.

$R_{specific}$ Specific gas constant.

S Wing area.

ssE Sum of squares errors.

u, v, w Velocity Cartesian components.

V Velocity Modulus.

V_R Uncertainties in the readings matrix.

V_s Sensor power voltage.

V_W Uncertainties of applied loads matrix.

v_w Wind tunnel airspeed.

V_{max} Maximum voltage.

V_{out} Output voltage.

V_{pp} Voltage peak-to-peak.

W Weighting matrix.

X, Y, Z Aerodynamic Forces.

Subscripts

i Aerodynamic components.

x, y, z Cartesian components.

Superscripts

T   Transpose.

Glossary

ADC	Analog to Digital Conversion
CAD	Computer-Aided Design
CFD	Computational Fluid Dynamics
CRM	Common Research Model
DAQ	Data Acquisition System
DOF	Degrees of freedom
FEA	Finite Elements Analyses
FEM	Finite Elements Method
FST	Formula Student Técnico
IMU	Inertial Measurement Unit
LTO	Laboratório de Técnicas Oficinais
PIV	Particle Image Velocimetry
SSL	Standard Sea Level
Técnico	Instituto Superior Técnico
UAV	Unmanned Aerial Vehical

Chapter 1

Introduction

1.1 Motivation

Aviation is one of the most reliable industries and service providers. This is only possible due to the remarkable work done by scientists and aeronautical engineers. It was never been an easy task, since aeronautics is based on a very complex multidisciplinary science. However, nowadays it is almost impossible to live without it. Transport of people and trading of merchandise are some examples of services highly dependent on aviation.

The consequences of an aerial malfunction may cause a big impact. No wonder that aviation is an industry with so extensive research. The development and improvement of aeronautical technologies are responsible for creating almost flawless machines. Theoretical background is used to support new concepts. Validations are the confirmation that the new concepts are feasible. Aeronautical validations take the form of computational analyses or experimental tests.

The wind tunnels are, without any doubt, the most used facilities for experimental tests. A scale model of an aircraft or a component, such as a wing, is used in wind tunnel tests. In these facilities, the scale model is subjected to an air flow. From this interaction, forces, moments, pressures, flow visualisations and others can be obtained as a result. This data is processed in terms of dynamic and stability of the model.

Just as the wind tunnels are the most common tests facilities, the aerodynamic force balance is the most well-known test instrument. Since forces and moments are common quantities to measure in a wind tunnel, it is almost inevitable to find an aerodynamic force balance in wind tunnels facilities.

The scale models are trustworthy reproductions of common size aircrafts or space vehicles. The use of a small-scale model instead of the real object is mostly justified by the easiness of obtaining results for more handleable pieces. Nevertheless, some aerial vehicles are small by themselves so that a small-scale model is not required, such as small unmanned aerial vehicle (UAV). The real scale prototype of a small UAV is suitable for a standard wind tunnel.

The wind tunnel installed in the Aerospace Engineering Laboratory at Instituto Superior Técnico (Técnico) currently lacks readily available instrumentation. As such, the motivation of this thesis is to

provide capability of measuring aerodynamic forces by developing an aerodynamic force balance capable of running out experimental tests. This way, the Técnico wind tunnel will be upgraded to supply a higher variety of experimental tests to the student and research activities. Currently, the aerospace engineering students association is involved in national and international aeronautical projects but, unfortunately, cannot properly leverage the existing facilities. The same is true for the aeronautical research community in Técnico.

1.2 Aircraft Design, Scaling and Testing

An aircraft is more than a vehicle of transportation. It is a refined piece of engineering with more than one hundred years of evolution. Since the first sketch introduced by the Wright brothers, a lot of changes in aircraft design have occurred.

Aircraft design is understood to be a mental process in which the designer tries to project his idea of an aircraft. Sometimes aircraft design is a little bit detached from purely analytical disciplines, such as aerodynamics, structures, control and propulsion, and it may start with an experienced person who idealises a new concept based on his entire background. New designs need to be well analysed and sized to accomplish the intention of its creation, satisfying certain requirements demanded by the customer. This makes aircraft design an iterative process, as the "design wheel" in Figure 1.1 tries to depict [1].
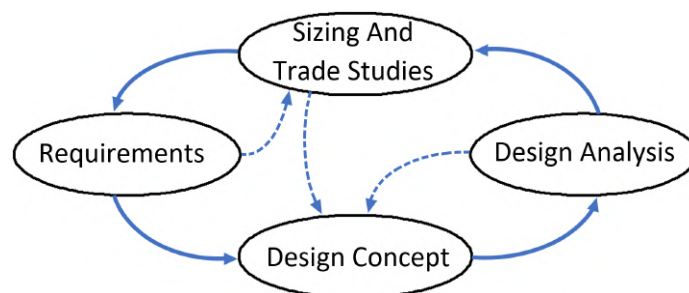
Figure 1.1: The design wheel. Adapted from [1].

Aircraft design is constituted by three phases: conceptual design, preliminary design and detailed design. The first phase gives a shell and a size to the aircraft, in which the aircraft configurations are selected to achieve the requirements. The next phase is the validation of the adopted configurations, in which, specialists in aerodynamics, propulsion and control systems come up to analyse their portion of the aircraft, typically performing many computational and experimental analyses. The last phase is the full concretization of the aircraft, in which all components of the aircraft are designed and validated, including the definition of the processes of production, materials and tools [1] .

Simulations become a crucial step in transforming an idea into reality. There are some different types of simulations which can be adopted to achieve the requirements, which can be grouped into two categories: numerical and experimental.

If some analyses of the aircraft are to be done numerically, a mathematical model is required. The information drawn is highly dependent on the mathematical modelling and the numerical methods used

to obtain a solution. The task of building equipment and performing tests is eliminated but a lot of assumptions and approximations are required. The attainment and interpretation of numerical results, therefore, requires high expertise on the subject at hand [2].

Regarding simulations in aeronautics, aerodynamics is one of the largest fields of study. The best way to understand aerodynamic phenomena is the combination of theoretical background, computational analyses and experimental testing, see Figure 1.2. Nowadays, the first stages of aircraft design deeply involve computational fluids dynamics (CFD) to provide a trustworthy first dimensioning [3].
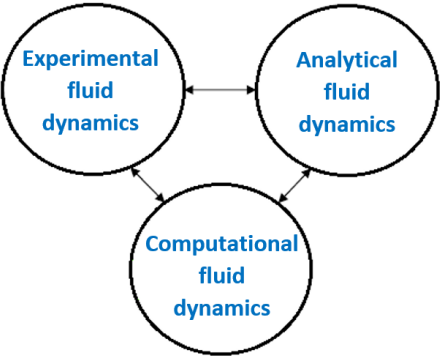
Figure 1.2: The three basic approaches to solve problems in fluid dynamics and heat transfer [4].

CFD simulations use numerical methods to solve fluid governing equations applied to a physical domain through some form of discretization, *finite-volume* and *finite-element* are commonly used. The mesh creation is an additional task whose complexity depends on the geometry under study. Figure 1.3 shows a mesh applied to a wing and engine structure of a aircraft.
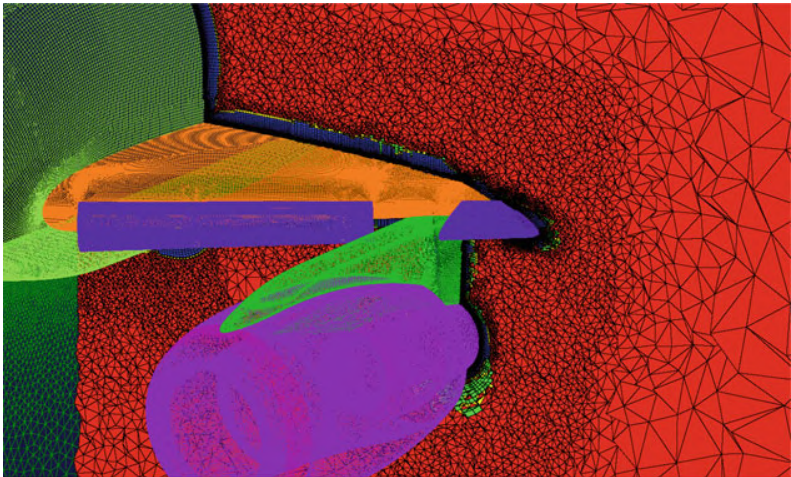
Figure 1.3: Multi-element grid with hexahedral, prism, pyramid and tetrahedral elements [5].

CFD has incremented accuracy and reliability in its results with the rapid growth of computational capabilities. However, the CFD analysis has a deviation compared with experimental tests, Figure 1.4 shows the comparison between experimental tests and computational simulations for force and moment of a common research model (CRM) aircraft. Some applications where CFD still remains a relatively primitive state of development, experiment-based approach remains the primary source of information especially when complex flows such as high-lift devices, shock waves or flow separation [4]. For this

3

reason, the experimental tests are required on aerodynamic analysis and CFD is a proper tool to complement them [5].
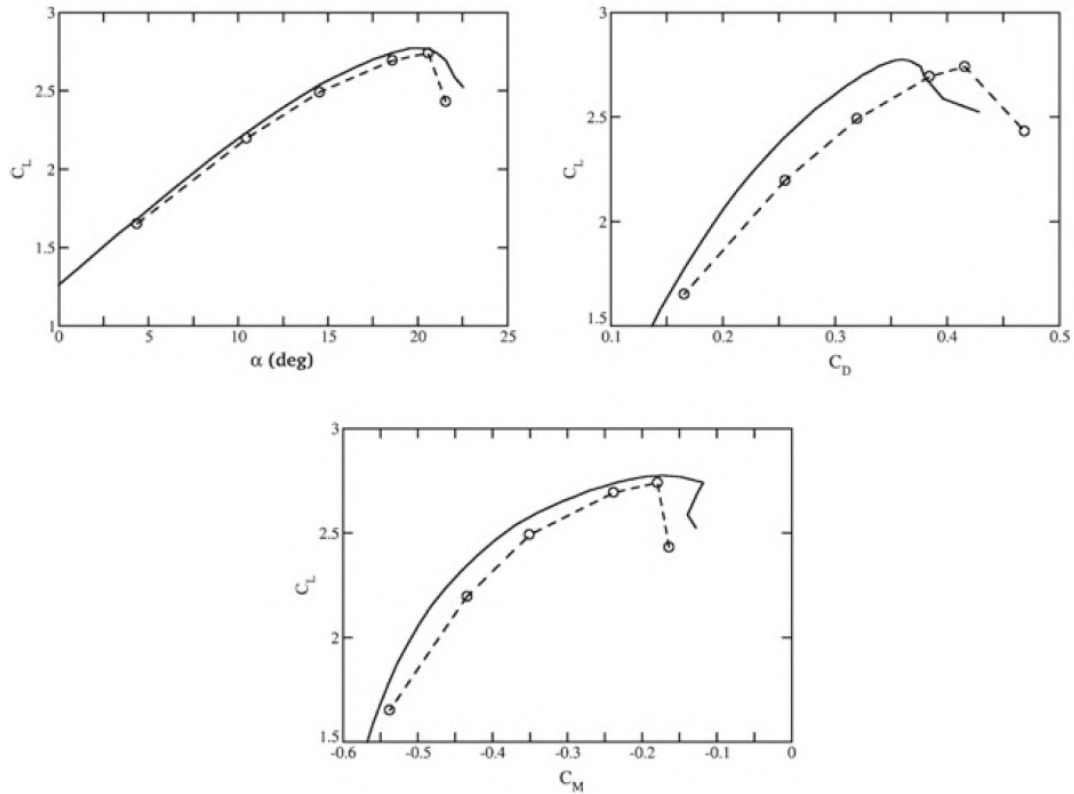
Figure 1.4: Force and moment comparison between experimental (–) and computational ($\circ - \circ$) for a CRM aircraft [5].

Experimental testing analyses a similar physical model which better suits a set of constraints. The model used is similar in appearance and proportions to the prototype but not identical. Normally, the model is smaller than the prototype, but being larger may also be advantageous. With a similar model approach, complex problems can easily studied. As problems become more complex, the experimental analyses of similar models gain more relevance than numerical approaches and mathematical models. The drawbacks of experimental analyses include high costs of infrastructure, the need of experimental expertise and limited applicability [2].

Experimental testing provides final validation. To that end, a wind tunnel, such as the one shown in Figure 1.5, is crucial in experimental analyses that provides invaluable information for the simulation of real flows at reduced scale [3] [4].

Wind tunnels can simulate incompressible subsonic, transonic supersonic and hypersonic flow velocities. The test section can accommodate a scale model of aircraft and spacecraft. It can also be used to test structures out of the aerospace range, such as buildings, cars or atmospheric phenomena. Studies in wind tunnels are related with turbulence, aerodynamic forces, pressure fields, buffeting, flutter, among others [6]. Shown in Figure 1.6 (a), a racing car model is assembled in a wind tunnel test section. The implemented models are adapted regarding the selected analysis to optimise resources. The size is the most common adaptation but also geometry adaptations are often implemented. For instance, the use

Figure 1.5: Example of a wind tunnel. Courtesy of Aerolab.

of an half aircraft model instead of a full aircraft model, see Figure 1.6 (b).

(a) Formula 1 car model. Courtesy of Sauber F1 Team.

(b) Aircraft half model. Courtesy of ONERA.

Figure 1.6: Models installed in a wind tunnel test section.

Using scale models also has other advantages, in particular [6]:

- The scaled models allows transformation of large systems into a system of manageable proportions for direct experimentation;

- The scale models reduces the experimentation time and promotes a deeper understanding of the desirable phenomenon;

- Some times deep understanding of physical phenomena requires experimental testing. Often, this methodology is the first step for feasible mathematical modelling.

1.3   Objectives and Deliverables

As demonstrated previously, wind tunnels are one of the most important experimental facilities, and an aerodynamic force balance is an essential instrument in aeronautical tests.

The main goal of this thesis is to provide the Aerospace Engineering Laboratory wind tunnel with an aerodynamic force balance, as well as, a procedure to run an experiment with it. The force balance needs to be able to obtain the three components of the aerodynamic forces (vertical, horizontal and lateral) and the aerodynamics moments (pitch, roll and yaw). In addition, other quantities will be provided by other complementing sensors, such as speed, temperature, humidity and model attitude.

To achieve the desirable force balance, all the process stages need to be overcome, ranging from design to testing, with some intermediate steps. After introduced a suitable design to the mechanical requirements, manufacture and assembly is mandatory, as well as the development and coupling of instrumentation. In order to the force balance provide trustfully data, calibration is introduced to consolidate the process.

The deliverables of this project are the following:

- Fully operational aerodynamic force balance capable of measuring the six aerodynamic components and being installed in the Aerospace Engineering Laboratory wind tunnel;
- Additional instrumentation to measure speed, temperature, humidity and testing model attitude;
- An user interface to visualise and record instrumentation data and provide the six aerodynamic components processed through the results of the performed calibration;
- Complete guide for setting up and operating the force balance during aerodynamic tests.

1.4 Thesis Outline

This thesis is divided in 8 chapters, including introduction, and structured as follows:

Chapter 2: State of The Art describes wind tunnels and force balances, introducing concepts related to experimental tests. This chapter contains also theoretical background about aerodynamics stability;

Chapter 3: Mechanical Design introduces the requirements of the force balance and details the facilities. The force balance structure is designed, finite elements analyses are performed, and an experimental test is carried out to validate the requirements;

Chapter 4: Instrumentation reveals all the purchased instruments to measure the quantities of study and all the development made to employ each sensor and integrate them. A calibration of each sensing bar strain gauge system is performed. The user interface is presented;

Chapter 5: Manufactured and Assembly presents all the selected materials and tasks to manufacture individual components and further assembly of the force balance, including instrumentation. The cost breakdown of the force balance is also presented;

Chapter 6: Calibration presents the methodology to calibrate the reading strain values of the sensing bars with the six aerodynamics components. The calibration is conducted through an experimental procedure;

Chapter 7: Testing exhibits the procedure guide and the required apparatus to conduct an experimental test with the aerodynamic force balance. An experimental test of a racing car rear wing model is performed;

Chapter 8: Conclusions presents the the overall conclusions and introduces future work to improve the aerodynamic force balance and its use.

Chapter 2

State of The Art

2.1 Wind Tunnels

In a wind tunnel, air and aircraft change the roles once assumed in flight. Instead of having the aircraft moving in the air, the aicraft is fixed and the air forced to move around it. An adequately scaled model, corresponding to an aerodynamically equivalent aircraft, can be used in wind tunnels.

The conditions of operation in wind tunnel are set to reproduce the same results as those obtained in real aircraft operation. To guarantee this, it is necessary to analyse non-dimensional fluid motion equations. The equations are used to provide the dimensionless relations between the scale model and the normal size aircraft. Three dimensionless coefficients are found: the Reynolds number (Re), the Mach number (Ma) and the Froude number (Fr) [3]. These parameters provide relations between the main causes of force in the flow: viscosity, inertia, elasticity and gravity,

$$Re = \frac{\rho v l}{\mu} = \frac{inertial\ forces}{viscous\ forces} \tag{2.1}$$

$$Ma = \frac{v}{a} = \frac{inertial\ forces}{elastic\ forces} \tag{2.2}$$

$$Fr = \sqrt{\frac{v^2}{lg}} = \sqrt{\frac{inertial\ forces}{gravitational\ forces}} \tag{2.3}$$

where l represents the characteristic length in m, v the velocity of the body in m/s, ρ the air density in kg/m^3, μ the coefficient of dynamic viscosity in kg/(m.s), a the speed of sound in m/s and g the acceleration of gravity in m/s^2.

There are many different variations of wind tunnels. They can be divided into two main groups: the open air circuit and the closed air circuit.

The test section can also be an open or a closed section, but the most common test section is the closed one.

(a) Open.	(b) Closed.
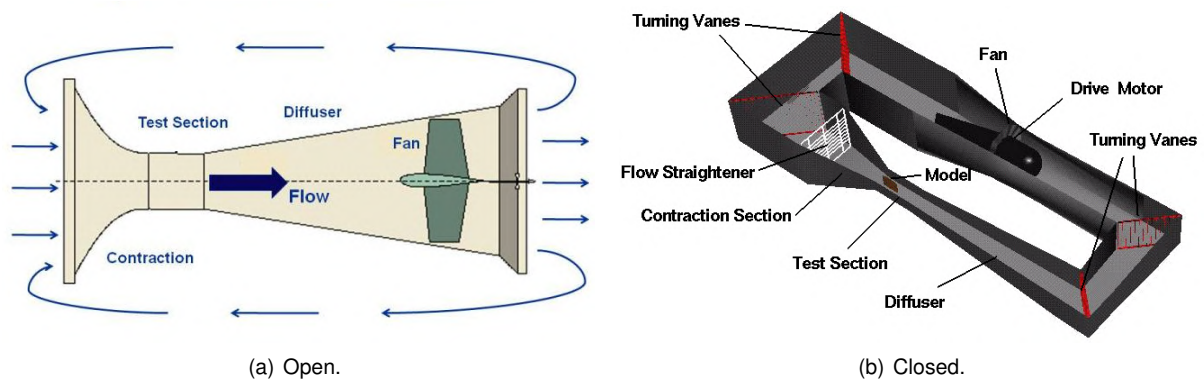
Figure 2.1: Types of wind tunnel air circuit. Courtesy of NASA.

2.1.1 Open Circuit Wind Tunnel

The open circuit wind tunnel does not have re-circulation of air. This type of wind tunnel is constituted by an entrance, a test section, a diffuser, a fan section and an exhaust. The adjustment of the fan speed changes the flux of intake air, allowing different flow speed settings. The air enters from an open area and exited to another open area. The scheme of an open air circuit is represented in Figure 2.1 (a).

These wind tunnels have the major advantage of lower acquisition cost by requiring less material and by this construction being easier than the closed circuit wind tunnel. It is also an advantage of this wind tunnel the exhaust to the atmosphere. Some tests, such as smoke tests and combustion engine tests, are even simpler in these wind tunnels because a purge is not necessary.

Some disadvantages of this type are the need of assurance of the air quality of the flow at the entrance since outside atmospheric conditions need to be taken into account, higher energy costs because it is necessary to accelerate the flow constantly, and noise. Open circuit wind tunnels are used in academical environments due to the inherent advantages and disadvantages [3].

2.1.2 Closed Circuit Wind Tunnel

Closed circuit wind tunnels have a re-circulation of air, with little or no air exchange with the exterior. This means the air runs along a circuit when the tunnel is operating. A scheme of the closed circuit wind tunnel is represented in Figure 2.1 (b).

The advantages of this type of tunnels are the quality of the flow where the use of vanes and screens results in more laminar flow, less energy necessary for operation so it is a cost effective for a high number of tests, and reduced noise.

The disadvantages are the higher acquisition costs of the tunnel and the necessity of a purge to run smoke and engine tests. Another disadvantage is the confines air temperature increase in normal operation making cooling often required [3].

2.1.3 Wind Tunnel Tests

Wind tunnel testing can be grouped into three major divisions: pressure, force and visualisation.

In pressure tests, intakes are placed around the model surfaces. With pressure on several points of the model, aerodynamic forces can be estimated.

In some cases, the forces and moments applied to the model can be measured directly using a device called force balance. The forces can be computed in a variety of ways, such as by measuring the angles of displacement and treat them with mathematical models, or by measuring the strain of some elements in the balance structure which were designed for this purpose [7]. An example of a force balance to test a model is represented in Figure 2.2.

Figure 2.2: Aircraft model mounted on a force balance in wind tunnel tests. Courtesy of Boeing.

The flow visualisation is a technique much different from the other two. Such technique helps to understand how the flow behaves around the surfaces and visualise some particular phenomenon. It allows to visualise stagnation points, separation lines, location of boundary layer transition and separation zones. To produce an image, some materials are used: smoke, oils, tufts, lights and ultraviolet fluorescent photographs [7]. In Figure 2.3 (a) a test with tufts and oil is represented, and in Figure 2.3 (b) a smoke test. Through this technique, it is easy to identify at first look turbulence zones.
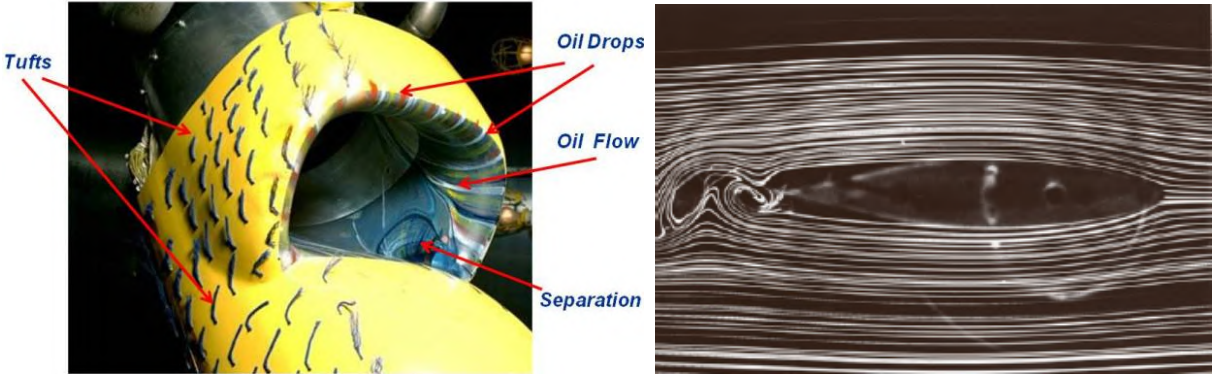
(a) Tufts and oil test in wind tunnel model. Courtesy of NASA.

(b) Smoke lines around a model airfoil in a low Reynolds-number wind-tunnel flow [7]

Figure 2.3: Wind tunnel types of visualisation tests.

A type of technique used to collect data from the flow visualisation is the *particle image velocimetry* (PIV), that requires the use of lasers and complex instruments to obtain an image of the flow. It is the only technique that allows one to obtain the velocity vectors and flow velocity fields. With the present technology, such as high resolution cameras and large processing devices, the captured images can

be computationally reproduced. A schematic representation of PIV apparatus is shown in Figure 2.4 (a). The advance introduced by these techniques is huge, allowing to compare the flow field obtained experimentally with the results obtained through CFD [8]. In Figure 2.4 (b), a velocity field at a trailing edge of a wing is represented.
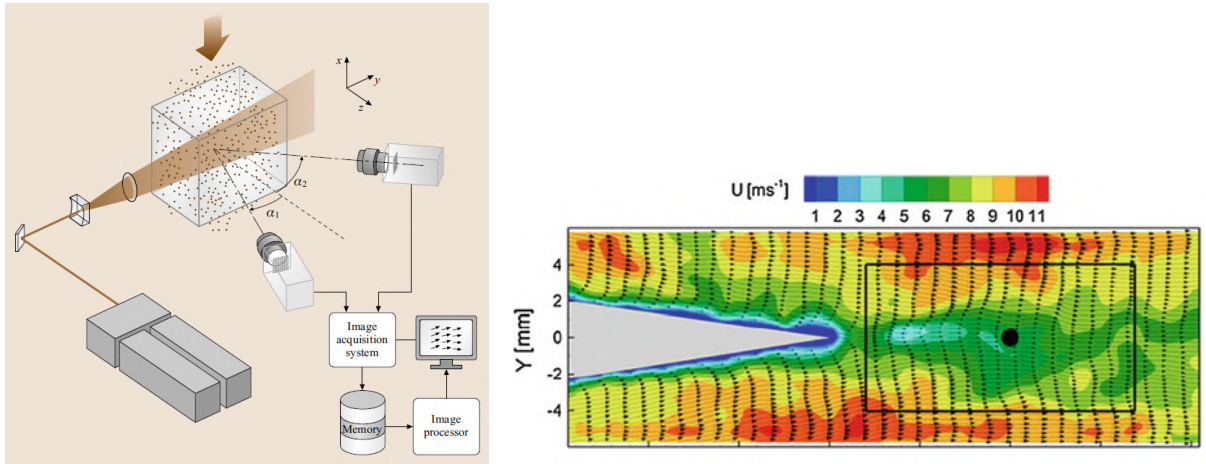
(a) Schematic of a typical PIV measurement system [7].

(b) Instantaneous velocity field at the trailing edge of a *NACA 0012* airfoil [8].

Figure 2.4: PIV apparatus and results.

For better results, it is common to apply more than one technique for the same experiment at a higher cost [3]. For instance, using an aerodynamic balance to obtain the forces and using PIV to obtain the behaviour of the flow around the model.

2.2   Wind Tunnel Force Balances

A force balance is a device that allows the measurement of forces and moments. It is very common to use this type of devices in wind tunnels to test scale models. A force balance should be able to provide trust-worthy data so good accuracy is necessary [3].

Two different configurations of force balance are widely used: internal and external. The difference between the two is the positioning of the model relative to the balance. External force balances are placed in the test section and the model is mounted over some part of the balance. Internal force balances are placed inside the model [9]. The size of the two balances are very different and the choice of one type may reside in this difference. The use of an internal force balance reduces the interference between the flow and supports. External force balances can produce more precise result due to its higher complexity. The two types of force balance use strain sensors in most part of the cases [7].

A set of components need to be considered in the apparatus to obtain results. One essential component is the extensometer that will measure the strain of a selected part due to the applied load. To process the output given by the extensometer, normally voltage, a data acquisition system is required. The data acquisition in collaboration with a conversion model converts strain to forces and moments. A schematic representation of this process to get the forces and moments using a force balance is represented in Figure 2.5.
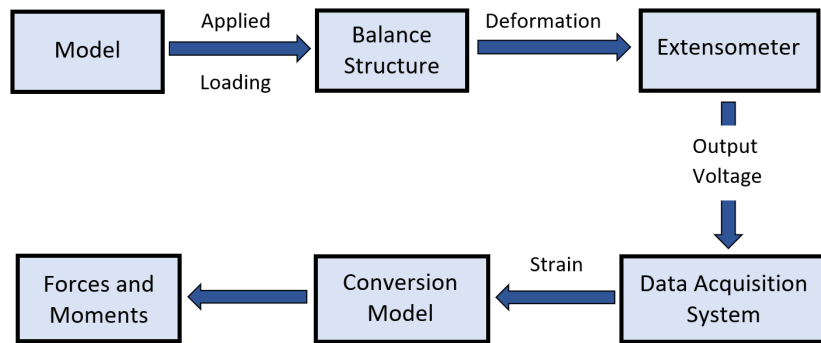
Figure 2.5: Schematic representation of the complete force balance measuring.

In general, force balances are constituted by two platforms which are connected by bars. The fixation between the bars and the platform is made by a spherical joints. This allows some movements in certain directions. The extensometers are installed on the bars, measuring theirs axial deformation.

To have a moving system with six degrees of freedom, three translations and three rotations, it is necessary to have 6 non collinear bars so that the six legs forces are linearly independent. The *Stewart* platform is a mechanism used in many cases, such as in flight simulators and wind tunnels experiments [10].

The *Stewart* platform features different configurations but the most common are the so-called 3-3, 3-6 and 6-6 formats, as represented in Figure 2.6.
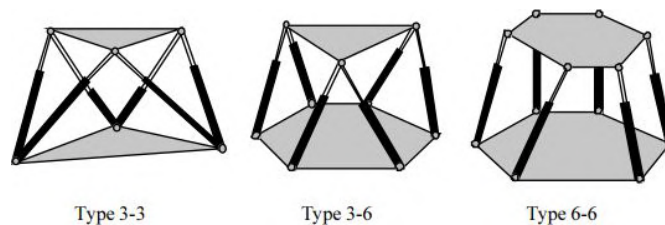
Figure 2.6: Types of *Stewart* platform [11].

The 3-3 format has triangular shapes in both platforms meaning that each vertex is connect to two bars. This introduces mechanical issues to the system due to the fact that there are two bars connected to each joint. The 3-6 format has a top platform with triangular shape and a bottom platform with hexagonal shape. Each vertex of the bottom base is connected to a bar and each vertex of the top base is connected to two bars. The 6-6 format has two hexagonal platforms being each vertex connected to each bar [11].

The configuration 3-3 and 3-6 carry the issue of a double spherical joint. This double joint is very hard to manufacture and ensuring no interference phenomena between the two bars connected to the joint is even more difficult. On the other hand, the 3-3 type is considered to be the most geometrically stable design. For these reasons, sometimes the double joint is split and the three sides platform is transformed into a kind of six sides platform, as seen in Figure 2.7. In this way the construction is more accessible and the balance stability is not compromised [12].

(a) 3-3 *Stewart* platform with double spherical joints.

(b) 6-6 *Stewart* platform based on the 3-3 platform.
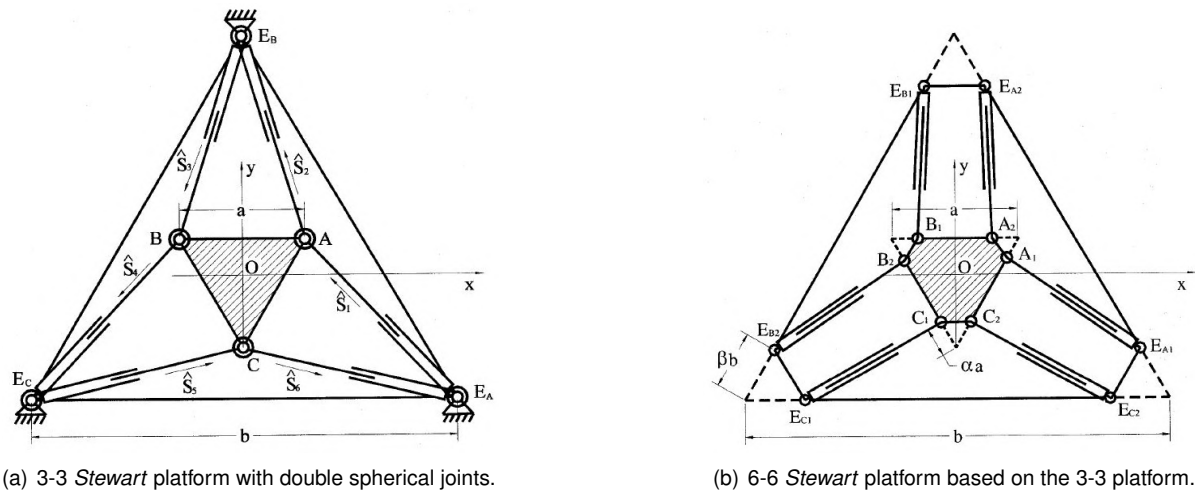
Figure 2.7: Transformation of a 3-3 *Stewart* into a 6-6 *Stewart* platform [12].

2.3 Aircraft Model

The physical system of an aircraft can be modelled trough the use of some state variables. The variables most common used are represented in Table 2.1.

Table 2.1: Variables used for describe aircraft motion

Forces		Moments		Angular velocities		Linear velocities	
X	Axial "drag" force	L	Rolling moment	p	Roll rate	u	Axial velocity
Y	Side force	M	Pitching moment	q	Pitch rate	v	Lateral velocity
Z	Normal "lift" force	N	Yawing moment	r	Yaw rate	w	Normal velocity

The variables are represented in the aircraft reference frame in Figure 2.8.
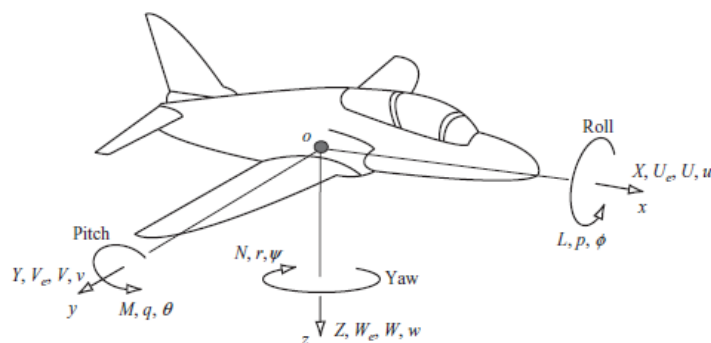
Figure 2.8: Aircraft reference frame.

We can note these total linear perturbations are given by the sum of steady equilibrium components (U,V,W) and transition perturbation components (u,v,w) [13].

Euler angles are associated with each axis of the model and define the attitude of the aircraft by comparing the angular orientation of the air-frame fixed axes with earth axes. The roll angle (ϕ) is related with the x axis, the pitch angle (θ) considers the rotation about the y axis and the yaw angle (ψ) rotation about the z axis.

2.3.1 Aircraft Aerodynamics, Stability and Control

The main forces applied on an aircraft are aerodynamics, gravitational and propulsive. A perturbation in forces and moments acting on the aircraft can be a direct response of a variation in the propulsion or the control surfaces. Some example of these surfaces are elevator, rudder and ailerons.

The forces and moments can be expressed as a function of state variables, such as linear velocities (u, v, w) and angular velocities (p, q, r). It is usual to convert this quantities into dimensionless [14].

Assuming the angles of attack and side-slip angle are small:

$$\beta = arcsin\frac{v}{V} \approx \frac{v}{V} = \hat{v} \qquad\qquad \alpha = arctan\frac{w}{V} \approx \frac{w}{V} = \hat{w}$$

where V is the velocity modulus.

Some models can be applied to a aircraft to describe the stationary states. It is common to separate an aircraft behaviour into two motions families, the longitudinal motion and the lateral motion.

Longitudinal motion is characterised by the motion without loss of symmetry in the x-z plane of the aircraft. The aerodynamic and control forces and moments related to longitudinal motion can be expressed in dimensionless form as [15]:

$$\begin{cases} C_x = C_{x_u}\hat{u} + C_{x_\alpha}\alpha + C_{x_q}\hat{q} + C_{x_{\hat{\alpha}}}\hat{\dot{\alpha}} + C_{x_{\delta_e}}\delta_e + C_{x_{\delta_t}}\delta_t \\ C_z = C_{z_u}\hat{u} + C_{z_\alpha}\alpha + C_{z_q}\hat{q} + C_{z_{\hat{\alpha}}}\hat{\dot{\alpha}} + C_{z_{\delta_e}}\delta_e + C_{z_{\delta_t}}\delta_t \\ C_m = C_{m_u}\hat{u} + C_{m_\alpha}\alpha + C_{m_q}\hat{q} + C_{m_{\hat{\alpha}}}\hat{\dot{\alpha}} + C_{m_{\delta_e}}\delta_e + C_{m_{\delta_t}}\delta_t \end{cases} \tag{2.4}$$

Taking as example C_{x_u}, which represents the dimensionless of the aerodynamic derivative for X. Force X can be express in dimensionless coefficient by $X = \frac{1}{2}\rho V^2 S C_x$ where S is the wing area. If the derivation is in order to u, this linear velocity must be dimensionless, $\hat{u} = \frac{u}{V}$. Therefore, $X_u = \frac{\partial X}{\partial u}$ is dimensionless in $C_{x_u} = \frac{\partial C_x}{\partial \hat{u}}$. The same methodology is applied to compute the others dimensionless aerodynamic coefficients. The detailed analysis which leads to equation system (2.4) can be reviewed in [15].

The longitudinal motion has two control inputs, the deflection of the elevator (δ_e) and the engine throttle (δ_t).

The lateral motion is characterised by a motion without loss of symmetry on the x-y plane of the aircraft. The aerodynamic and control forces and moments related to this motion can be described in dimensionless form as:

$$\begin{cases} C_y = C_{y_\beta}\beta + C_{y_p}\hat{p} + C_{y_r}\hat{r} + C_{y_{\delta_a}}\delta_a + C_{y_{\delta_r}}\delta_r \\ C_l = C_{l_\beta}\beta + C_{l_p}\hat{p} + C_{l_r}\hat{r} + C_{l_{\delta_a}}\delta_a + C_{l_{\delta_r}}\delta_r \\ C_n = C_{n_\beta}\beta + C_{n_p}\hat{p} + C_{n_r}\hat{r} + C_{n_{\delta_a}}\delta_a + C_{n_{\delta_r}}\delta_r \end{cases} \tag{2.5}$$

The aerodynamic derivatives to lateral motion follow the same process described for the longitudinal motion [15].

The control of the lateral motion is done using two surfaces, the rudder and the ailerons. The deflection angle of these two surfaces is represented by δ_r and δ_a respectively.

2.3.2 Aircraft System Identification

The aircraft derivatives can be determined with the use of experimental devices. This is very common because the models do not always provide the necessary data for a complete mathematical model of the aircraft [3]. A wind tunnel coupled with a force balance can be an useful apparatus to estimate the physical behaviour of a model. The amount of information given by a force balance depends on its complexity.

A study of the variation of moments and forces with respect to state variables can serve as a basis for computing important dimensionless parameters (such as coefficient of lift) and a step towards modelling the aircrafts behaviour. For instance, the derivative X_u can be calculated by varying the velocity u and measuring the response of the aircraft in terms of the force in X

$$X_u = \frac{\partial X}{\partial u} \approx \frac{\Delta X}{\Delta u} \tag{2.6}$$

The rest of the derivatives follow the same process.

However,a typical static force balance and a regular closed wind tunnel has limitations. Only the derivatives related with the velocity u, v, related with the control, δ_e, δ_T, δ_a and δ_r and related with α and β can be computed. The angular velocities can be changed with some external equipment to create rotation in a given direction.

Chapter 3

Mechanical Design

3.1 Requirements and Start-up Phase

3.1.1 Wind Tunnel Specifications

Técnico possess a closed circuit wind tunnel with an anechoic camber located at the Aerospace Engineering Laboratory in the Mecânica III building. The anechoic chamber isolates the reverberated perturbations, in this way the flow does not suffer any external influence and is uniform along the runtime, with sound wave cut-off frequencies up to 80Hz [16].

An electric motor of 200kw powers a 7-blades fan to a maximum of 1500rpm to produce the air flow. The maximum flow speed is around 50m/s. The control of the flow speed is made by changing the frequency of the inverter, as shown in Figure 3.1. This calibration was made with the instrumentation presented in Chapter 4 to validate the current wind tunnel apparatus for the experimental tests mentioned in Chapter 7.
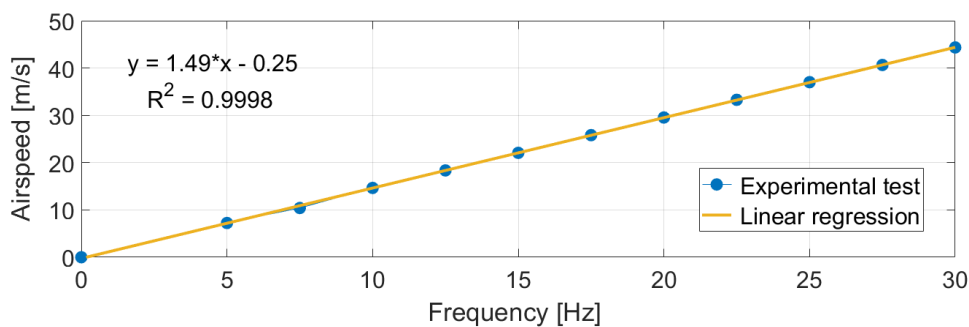
Figure 3.1: Relation between the inverter frequency and the airspeed.

The anechoic chamber is quite large but the test section is defined by the dimension of the nozzle, shown in Figure A.1(a). A schematic representation of the nozzle and the corresponding dimensions are shown in Figure A.1(b). The nozzle diameter of 1.42m sets the maximum dimensions of the models for analyses, and the height of 1.345m from the bottom platform to the center of the nozzle defines the height range of the force balance.

3.1.2 Testing Scenarios

Taking into account the control volume, illustrated in Figure 3.2, the axes used all the subsequent analyses are: the X longitudinal wind axis, parallel to the wind flow but in the opposite direction; the Z perpendicular wind axis pointing towards the ground; the Y axis defined by the right-hand rule to the plane X-Z. The aerodynamics components are six: three forces and three moments. Each force and moment are in respect of an axis. As outlined in Figure 3.2.

Aerodynamic Load	Designation
Stream line force	F_X
Side force	F_Y
Vertical force	F_Z
Stream line moment	M_X
Side moment	M_Y
Vertical moment	M_Z
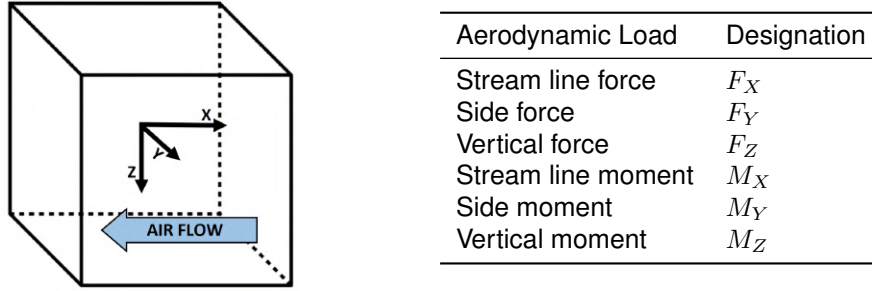
Figure 3.2: Reference axis in the control volume and aerodynamics forces and moments.

To size the aerodynamic force balance, the set of expected loads are required. Two loads sets were considered, one load associated to a half wing model and another to an aircraft model.

Half Wing Model

For the half wing model, the airfoil considered was the cambered *NACA 4412*, that is widely general use in aeronautical applications. The geometrical parameters of the 4-digit *NACA 4412* airfoil are related to its number: maximum camber of 4% located at 40% chord from the leading edge and maximum thickness of 12% chord, as shown in Appendix A, Figure A.2.

The wing dimensions were assumed to entirely cover the test section, so a half wing span (b) of 1m was considered and an aspect ratio ($AR = \frac{b^2}{S}$) of 4 selected.

To handle the most critical case, a maximum flow speed of 50m/s was considered. Assuming standard sea level (SSL) conditions inside the wind tunnel, the considered properties of aircraft and air flow are summarised in Table 3.1.

Table 3.1: Wing and air flow properties

Aspect ratio (AR)	4	Flow velocity (u) [m/s]	50
Span (b_w) [m]	2	Air density (ρ) [kg/m³]	1.225
Chord (c_w) [m]	0.5	Dynamic viscosity (μ) [kg/(m.s)]	1.8E-05
Area (S_w) [m²]	1	Reynolds number (Re)	1.7E+06

The wing is analysed using XFLR5, v6.40 [17] to obtain the forces and moments when subjected to a flow within this conditions. Stall phenomenon occurs at $15°$, as seen in Appendix A, Figure A.3.

An angle of attack (α) of $14°$ was selected to pursue the wing analysis. The software provides the aerodynamics coefficients C_L, C_D and C_m, computed using the usual definitions

$$C_L = \frac{L}{\frac{1}{2}\rho u^2 S}; \qquad C_D = \frac{D}{\frac{1}{2}\rho u^2 S}; \qquad C_m = \frac{M}{\frac{1}{2}\rho u^2 S c} \tag{3.1}$$

The obtained coefficients and corresponding computed forces and moments are shown in Table 3.2.

The simulations were made to a full wing model, however a half wing model is placed on the force balance instead of a full one. Therefore, the numerical values considered the half wing were halved. Furthermore, in the full wing model, the moments of roll and yaw, L and N, are null due to the symmetry of the wing in respect to its root. However, in a half wing model these two moments appear, as consequence of the nonexistence of the balancing loads of the complementary half wing. The arm of the moment is the distance between the attachment point and the center of the lift distribution along the span.

The center of lift distribution was assumed to be at 0.25% of the half wing span. By considering all the these factors, the forces and moments were obtained for the half wing model. As presented in Table 3.3, taking as reference the aircraft reference frame (Figure 2.8).

Table 3.2: Full wing model aerodynamic coefficients and loads.

AR	α [°]	C_L	C_D	C_m
4	14	1.261	0.142	0.121

Table 3.3: Half wing model aerodynamic forces and moments.

α [°]	X [N]	Y [N]	Z [N]	L [N.m]	M [N.m]	N [N.m]
14	- 109	0	-966	241	46	-27

Aircraft Model

The aircraft model considered is a conventional desing, with a wing a *NACA 4412* airfoil, and a tail constituted by a *NACA 0012* vertical stabiliser and a *NACA 4412* horizontal stabiliser. The fuselage length is 1.1m, with the wing placed at 0.3m from the nose. A schematic representation of this aircraft model is shown in Figure 3.3 and the properties of the model and air flow are detailed in Table 3.4.
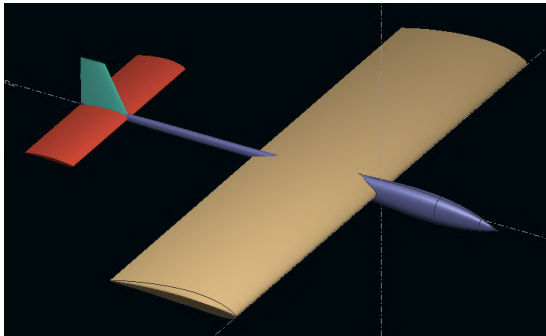
Figure 3.3: Schematic representation of the aircraft model.

	Wing	Horizontal Stabiliser	Vertical Stabiliser
Aspect ratio (AR)	4	4	2.5
Span (b) [m]	1	0.4	0.1
Chord (c) [m]	0.25	0.1	0.1 - root 0.06 - tip
Area (S) [m^2]	0.25	0.04	0.01
Flow velocity (u) [m/s]			50
Air density (ρ) [kg/m^3]			1.225
Dynamic viscosity (μ) [kg/(m.s)]			1.8E-05
Reynolds number (Re)			8.5E+05

Table 3.4: Aircraft model and flow properties.

For the analysis of the aircraft model an angle of attack of $12°$ was selected to ensure the stall does not occur. To create a more complete loading set, the model was also tested with a side-slip angle (β). The aerodynamic results provided by the software are presented in Table 3.5. The forces and moments are computed using Equations (3.1) and presented in Table 3.6.

Table 3.5: Aircraft model aerodynamic coefficients and loads.

α [°]	β [°]	C_D	C_Y	C_L	C_l	C_m	C_n
12	0	0.125	0	1.019	0	0.159	0
12	20	0.196	0.062	0.897	0.006	0.147	0.013

Table 3.6: Aircraft model aerodynamic forces and moments.

α [°]	β [°]	X [N]	Y [N]	Z [N]	L [N.m]	M [N.m]	N [N.m]
12	0	-48	0	-390	0	-15	0
12	20	-75	-24	-343	1	-14	1

3.1.3   Load Set For Both Test Cases

To create structural force balance design simulations, two loads cases sets were considered, one for the half wing and the other for the aircraft model.

In the case of the half wing design, the load set correspond to the forces and moments obtained through the previous half wing analyses. But the forces and the moments require a transformation to the wind tunnel reference axes. This transformation is due to the fact that the wing is actually placed vertically on the force balance. The transformation consists in a rotation of $90°$ over the X-axis.

To the aircraft model force balance was considered a hypothetical situation, with the intuit of obtaining a more critical load case. The selected forces and moments were the maximum values obtained from the test of the aircraft model with and without side-slip angle.

Table 3.7 set the load case to the half wing and aircraft model force balance in the reference axis.

Table 3.7: Load cases for the force balance.

Test Case	F_X [N]	F_Y [N]	F_Z [N]	M_X [N.m]	M_Y [N.m]	M_Z [N.m]
Half-wing model	-109	966	0	241	27	46
Aircraft model	-75	-24	-390	1	-15	1

3.1.4   Design Review

The baseline design of the force balance is the previous work done by João Fernandes [18]. Some modifications will be made to that design to suit new requirements and performance features.

This initial design has a force balance design according to a 6-6 *Stewart* platform based on the 3-3 platform. The design of the force balance was made taking into account the dimensions of the test section of the wind tunnel detailed in Section 3.1.1. The force balance is based on a metal surface named "table". The platform above is named "fixed platform" because it is fixed during the experimental run. However, it is possible to adjust the side-slip angle with this component by using a rotating collar set between the two surfaces. Two other components complete the balance: the bars and the top platform, denominated as sensing bars and moving platform respectively.

The union between each sensing bar and the two platforms is made through a joint system with two components: the rod end bearing and the coupler. The coupler is fixed to surfaces and a pin unite this structure with the rod end bearing. This rod end bearing satisfied the typical spherical joint used in *Stewart* platforms. To ensure the rod end bearings are screwed on the top of the sensing bar with the same rotation direction, a rod end bearings with a left male thread and a right male thread were selected.

The top part of the force balance makes the union between the model and the *Stewart* platform. This part is constituted by a flange, a strut and an alpha adjustment system. The flange fixes the strut to the fixed platform, being possible to adjust the height of the strut. The alpha adjustment system has two components and allows for the angle of attack adjustment.

3.1.5 Mechanical Load Limits and Acceptable Displacements

The design of the force balance depends on two design specifications: the limit loads and the acceptable displacements. The limit loads are the critical for the mechanical sizing and material selection. The acceptable displacements are those that still maintain the apparatus in its set desired position.

The critical mechanical parts of the force balance are the sensing bars, whose extension will be measured and the strain (ϵ) computed. To make the deformation controllable, the bars must work under the elastic deformation regime, so the admissible stress must be in the linear elastic part of *stress-strain* diagram, between zero and (*pl*), see Figure 3.4.
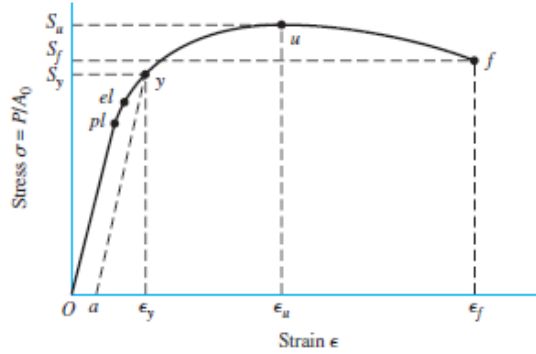
Figure 3.4: Stress-strain diagram obtained from the standard tensile test. pl marks the proportional limit; el, the elastic limit; y, the offset-yield strength as defined by offset strain a; u, the maximum or ultimate strength; and f, the fracture strength [19].

Under this regime, the stress is defined by the *Hooke's law* $\sigma = E\epsilon$ where *E* is the slope of the linear part, called *Young's Modulus* or *modulus of elasticity* and σ is the stress [19].

The limit stress of the elastic deformation is called *Yield Stress*. The maximum acceptable force applied on the sensing bars are then given by

$$Force = \sigma A \tag{3.2}$$

where A is the cross-section area.

The *Yield Stress* is the stress limit to the tension but not to compression. In the latter case, the bar can suffer the *buckling* phenomenon. *Buckling* occurs when a column starts to bend due to compressive forces. The force for which the buckling occurs is the critical force (P_{Cr}), computed by the *Euler's critical load* formula,

$$P_{Cr} = \frac{C_{fix}\pi^2 E I}{l^2} \tag{3.3}$$

where the C_{fix} is a constant that depends on the conditions of the fixation of the column, I is the minimum area moment of inertia and the l is the length of the column. In the case of the column being fixed with rotation free in both end, the C_{fix} corresponds to 1 [19].

To increase the elasticity of the sensing bars, hollow tubes are used. The area moment of inertia of a tube is given by

$$I = \frac{\pi(D_t^4 - d_t^4)}{64} \tag{3.4}$$

where D_t is the outer diameter and d_t is the inner diameter.

The *Yield Stress* and the critical force are used to set the loading limit of the force balance. However,

if the acceptable displacements are not ensured, stricter limit loading need to be imposed.

The displacements are a consequence of the forces and moments applied on the force balance. These displacements are in the form of rotations and translations of components. Thus, the components must have a small deviation from the initial positioning, like the case of the alpha adjustment system. A large displacement of this component would introduce a variation of the initial setting parameters that are desired to keep constant: this parameters are the angle of attack and the side-slip angle.

Therefore, the displacements are measured at the top of the alpha adjustment system in terms of the angles variation over the Y-axis and the Z-axis. The angles are computed by considering two specific points and their displacement in a given direction. Figure 3.5 shows the points and the displacements considered in the measurement of the two incremental angles, θ_Y and θ_Z. θ_Y represents a change of the angle of attack in the aircraft model force balance, and the side-slip angle in the half wing force balance. The opposite also occurs for the case of θ_Z, that corresponds to change in β in the aircraft model force balance and to α in the half wing force balance.

(a) Variation of θ_Y on the top of force balance. (Side view)

(b) Variation of θ_Z on the top of force balance. (Top view)
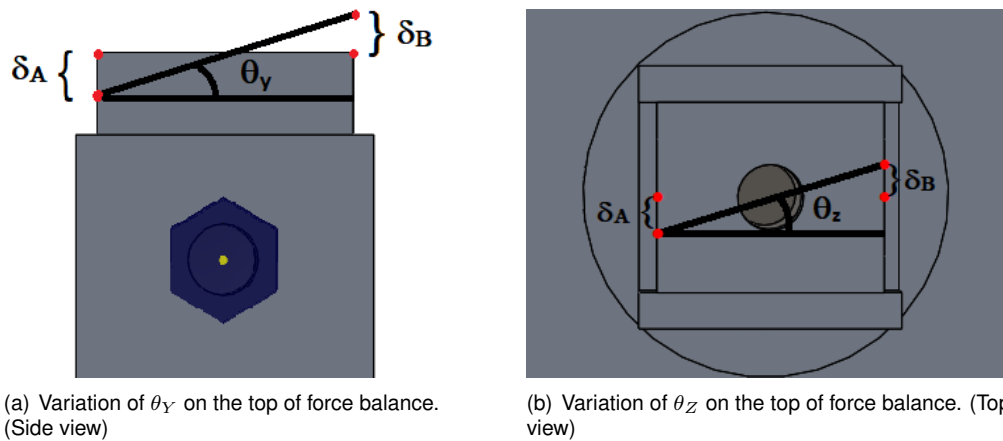
Figure 3.5: Schematic representation of the incremental angles measured on the alpha adjustment.

Taking into account Figure 3.5, the following geometrical relation is derived:

$$\theta = \arcsin \frac{|\delta_A - \delta_B|}{l} \tag{3.5}$$

where l is the length of the alpha adjustment system measured on top part.

The forces and moments applied should be limited by the displacements. The limit applied is that both of incremental angles cannot be greater than $0.5°$.

3.2 Computational Structural Analysis

In this section, the design of all parts and all computational analyses of the force balance will be carried out. The used software is *SolidWorks®* v2018 by Dassault Systèmes.

3.2.1 New Considerations and Additional Parameters

The previous computer-aided design (CAD) [18] was made in a different version of the software. Therefore, the first task was to reassemble each part of the force balance in accordance with the new

version features. After updating the CAD, it was found that the simulations done previously were unable to be reproduced. Hence, it was necessary to generate all the simulations from scratch again. This occurrence gave an opportunity to redefine and add new parameters to the simulations.

The load sets selected in Section 3.1.3 were added to the simulation. Due to some lack of pure moments by the software when multiple loads are applied, the moments are represented by two opposing forces equal in modulus and defined in order to obtain the respective moment. The acceleration of gravity was excluded from the simulations, since a model which only regards deformations due to the applied aerodynamic forces and moments is desired. The weight of the structure is only considered in experimental procedures, such as calibrations and setups.

One modification of the structure was made from the very beginning, which concerns the material used for the sensing bars and the flange. This modification was necessary considering the available material from the supplier. The new selected materials belong to the same alloy series, as in the initial conceived design, but differ in the percentage of composition in respect of its elements or the suffered heat treatment. This can be seen in the change of the two last numbers of the aluminium reference, which correspond to composition, or the indexed term, which corresponds to heat treatment. The material selected for the sensing bars is the Al 6063-T6 instead of Al 6061-T6 and for the flange is the Al 7075-T6 instead of Al 7075-0.

To make the simulations run faster and save computational effort, the simulation has been simplified by excluding some unnecessary structural parts. The excluded parts are the table and the rotating collar because they have a great stiffness and are the last parts of load carrying. As such, only the parts above the rotating collar, the most susceptible to loads, will be analysed.

In Figure 3.6, the simplified force balance structure is shown for both cases (aircraft and half wing model) with the loads applied.
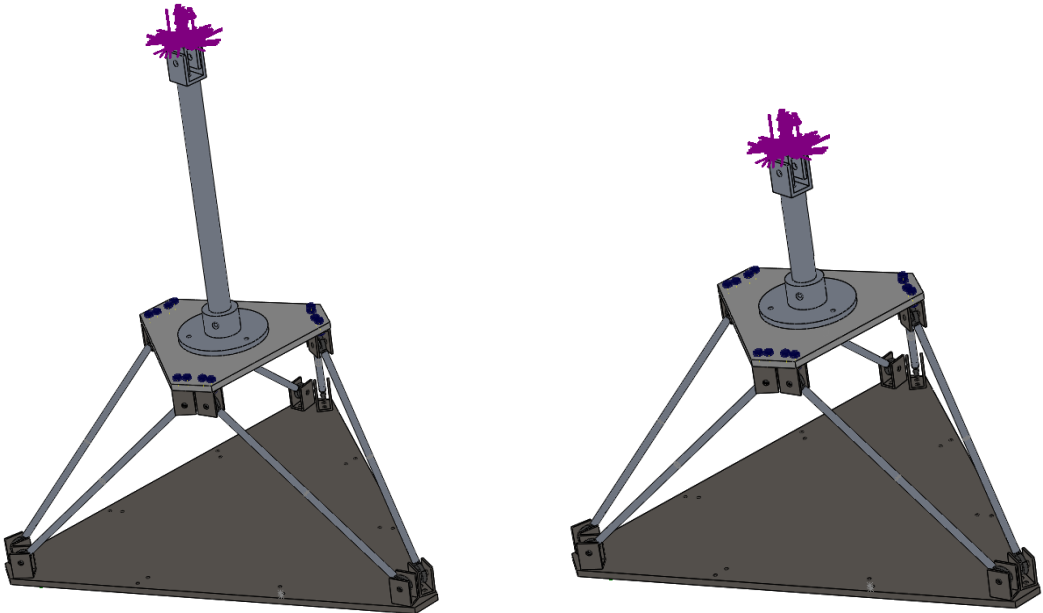
(a) Model of the force balance for the aircraft model.

(b) Model of the force balance for the half wing model.

Figure 3.6: Simplified model of the force balance with loads and gravity set for each case study.

Most of the force balance parts interact with each other in a *bonded* way: they are welded or screwed. However, the rod end bearing, see Figure A.4, has another contact set. This part is *bonded* to the sensing bar through a screw and a tightening pin, having an internal spherical component that allows free rotation. A *no penetration* contact set is applied to that sphere. With these bonds of rod end bearing, sensing bar and pin, the sensing bar only suffers axial forces, tension and compression.

To finalise the simulation setup, a static study and a direct sparse solver were selected. According to *SolidWorks*®, these are the best settings for this problem type, contact sets and mesh, and also the most advisable for the computational hardware available.

3.2.2 Mesh Parameters and Convergence Study

The structural analyses are made with a finite elements method (FEM), and therefore the behaviour of the model is predicted with the combination of information obtained from each element that makes up the model. The mesh used is based in parabolic tetrahedral solid elements, also called second-order, or high-order elements. These elements are defined by four corner nodes, six mid-side nodes, and six edges, as seen in Figure 3.7. With the parabolic elements, curvature-based mesh is used, that creates more elements in higher-curvature areas automatically, producing better results than linear tetrahedral elements or standard Voronoi-Delaunay mesh [20].
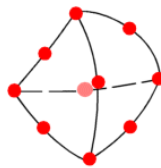
Figure 3.7: Parabolic tetrahedral solid elements for FEM simulations [20].

Regarding the mesh parameters, some components required more elements than others due to their influence on the complete model. An example of a component which does not need these sensitive analyses is the fixed platform. Conversely, the rod end bearing does need them. For this reason, *mesh controls* are applied. The *mesh control* is a tool of *SolidWorks*® which allows one to set a mesh element dimension for a selected surface or surfaces. This setting stays unchanged along the mesh resizing. A maximum mesh element size of 30mm was set to the surface of the fixed platform and a maximum mesh element size of 3mm was applied to the spherical bearing surface of the rod end bearing.

All these parameters complete the simulation setting, their selected was made to suit the analyses in question and save computational effort. However, a mesh convergence analysis is required to guarantee the accuracy of the results. The parameter chosen as variable for the mesh convergence study was the total strain energy, that corresponds to the energy stored by a system undergoing deformation.

Mesh convergence studies were made for both the aircraft model force balance and for the half wing model force balance. A more detailed analysis was made for the case of the aircraft model force balance and from that a suitable start condition was selected for the half wing force balance mesh convergence study. The parameter of refinement which was changed with each iteration was the mesh element dimension, which in turn defines the number of mesh elements. Besides the total strain energy,

other quantities given by the simulation were taking into account. The maximum stress was taken as redundancy, the mesh degrees of freedom (DOF) and the simulation time as additional information. The convergence analyses made to both force balance model are depicted in Figure 3.8, where the total strain energy and the computation time as function of the number of mesh elements are presented.

(a) Convergence study for the case of the aircraft model force balance.

(b) Convergence study for the case of the hall wing model force balance.
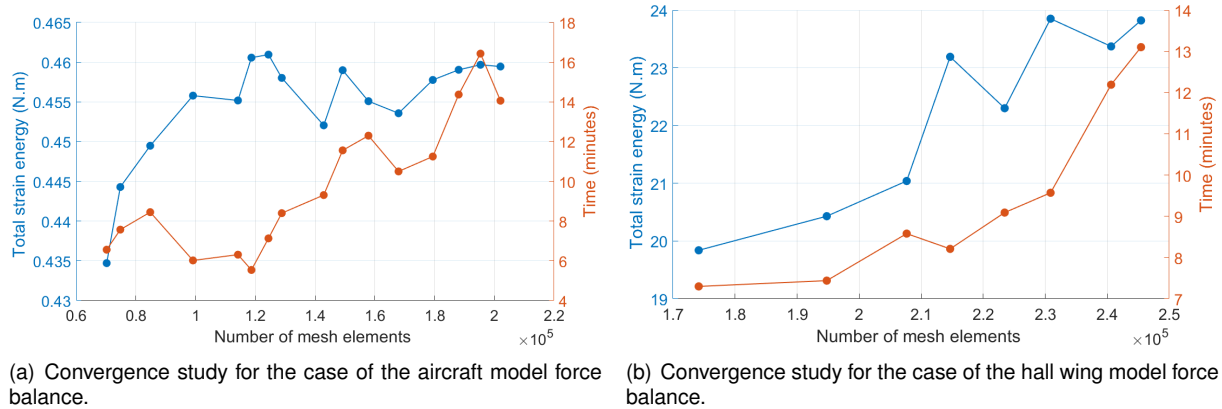
Figure 3.8: Variation of the total strain energy with the number of mesh elements.

As seen the selected sample of mesh elements tend to converge the total strain energy to a certain value. The last iterations have a small deviation around that value. The time of simulation sometimes decreased with the degree of refinement, due to the mesh adaptations done by the software for each element on the boundaries. In this way the refinement of the mesh has a dependency on the software and, therefore, the individual refinement on the selected surfaces, as done previously, is crucial to reduce the computational effort. Simulations of 15 minutes using so many number of mesh elements, is a direct consequence of that. Consequently, the maximum number of elements used on the convergence analyses, 202046 for the aircraft case and 245445 for the half wing case, are used reliably to establish the subsequent results.

3.2.3 Simulation Results

The simulation analyses focus firstly on the sensing bars. *SolidWorks*® provides the *Von Misses* stress as default, but for this analysis in particular, another stress configuration is considered, corresponding to one with a specific direction. The considered direction is the axis of symmetry of each bar, so, the stress corresponds to pure axial stress. Figure 3.9 (a) shows the stress plot for one sensing bar which is given with respect to the direction of its axis of symmetry. *SZ* is the stress in the *Z* direction of the cylinder with the reference system of *Axis 18*.

The strain was set with the same configuration as the stress. The strain response shows some variations along the elements of the sensing bar, a normal occurrence in finite elements analyses (FEA) of the strain. To produce more accurate results, a *SolidWorks*® tool was used: a *sensor* which is defined for each bar. A *sensor* is a group of selected mesh elements, where it is possible to take quantities in each element and to average them. Figure 3.9 (b) shows a strain plot for one sensing bar given with respect to its axis of symmetry, in which the sensor of that bar is also shown. The *sensor* is placed in the middle of the bar and has 40mm in length.

| (a) Stress plot. | (b) Strain plot with the corresponding sensing bar *sensor*. |
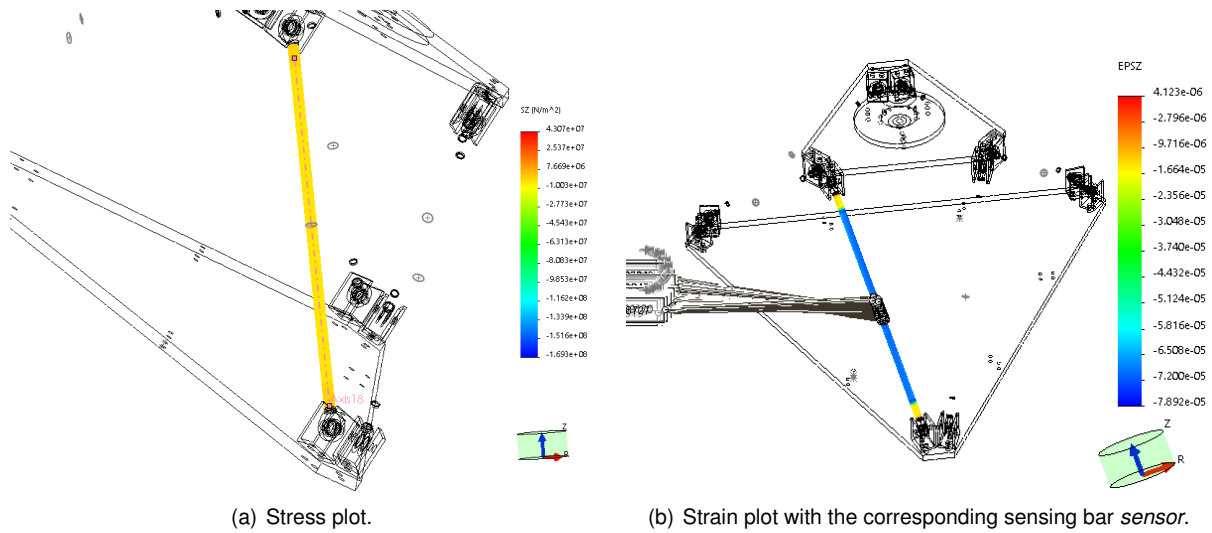
Figure 3.9: Plots for sensing bar set with respect to its symmetrical axis.

Figure 3.10 shows the enumeration of the sensing bars adopted and the axes of reference. In addition to the stress and the strain, the force was computed for each sensing bar through Equation (3.2). The used area is the area of a tube with 7mm of inner diameter and 10mm of outer diameter. The simulation results obtained for the aircraft model force balance and the half wing force balance are presented in Table 3.8.
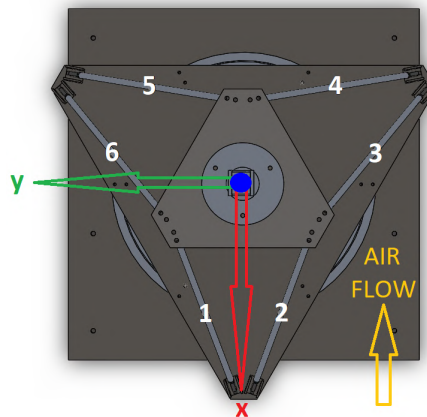
Figure 3.10: Enumeration of the sensing bars in the subsequent analyses.

Table 3.8: Stress, force and strain of each sensing bar.

Sensing Bar		1	2	3	4	5	6
Aircraft Model	Stress (N/m^2)	4.66E+06	2.96E+06	2.12E+06	3.39E+05	6.00E+05	3.83E+06
	Force (N)	186.84	118.45	84.90	13.56	24.04	153.40
	Strain	6.76E-05	4.29E-05	3.07E-05	4.91E-06	8.69E-06	5.55E-05
Half Wing Model	Stress (N/m^2)	-2.99E+07	3.51E+07	4.16E+07	-3.64E+06	-5.72E+06	-3.75E+07
	Force (N)	-1195.65	1405.14	1664.30	-145.6	-229.08	-1501.27
	Strain	-4.33E-04	5.09E-04	6.02E-04	-5.27E-05	-8.29E-05	-5.43E-04

The *Yield Stress* (241E+06 N/m^2) and the critical buckling force (2260 N) are respected for each sensing bar, but these parameters were not important at the moment due to the values which were observed for the strain. Some of the strain values are close to one micrometre (1E $- 06$) being this the

lower advisable measurement limit of the available strain sensor. A higher strain value is desirable for a better use of the reading scale and to respect the recommended values.

Although this design needs some modifications, the displacements θ_Y and θ_Z were computed with Equation (3.5) and presented in Table 3.9. The design requirement $\theta < 0.5°$ are met for both models.

Table 3.9: Rotations θ_Y and θ_Z in both models.

Displacement	θ_Y (°)	θ_Z (°)
Aircraft Model	0.00	0.01
Half Wing Model	0.21	0.34

3.3 New Parts Design

The performance of the force balance was found to require some improvement, so some of its parts will be redesigned, giving particular attention to their mechanical limits and the acceptable displacements. The redesign of the sensing bars has as principal objective an improvement of the strain measurement, which can be done by manipulating its cross-section area. The strain measurement is highly dependent on the characteristics of the selected strain sensor. For this, experimental tests that evaluates the sensitivity of the strain sensor are required for the sensing bars sizing. Moreover, the flange and the moving platform are modified, mainly, to compensate the incremental displacements of the new assembly.

3.3.1 Sensing Bar Sizing

The sensing bar sizing is made by taking into account three criteria: the *Yield Stress*, the buckling critical force and a measurement sensitivity of 1N.

The maximum admissible force is computed through Equation (3.2), by taking account the *Yield Stress* of the Al *6063-T6* ($241\text{E} + 06\text{N/m}^2$) and the respective cross-section area. To ensure that the sensing bar works within the elastic regime, it was postulated that the axial force should not surpass 60% of the *Yield Force*.

The *buckling* critical force is computed through Equation (3.3), considering a *Young's modulus* of $68, 9\text{E} + 09\text{N/m}^2$ and a length of 335mm. To ensure that buckling of the sensing bars does not occur during the experiments, it was postulated that the applied axial force should not surpass 80% of the critical force.

To verify if the sensing bar was able to measure increments of 1N, an experimental test was carried out. Such test consisted in subjecting the bar to several set of loads, each one heavier than the previous by 1N, and recording the respective measurement values.

The required instrument to measure the strain is the portable strain indicator *P-3500* by *Vishay*, see Figure 3.11 (a). This instrument can be set to the three types of bridges for which a wide range of functionalities is available. All the configuration instructions are presented on the cover of *P-3500*.

(a) Portable strain indicator by *Vishay*, *P-3500*. Courtesy of *Artisan*.

(b) Used weights and support .

Figure 3.11: Apparatus for the experimental tests on the sensing bar.

The used strain gauge, its placement and the *Wheatstone* bridge types are described in Chapter 4. The strain indicator has a reading scale in micrometre of strain. Because the experimental test has the unique objective of measuring the sensitivity of the sensing bar, a quarter bridge was selected and the instructions to connect the single strain gauge to the strain indicator were followed. The three initialisation steps to set up the strain indicator are: set the *AMP ZERO* to read zero; set the gauge factor controls in accordance with the strain gauge in use; put the initial strain measurement at zero. The load experiment starts with the weight of the weight support structure, ≈ 1N, and ends with a combined weight of ≈ 39N. It is incremented ≈ 1N until the ≈ 21N, and ≈ 2N after. All the weights were calibrated in a high precision scale. The used weights in the sensing bar sizing experimental tests are shown in Figure 3.11 (b).

First Sensing Bar Sizing

The first sizing attempt was made with a large cross reduction, by reducing the previous thickness from 1.5mm to 0.45mm. It was used a tube of aluminium alloy with 7mm of outer diameter and 6.1mm of inner diameter, available from a supplier. The first two criteria of analyses and some dimensions of the first sensing bar sizing attempt are presented in the first line of Table 3.10. These criteria values are suitable to the expected stress and force for the aircraft model force balance but not for the half wing model, see Table 3.8. However, the experimental test was proceeded to collect data from the match between this testing bar and the sensor.

Table 3.10: Dimensions of the testing bars and two analysis criteria values.

Size Case	D_y (m)	d_t (m)	Area (m^2)	I (m^4)	*Yield Force* (N)	P_{cr} (N)
First Bar	0.007	0.0061	9.26E-06	4.99E-11	2231	302
New Bar	0.009	0.007	2,51E-05	2,04E-10	6057	1237
	0.01	0.007	4,01E-05	3,73E-10	-	2260

The placement of the strain sensor did not pose any issue, but the coupling between the testing bar and the rod end bearing did. The bar thickness of 0.45mm is not appropriate to create a *M8* female thread

with the correct dimensions to couple the rod end bearing [21]. Causing several plastic deformation on the tube wall and misalignment between the two parts. Figure 3.12 (a) shows the coupling between the two parts with the plastic deformation.

The strain response obtained with the *P-3500* for the defined load set is shown in Figure 3.14. The evolution of the strain was almost linear and each 1N increment and 2N was detected.

Despite this sensing bar design only suits the aircraft model force balance, a premature assembly of six of these bars and the fixed and moving platforms were made. But many of the bars suffered damage, such as bending and rupture, see Figure 3.12 (b). As such, the thickness of 0.5mm was found to be inappropriate to the necessary handling of the force balance. The rod end bearing male thread proved to be a critical factor and should be considered in the following sensing bar sizing.

(a) Coupling with plastic deformation on the thread.

(b) Damage occurred during the assembly.
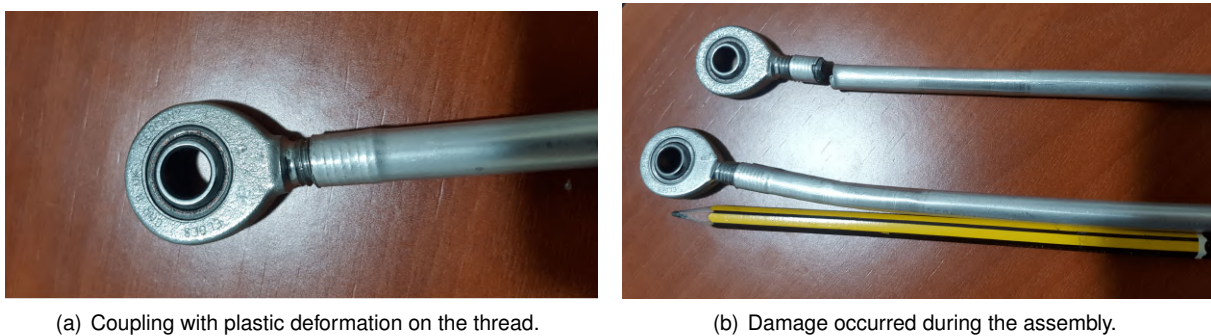
Figure 3.12: First testing bars with the rod end bearing.

New Sensing Bar

The new sensing bar design selected is a combination of two cross-sections diameters with requiring more manufacture but fit the requirements. This bar has the initial selected outer and inner diameter, 10mm and 7mm, but there is a middle section of this new sensing bar in which the wall thickness has been reduced to 1mm. This new sensing bar was an outer diameter of 9mm and an inner diameter of 7mm. The bar dimensions and the first two criteria of analysis are presented in bottom lines of Table 3.10, for both bar cross-sections considered.

The *Yield Force* obtained with the small cross-section satisfies the computed forces from the simulations analyses for the two force balance models. Equation (3.3) do not take into account bars with variable cross-section, but the real P_{cr} should be placed between the two computed values. The previous computed forces are less then the maximum *buckling* force for this new sensing bar.

The length of the middle section should be able to attach the strain sensor and disperse the concentration of stress in the reduction wedge. To determine the minimum length so that the stress is uniform, a computational tensile test of the new sensing bar is performed with a 1500N force. Figure 3.13 (a) shows that the stress is uniform after ≈ 10mm of the reduction wedge. The length selected for the middle part of the new sensing bar is 100mm. A testing new sensing bar was manufactured and instrumented, see Figure 3.13 (b).

The strain response to the load set, see Figure 3.14, shows this new sensing bar design is still capable of measuring increments of 1N with the selected strain sensor.
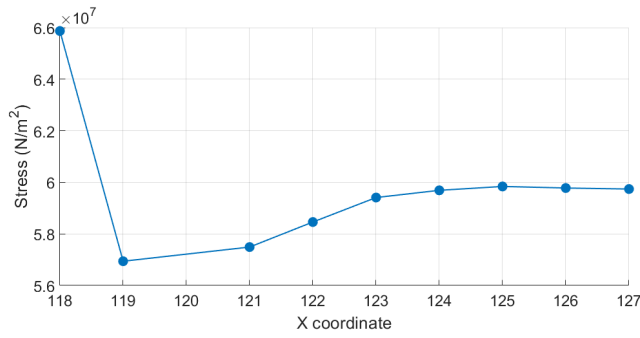
(a) Numerical simulation. Stress over X coordinate.

(b) New sensing bar made only for experimental tests.

Figure 3.13: Stress analyses in the reduction of the cross-section of the new sensing bar.
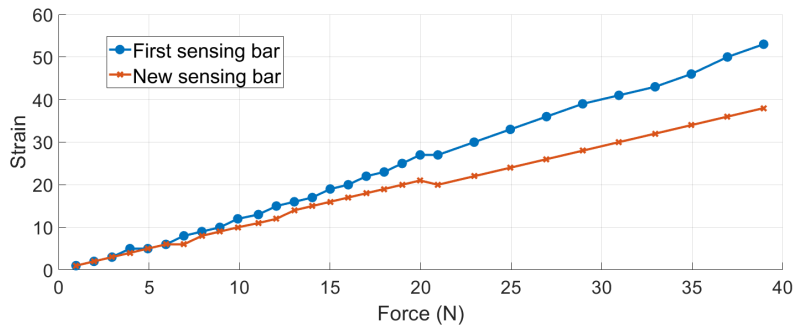
Figure 3.14: Strain response for experimental load set.

3.3.2 Moving Platform, Flange and Strut

The first part to be modified was the moving platform since, from the stress simulations, it experienced the maximum stress and deformations. The initial selected material for this part was a composite structure with carbon fibre, epoxy and foam. This material was changed to a more rigid material, the Al 6082-T6. The thickness of this part component was increased from 5mm to 10mm.

A new flange design was adopted, see Figure 3.15, to decrease the bending of the strut and making its manufacture easier. This new design increased the weight of the flange by 70%. However, since the component was already initially very light, this percentage corresponds to merely 6.6N.
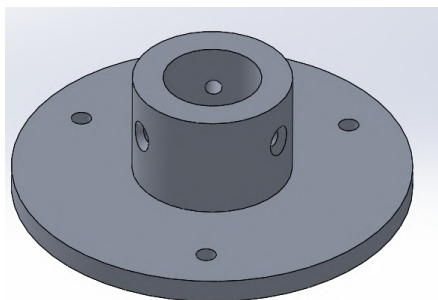
(a) Previous flange design.
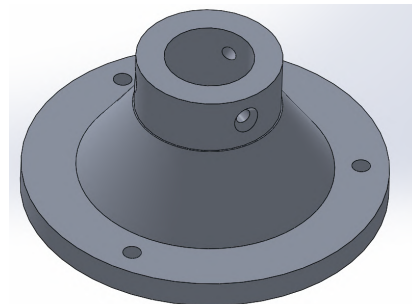
(b) New implemented flange design .

Figure 3.15: CAD models for flange.

From the stress analyses, one can also conclude that the strut does not suffer considerable stress. The wall thickness of the strut was reduced, by changing the inner diameter from 20mm to 25mm. This last modification introduces a decrease in weight, this way, the increase in weight due to the other two

28

modifications is partially compensated.

3.4 Complete New Balance Assembly

The assembly of the new force balance is represented in Figure 3.16, in which all its components are identified and the respective quantities and material are detailed. The technical drawing of each part component of the force balance and its dimensions are shown in Appendix B.

Item number	Part name	Quantity	Material
1	FixedPlatform	1	Steel 1.0037
2	Coupler	12	Alloy Steel
3	RodEndBearing_R	6	Steel 1.0503 Brass
4	NewMovingPlatform	1	Al 6082-T6
5	RodEndBearin_L	6	Steel 1.0503 Brass
6	NewSensingBar	6	Al 6063-T6
7	RotatingCollar	1	Al 2024-T4 Al 6063-T6
8	Table	1	Steel 1.0037
9	NewFlange	1	Al 7075-T6
10	NewStrut	1	Al 6063-T6
11	alphaAdjustment_1	1	Al2024-T4
12	alphaAdjustment_2	1	Al 2024-T4

Figure 3.16: Exploded view of the new force balance model assembled.

3.4.1 Structural Numerical Simulation

To ensure that the previous mesh parameters are still valid, a small convergence analysis was made, taking as reference some of the numbers of mesh elements from the previous convergence. The new convergence analysis to the aircraft model force balance is shown in Appendix A, Figure A.5. As expected, the number of mesh elements that was necessary to achieve convergence suffered a slight increment, but only to the aircraft model. The subsequent results are obtain using 215125 elements for the aircraft model, more 6% in relation to the previous convergence. The increment in half wing model to achieve convergence is less than 1% and therefore neglected.

Using the same methodology, stress, force and strain are obtained, being presented in Table 3.11 for both models. Table 3.12 shows the displacements θ_Y and θ_Z.

The new assembly introduces significant improvements in respect of the strain, and the necessity of a better use of the reading scale is satisfied without compromise the critical displacements. The increments of θ_Y and θ_Z are almost neglected. The new values of stress for the new sensing bars

Table 3.11: Stress, force and strain of each sensing bar from the new force balance.

Sensing Bar		1	2	3	4	5	6
Aircraft Model	Stress (N/m^2)	7.44E+06	4.71E+06	3.37E+06	5.39E+05	9.57E+05	6.10E+06
	Force (N)	187.01	118.43	84.77	13.54	24.04	153.28
	Strain	1.08E-04	6.83E-05	4.89E-05	7.81E-06	1.39E-05	8.84E-05
Half Wing Model	Stress (N/m^2)	-4.75E+07	5.59E+07	6.63E+07	-5.80E+06	-9.11E+06	-5.98E+07
	Force (N)	-1194.56	1405.42	1666.80	-145.82	-229.03	-1502.44
	Strain	-6.89E-04	8.10E-04	9.61E-04	-8.41E-05	-1.32E-04	-8.66E-04

Table 3.12: Rotations θ_Y and θ_Z of the new models.

Displacement	θ_Y (°)	θ_Z (°)
Full aircraft model	0.00	0.02
Half wing model	0.22	0.36

respect the *Yield Stress* and the *Buckling* criteria. The maximum computed force, 1666.8N, is 28% of the *Yield Force* and the maximum compressive force, -1502.44N, is 67% of the maximum P_{cr} for the new sensing bars, and 26% in the range of the two critical forces.

The mechanical setup is concluded with a stress analysis of the complete force balance model, and the forward confirmation that the *Yield Stress* is respected in all of its components as demonstrated in Figure 3.17.

(a) Aircraft model force balance.   (b) Half wing model force balance.
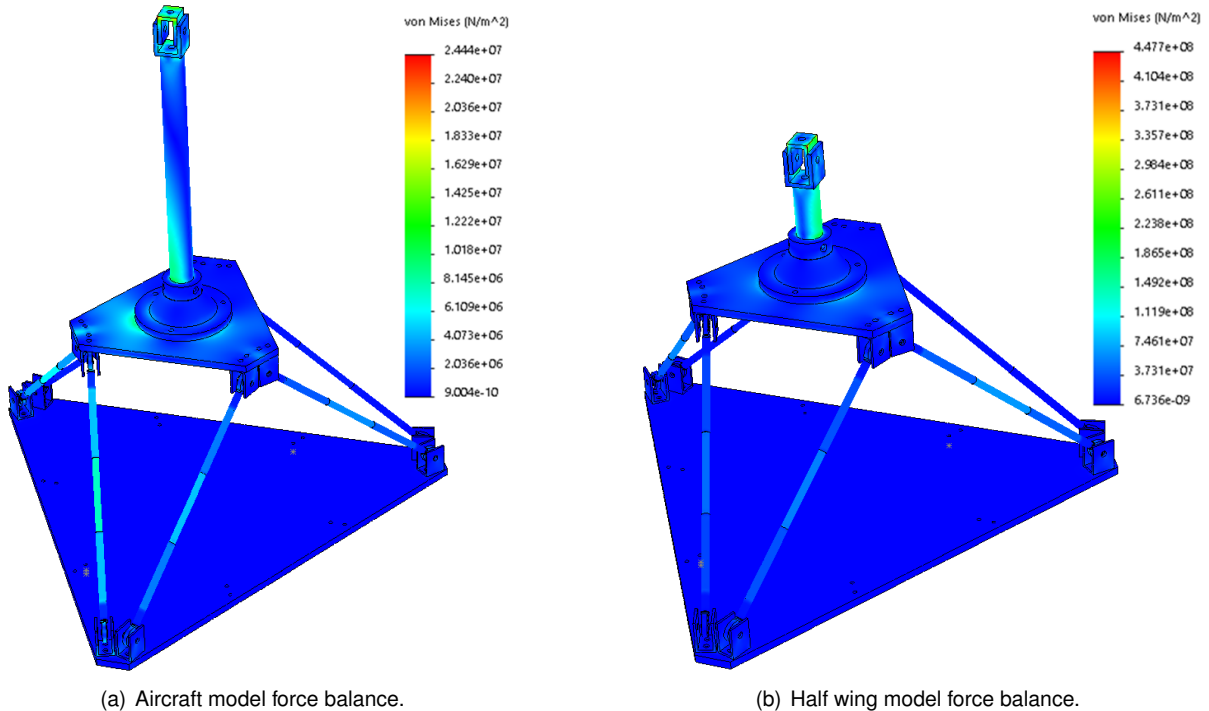
Figure 3.17: Stress plot of the force balance models.

The maximum stress is $2.44\text{E}+07$N/m^2 for the aircraft model and $2.48\text{E}+08$N/m^2 for half wing model. In both cases, the stress occur in the alpha adjustment with an *Yield Stress* of $3.25\text{E}+08$N/m^2. Consider the worst case scenario, only 76% of the elastic regime is achieve.

3.4.2 Analytical Model and Application

With the set configuration of the force balance, an analytical model can be defined to compute the forces and moments produced by the study case concerning the sensing bars forces. This analytical model is a rigid body model, so some disparity from the simulation and the real physical occurrence is expected. However, this model helps to understand the translation of the behaviour of the force balance over an analytical perspective and compare with the FEM used in the computational simulations.

Figure 3.18 (a) shows the projections of the sensing bar 1 on the three axes their corresponding length.

(a) Projections in the three axes of the new sensing bar # 1 and its dimensions.

(b) Projections in X axis and Y axis of the six new sensing bars and its dimensions.
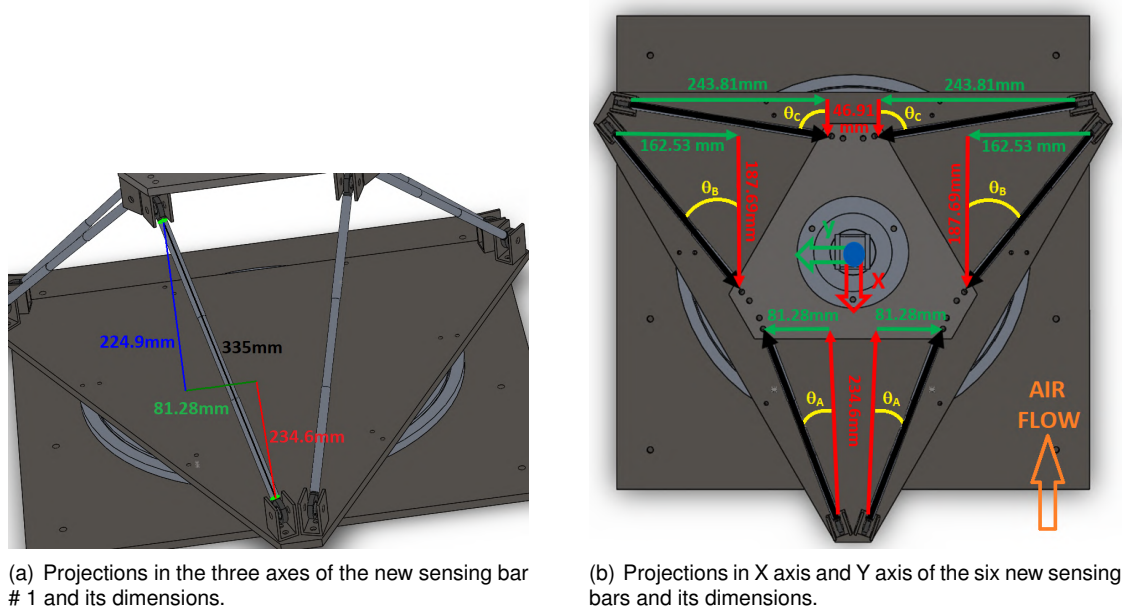
Figure 3.18: Projections required to create the analytical model.

From the lengths of the projections of the sensing bars, two angles can be computed, between each sensing bar symmetry axis and the Z projection, and between the X and Y projection. The Z projection lenght is common to all sensing bars, corresponding to θ_V angle, but the X and y projection are not. Figure 3.18 (b) is a representation of the aerodynamic force balance on the X-Y plane, with all the Y and Y projections represented and their lengths depicted for the six sensing bars. It was set an axial tension force to the six sensing bars to be coherent in the definition of the projections directions. From these values, it was computed θ_A is $19.11°$, θ_B is $40.89°$, θ_C is $79.11°$ and θ_V is $42.17°$.

The forces in each bar, F_1, F_2, F_3, F_4, F_5, F_6, can be decomposed in the X and Y directions using the projections of each bar, or the correspondent angles following the enumeration in Figure 3.10. With all these quantities, a balance of forces is made, relating the sensing bar forces with the forces applied on the model,

$$\begin{cases} F_X = \Big[(-F_1 - F_2)\cos(\theta_A) + (F_3 + F_6)\cos(\theta_B) + (F_4 + F_5)\cos(\theta_C)\Big]\cos(\theta_V) \\ F_Y = \Big[(F_1 - F_2)\sin(\theta_A) + (F_3 - F_6)\sin(\theta_B) + (F_4 - F_5)\sin(\theta_C)\Big]\cos(\theta_V) \\ F_Z = -(F_1 + F_2 + F_3 + F_4 + F_5 + F_6)\sin(\theta_V) \end{cases} \tag{3.6}$$

To deduce the equation that transforms the forces of the sensing bars into moments applied to the

top of the strut, the distance between the interception of the bar force and the moving platform with the centre of the moving platform. It is necessary to decompose the distance in X and Y coordinates. Figure A.6 shows the distance in X and Y coordinates of the interceptions of the six sensing bars with the moving platform. From these values dX_A is 45.5mm, dX_B is 81.3mm, dX_C is 126.8mm, dY_A is 120.1mm, dY_B is 99.4mm and dY_C is 20.7mm.

The transformation equation is deduced by applying a balance of moments, in the form $\vec{M_0} = \sum_{n=1}^{6} \vec{r_n} \times \vec{F_n}$, to a point at the centre of the moving platform with D_S on the z coordinate, corresponding to the adjustable strut height. The $D_s = 0$ is placed on the moving platform top plane. The resulting transformation equation is then

$$
\begin{cases}
M_X = \sin(\theta_V)\Big[dY_A(-F_1 + F_2) + dY_B(F_3 - F_6) + dY_C(-F_4 + F_5)\Big] \\
\quad -D_S \cos(\theta_V)\Big[(F_1 - F_2)\sin(\theta_A) + (F_3 - F_6)\sin(\theta_B) + (F_4 - F_5)\sin(\theta_C)\Big] \\
M_Y = \sin(\theta_V)\Big[dX_A(F_1 + F_2) + dX_B(F_3 + F_6) - dX_C(F_4 + F_5)\Big] \\
\quad +D_S \cos(\theta_V)\Big[(-F_1 - F_2)\cos(\theta_A) + (F_3 + F_6)\cos(\theta_B) + (F_4 + F_5)\cos(\theta_C)\Big] \\
M_Z = \cos(\theta_V)\Big[(F_1 - F_2)(dX_A\sin(\theta_A) + dY_A\cos(\theta_A)) \\
\quad +(F_3 - F_6)(dX_B\sin(\theta_B) + dY_B\cos(\theta_B)) \\
\quad +(-F_4 + F_5)(dX_C\sin(\theta_C) + dY_C\cos(\theta_C))\Big]
\end{cases}
\tag{3.7}
$$

Application of the Analytical Model

The values of bar forces obtained from the computational simulation, Table 3.11, were used to compute the prediction forces and moments with the analytical model. The last missing element is the D_S, this value is 0.455 m to the aircraft model and 0.185 m to the half wing model. This distance comes up from the technical drawings, considering the strut and the alpha adjustment system.

The load forecast from the analytical model and the comparison with the applied load is depicted in Table 3.13.

Table 3.13: Load prediction through the analytical model with bar forces.

		F_X [N]	F_Y [N]	F_Z [N]	M_X [N.m]	M_Y [N.m]	M_Z [N.m]
Aircraft Model	Applied load	-75	-24	-390	1	-15	1
	Analytical model	-75.26	-24.25	-390.1	1.07	-15.12	1.01
	Difference (%)	0.4	1.0	0.0	7.0	0.8	1.0
Half Wing Model	Applied load	-109	966	0	241	27	46
	Analytical model	-108.07	967.32	-0.24	241.14	27.32	46.25
	Difference (%)	0.9	0.1	-	0.1	1.2	0.5

As expected, a deviation of values occur comparing the analytical model with the simulation results. Therefore, the analytical model is used as a base to validate the simulation result when a small disparity occurs, and the computational simulation with FEM introduces more accuracy in the values.

The difference between the analytical model results and the simulation results anticipate the possible divergence between these results and the experimental results. Consequently, a calibration procedure of the manufactured force balance at hand is essential to create the most accurate results.

Chapter 4

Instrumentation

This chapter introduces the necessary instruments to collect the required data, giving details of the hardware and their integration in the force balance.

4.1 Background and Purchased Instruments

4.1.1 Strain Sensors

The basic technique to compute forces in wind tunnel experiments is measuring the strain of a default part. This method foresee the aerodynamic forces are the only load acting on the wind tunnel model, therefore the deformation of the structure can be related with them.

A strain gauge is an electromechanical device where the electrical resistance can be related with the strain in the component directly, the wire strain gauge was one of the first to be used. The physical principle of a wire strain gauge is that a change in electrical resistance is produced when a strain variation is applied to the gauge [7]. The electrical resistance of a wire can be written as

$$R_g = \frac{\rho_w l}{A} \tag{4.1}$$

where R_g is the resistance of wire, l the length of the gauge grid, A the cross section area of the wire and ρ_w is the resistivity. The Equation (4.1) can be differentiate with respects to resistance, applying further elastic deformation theory, comes up the equation which relate the resistance and strain,

$$\frac{dR_g}{R_g} = k\epsilon \tag{4.2}$$

where k stands for calibrated strain gauge sensibility, called the gauge factor, and $\frac{dR_g}{R_g}$ for the relative change on the strain gauge resistance.

Theoretically, the strain sensitivity of a metal conductor under plastic deformation is 2, in the elastic range should to be as close to 2 as possible [7].

The strain gauge selected was the *1-LY13-6/350* by HBM. This strain gauge integrates a specific group of strain gauges to be attached on aluminium, with a nominal resistance of 350Ω. The dimensions of the sensor are $13mm$ by $6mm$, corresponding to c and d in Figure 4.1 [22].
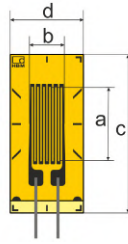
Figure 4.1: Schematic representation of strain gauge series *1-LY1* by HBM [22].

The strain gauge factor is settled to groups of sensors by HBM, this group was a strain gauge factor of $2.11 \pm 1.0\%$. The data sheet of this strain gauge is available in Appendix C.

The number of strain gauges and the orientation depends on the *Wheatstone* bridge used. The *Wheatstone* bridge is commonly an arrangement of four resistances used to compare these resistances with each other [23].

In this case, the resistances are strain gauge, and the types of *Wheatstone* bridge differ in the number of active resistances. There are three possibilities of bridges: quarter-bridge, half-bridge and full-bridge. The quarter-bridge measure the tension, compression or bending using only one sensor, so it does not have compensation on the other directions (*Poisson* effect). The half-bridge uses two sensors perpendicular to each other, allowing to measure the axial deformation with one sensor and the other sensor to shear strain, compensate this way the *Poisson* effect. The full-bridge uses four sensors, two sensors perpendicular to each other and the other two symmetrical on the opposite side of the component. This type of bridge measures the strain with more accuracy because the compensation of the *Poisson* effect and temperature [23]. The three types of bridge set on a probe working on tension are shown in Figure 4.2

(a) Configuration of strain gauge in quarter-bridge.

(b) Configuration of strain gauge in half-bridge.

(c) Configuration of strain gauge in full-bridge.
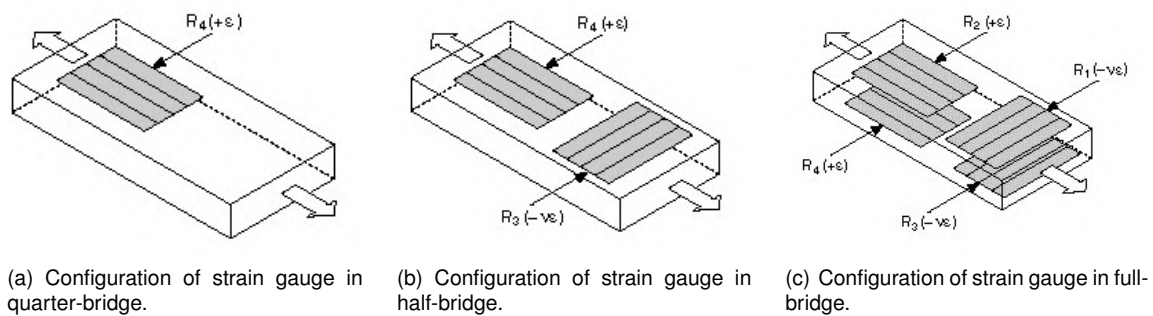
Figure 4.2: Types of bridges in a probe working on tension [24].

The selected *Wheatstone* bridge for this force balance case is the half-bridge, due to the compensation of *Poisson* effect and given the forces on the sensing bars are purely axial. The half-bridge uses less sensors than a full-bridge, this carries less associated costs and simplify the placement of the strain gauges. The reduced bar cross-area will introduce more complexity in the placement pursuant to the number of strain gauges used. The misalignment of the strain gauges can affect the accuracy of the measurements. The half-bridge do not have the same temperature compensation as the full-bridge. However, the temperature is controlled inside the facilities and additional components can be introduced to minimise the temperature effect. The half-bridge needs two additional resistances to complete the

Wheatstone bridge. If the nominal resistance of these two passive sensors is not equal or approximate the nominal resistance of the active sensors, the strain measurement is not the most accurate.

4.1.2 Air Speed Sensor

To obtain the speed of the air flow in the test section, a differential pressure sensor is required. Others forms of compute velocity can also be used such as: thermal, anemometry, particle-based techniques and molecular tagging velocimetry, but the pressure-based measurements are the most common and also the most easy to apply.

The static pressure and dynamic pressure can be related with velocity by the *Bernoulli's* equation and, for low speed, the flow is treat as incompressible, density (ρ) is constant [7]. The velocity is then computed as

$$p_0 - p_s = \frac{1}{2}\rho V^2 \Leftrightarrow V = \sqrt{\frac{2}{\rho}(p_o - p_s)} \tag{4.3}$$

where p_0 is the stagnation or total pressure, p_s is the static pressure, and the term $\frac{1}{2}\rho V^2$ is the dynamic pressure, that relates the density and speed of the stream.

The tool used to take pressure is the Pitot tube, that has two pressure intakes, one for stagnation and another for static pressure, see Figure 4.3 (a).
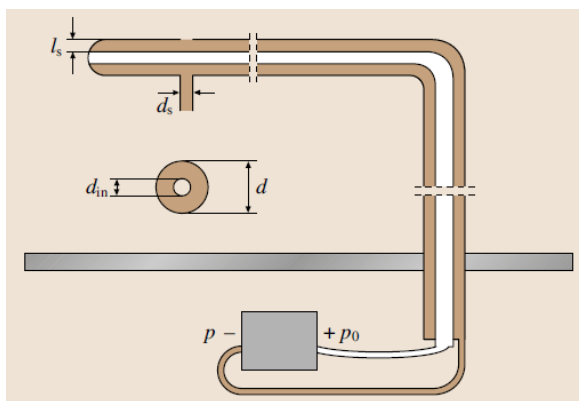
(a) Schematic [23].
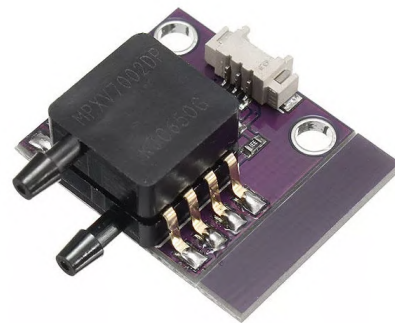
(b) Pressure sensor *MPXV7002DP*.

Figure 4.3: Pitot-static probe and pressure sensor.

The pressure sensor *MPXV7002DP*, see Figure 4.3 (b), is an analogical sensor able to compute the difference between the dual pressure intakes. With a dual intake Pitot tube and a processing system, the system to obtain the flow speed is complete. A processing system simple and affordable to coupling this sensor is an Arduino. The data sheet of this sensor is available in Appendix C.

4.1.3 Temperature Sensor

For the force balance case, the temperature measured will be the air temperature inside the chamber so the range of temperature is small and close to the common environment temperatures. Therefore, the required thermal sensor can be a simple system with a reasonable range. Types of thermal sensors include: thermocouples, resistance thermometers, silicon sensors and radiation thermometers [25].

The *DHT11*, see Figure 4.4, is a temperature and humidity sensor with reduced dimensions, used in several applications. This sensor has a range of temperatures from $0°$C to $50°$C, and of relative humidity from 20% to 90%. This sensor is digital and can be associate to an Arduino for signal processing.
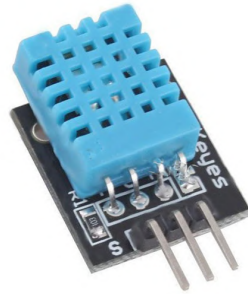
Figure 4.4: Temperature and humidity sensor *DHT11*.

4.1.4 Attitude Sensor

In wind tunnel experiments, the attitude of the model is an important quantity to be measured, this attitude can be translated by the three *Euler* angles. The angles of the model relative to the air flow gives the attitude of the model. Moreover, the side-slip angle and the angle attack need to be set at the beginning of the experiment, so the measurement of attitude is essential.

One way to measure the flow direction is using a multihole probe. This instrument resembles the Pitot tube but has several intake holes for pressure, where the central hole measures the stagnation pressure and the others measure static pressure. The several intake holes are grouped in pairs and each pair is symmetrical to the central hole. Figure 4.5 shows multihole probes and depict the velocity angularly. To operate with a multihole probe, a calibration is necessary, because the angles are determined by comparison with data obtained from there. Therefore, this probes have a limit of operation, normally, it is when the central hole suffer separation phenomenon, around $30°$ in every flow direction [7].
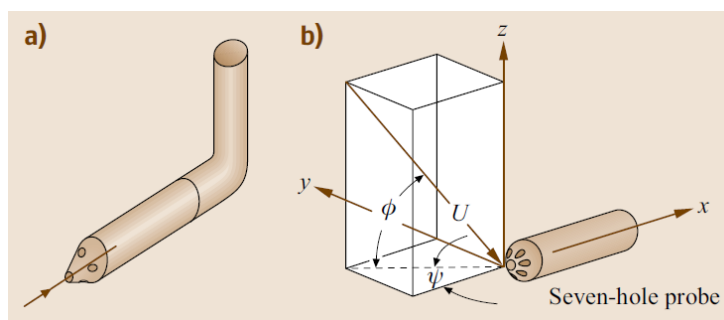
Figure 4.5: Schematic of **(a)** a five-hole truncated-cone probe, and **(b)** a conical seven-hole probe, demonstrating the angular determination of the velocity vector [7].

Inertial sensors can also be used to measure the attitude. An inertial measurement unit (IMU) combines several inertial sensors, being the most common accelerometers and gyroscopes. A gyroscope is used to measure the sensor angular velocity, that means, the rate of change of the sensor's orientation. The accelerometer is used to measure the external specific force acting on the sensor, this force consists in both sensor's acceleration and gravity of earth [26]. The IMU uses a specific process to obtain

position and direction, bringing together the measurements from the gyroscope and the accelerometer because the sensor's orientation, provided by integration of gyroscope measurement, is necessary to the computation of the position with the accelerometer measurement [26]. These two sensors are linked and Figure 4.6 (a) depict the interaction between both.
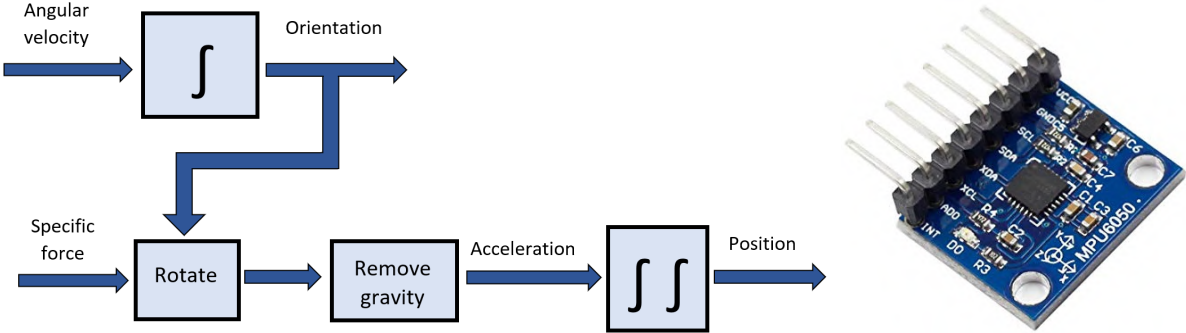
(a) Process of estimating position and orientation, with the use of accelerometer and gyroscope.

(b) IMU sensor *MPU-6050* .

Figure 4.6: Inertial measurement unit working and sensor.

The use of IMU gives more applications than a multihole probe, it is more precise and the processing is faster. The multihole probe also requires a special pressure sensor with multi intakes or several pressure sensor as the *MPXV7002DP* working together. The IMU is a better solution face the multihole constraints and all the advantages carried.

The digital *MPU-6050*, see Figure 4.6 (b), is a typical IMU with three orthogonal mounted accelerometers and three orthogonal mounted gyroscopes. This sensor of reduced dimensions can be attached to a processing system such as the Arduino.

4.1.5 Data Acquisition System

Data acquisition system (DAQ) is a term used to describe the system which transform the electrical output signal from the extensometers into strain values. The selected DAQ must be compatible with the purchased strain gauge, and able to use the chosen *Wheatstone* bridge.

The best solution off-the-shelf for the DAQ is provided by *National Instruments*[TM], the *NI 9237* board, see Figure 4.7 (a). This CompactDAQ is capable of measuring signals from quarter-bridge, half-bridge and full-bridge. Each board has 4 input channels on the form of *DSUB* or *RJ50*, each capable of reading one bridge signal. This DAQ is configured with *LabVIEW*[TM], which is an engineering software for applications that require test, measurement and control, developed by *National Instruments*[TM] [27].

The main reason to consider other options of DAQ is the price around 1.600 € of this board, and moreover it is necessary two boards for the six bridges, one in each sensing bar.

Therefore, building a data acquisition system is an option regarded, which makes this system more affordable, however, further develop and analysis of the system is required and pending to validation. To build a DAQ is necessary a system capable to process electrical signal from load cells. The *HX711* module, see Figure 4.7 (b), is that pursued system. This amplifying module, with a again of 32, 64 and 128, is used in many weight gauges and very versatile due to its reduce size, varied features

(a) *NI 9237*, which *DSUB* and *RJ50* gates, by *National Instruments*[TM] [27].
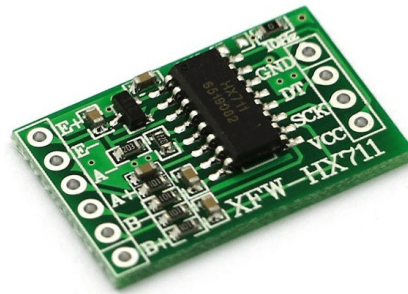
(b) Amplifier module *HX711*.

Figure 4.7: Possible data acquisition systems

and affordable price. Probably, the most interesting feature is the possibility to couple with an Arduino to complete the acquisition system. Additionally, the integration of strain acquisition system with an Arduino is very convenient, due to the possibility to coupling all the sensors together, since the temperature, speed and attitude sensors use this same device as processing system. However, one disadvantages comes up with the use of the modules. That is the necessity of purchase six *HX711* and two Arduinos, a module to each bridge and each Arduino can process signals from three bridges. Although, all these devices make the system larger and less manoeuvrable, the final price is substantially cheaper than a *NI 9237* board.

Fortunately, the Mechanical Engineering Department at Técnico has a *NI 9237* board that provides for testing. This way, the comparison between the built or purchased DAQ can be made without buying the expensive *NI 9237* board.

4.2 Strain Gauge

4.2.1 Placement on the Sensing Bar

To create a half-bridge, two strain gauges are required in each sensing bar, placed on the reduced middle section of the bar. To ensure uniform strain, the strain gauges are placed in the middle of this section and with a clearance of 10mm between both gauges to prevented interference issues, as justified in Section 3.3.1. The strain gauge is placed following the steps:

- Sand the area where the gauge will be placed;
- Make a mark to outline the axis of symmetry of the bar and another mark perpendicular to it. Figure 4.8(a);
- Tape to transcribe the marks, a part of the tape is peeled off and the marks on the surface are cleaned with isopropyl ethanol. Figure 4.8(a) and 4.8(b) ;
- Place the strain gauges on the tape, the vertical and horizontal lines set the gauge positions. Figure 4.8(b);

- Put some glue on the strain gauges and put the tape against the bar again. Press the gauge, using cotton or similar component to not damage the gauge;

- Remove tape after some time and clean surrounding area. Place a paper tape to prevent the wires touching the metal. Figure 4.8(c);

- Welding a cable at each wire output of the strain gauge and fix them to the bar. Figure 4.8(d).

(a) Marker marks on the bar and tape.
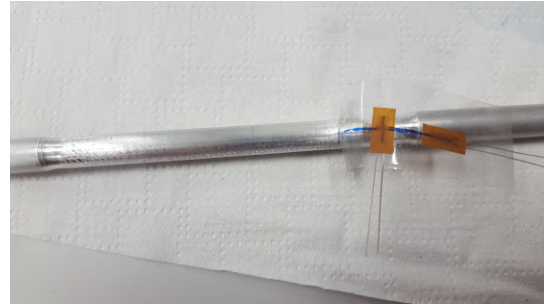
(b) Strain gauges placed on the tape with reference to the marks.

(c) Strain gauges glued to the sensing bar with paper tape to protect the wires output.
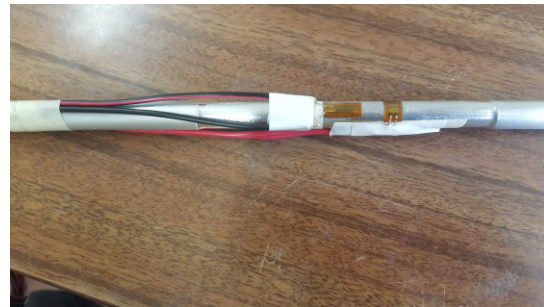
(d) Strain gauges with cables welded and fixed.

Figure 4.8: Steps to place the strain gauges on the sensing bar.

The good measurement of the strain gauge depends on a good placement of the gauges. The placement of the gauges at $90°$ is the most complicated achievement. The use of marks and tape helps to simplify this process. During to placement, the strain gauges require careful handling as they are very fragile when not yet placed on a material.

4.2.2 Calibration of Each Sensing Bar Strain Gauge System

The expected strain response from the bar gauge system is linear with the application of force, since the working regime is elastic making the stress-strain is linear. However, the creation of the physical system is associated with some deviations from the theoretical analyses. A good example to understand this fact is the placement of the strain gauges. If the strain gauge placed to measure the axial strain is not perfectly aligned with the axis of symmetry of the sensing bar, the measured strain will have a slight difference compared to the desired strain. The material imperfections and geometrical deviations are other causes of the difference between experimental and theoretical results. A calibration of the strain response to a well-known loading force will remove any intermediate strain matching process and introduce more accuracy to the force balance.

The calibration procedure consists in loading each sensing bar with a load sequence and taking the strain and the time of each increment weights since its introduction until the introduction of the next increment weight. The load sequence consists of: 5 weights increments of 10N, 3 weights increments of 5N, 2 weights increments of 2N, 10 weights increments of 1N, 2 weights increments of 2.5N, 3 weights increments of 5N and 5 weights increments of 10N. Each weight is verified using a high-resolution scale, see Figure 4.9 (a).

The loading experiment is proceeded through the use of a support structure provided by Mechanical and Material Tests Laboratory and using the *NI 9237* board as DAQ. The experimental apparatus with the complete load set applied and the DAQ is shown in Figure 4.9 (b).

(a) Weighing of an increment weight to setup the load set.

(b) Experimental apparatus with support, complete load set applied and *NI 9237* board as DAQ.

Figure 4.9: Experimental procedure to calibrate each sensing bar strain gauge system.

The experimental data collection is made continuous to not introduce variations in the initial setting configurations. Figure 4.10 shows the strain response to the complete load set for the sensing bar # 1.
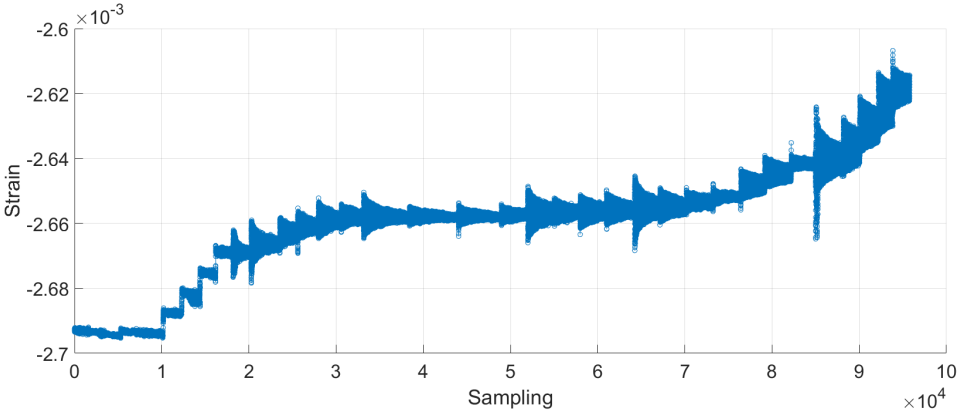
Figure 4.10: Strain response for the complete load set for sensing bar # 1.

Each strain peak corresponds to the introduction of a new increment and the frequency of rating of the DAQ is used to match the number of sampling with the time defined to each increment. The time set for each weight increment varies with the type of force produced by the weight. The time steps varies between 4 minutes for the larger forces and 7 minutes for the lower forces. The duration of the step also depends on the inertia of the sensing bar coupled with the weight probe.

The strain values for each increment was averaged in the most uniform part, the last $30-50$ seconds of the time step. This experimental test was conducted to evaluate the strain when applied a tensile force, as a consequence the compressive force should have the same effect in strain response but a symmetrical signal. Figure 4.11 shows the force for the average strain response for the sensing bar # 6, the tensile and the compressive force are considered.
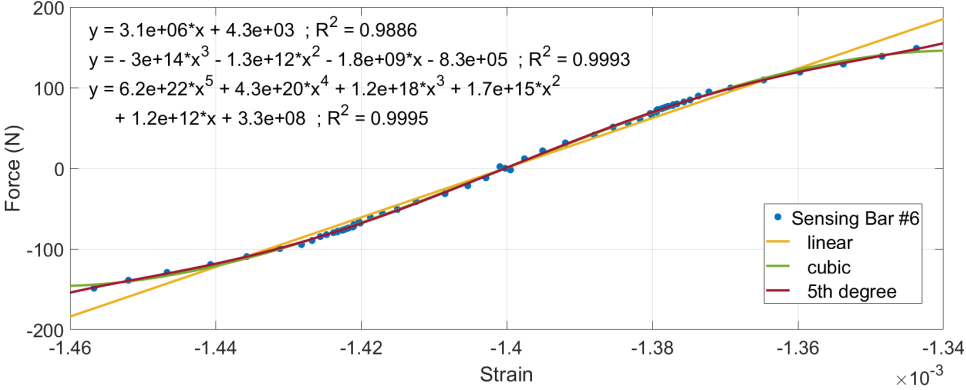
Figure 4.11: Force for average strain response for sensing bar number # 6.

As expected, the response of the strain is not exactly linear but is close for the six sensing bars. Three types of adjustment regressions were made for each bar, 1st order, 3rd order and 5th order, parabolic equations do not fit this case. The parameter of interest is the R^2 of each regression, a R^2 close to 1 present an equation which satisfies better the collected strain points. The R^2 of the three types of regression for each sensing bar are presented in Table 4.1

Table 4.1: Values of R^2 for linear, quadratic and cubic regression for the six sensing bars.

	Sensing Bar					
	1	2	3	4	5	6
Linear regression	0.9988	0.9919	0.9993	0.9993	0.9968	0.9886
Cubic regression	0.9988	0.9991	0.9994	0.9993	0.9981	0.9993
5th order regression	0.9990	0.9993	0.9995	0.9994	0.9982	0.9995

The strain response for the complete load set, the load force for the computed average strain and the all the parameters for adjustment analyses are presented in Appendix D for the six sensing bars.

From the obtained values, the regression that best fits the compromise between a R^2 close to 1 and the computational effort is cubic regression. The cubic calibration equation of each bar should be introduced in the DAQ processing, after the measurement of strain for each sensing bar.

In order to analyse the level of accuracy of this calibration another experimental test was regarded varying the fixation of the sensing bar to the support. In previous test, the fixation was made with a hook system 4.12 (a), in this further test was made with screwing 4.12 (b). This test carrying a response of strain a slightly more stable than with a hook system. However, the loading process was made with the same mechanism and that reveals more crucial than the sensing bar fixation. Due to the lack of facilities to proceed a pure static loading tests, experimental tests to calibrate a single sensing bar were concluded.
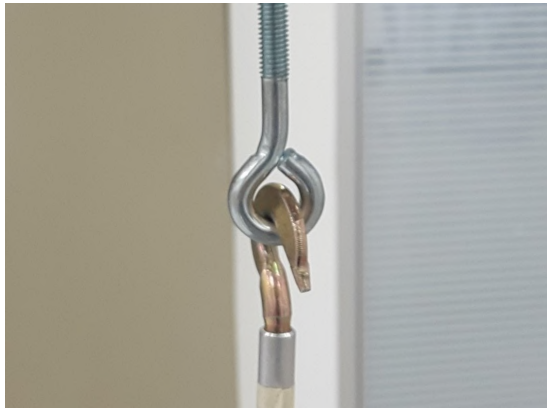
(a) Hook fixation.

(b) Screwing fixation.

Figure 4.12: Type of sensing bar fixation used in sensing bar calibration tests.

However, the calibration tests to obtain the characteristic equation of each sensing bar are just one more step to introduce accuracy in the system. The last experimental test enhance the importance of a calibration test of the complete balance to reinforce the accuracy of it, as performed in Chapter 6.

4.3 Arduino Solution

Nowadays on the market, a large variety of Arduino models are available, the Arduino *UNO* is the most recognised and versatile model. The Arduino *Nano* is similar to Arduino *UNO*, only differ in size, number inputs/outputs pins and energy supply method. Regarding also the purchased sensors, the Arduino *Nano* has the necessary features to process the outputs signals and the size advantages.

4.3.1 Speed, Temperature and Attitude Sensor Setup

Each sensor needs a set of instructions to initialise and compute the quantities through the sensor outputs. This coding for each sensor will be running on the Arduino. The Arduino group developed an open-source software to write programs and upload to Arduino, this software is the Arduino *IDE*, being the most recent version *IDE 1.8.11*. The language used on Arduino *IDE* is similar to `C` and `C++` with special rules of code structuring. Due to the vast number of users and to be public domain, many *libraries* are available to the users. These *libraries* are saved procedure codes for some operations and simplify substantially the coding.

Speed Sensor

To program the pressure sensor *MPXV7002DP* it is necessary relate the analog output and the aerodynamics concepts introduced previous. The difference of the two pressure intakes is the output of the sensor, and is present on the form of voltage. A transfer function provides the conversion of this voltage output to pressure units. The data relative to the transfer functions can be reviewed in the datasheet of the *MPXV7002DP*. The transfer function is depicted as

$$\Delta P = 1000 \left(\frac{5V_{out}}{V_s} - \frac{5}{2} \right) \tag{4.4}$$

Substituting in Equation (4.3) results

$$v = \sqrt{\frac{10000\left(\frac{V_{out}}{V_s} - \frac{1}{2}\right)}{\rho}} \tag{4.5}$$

The sensor output is given in ADC (analog to digital conversion), the conversion to voltage is required. There is a ratio between the voltage and the ADC resolution:

$$\frac{Resolution\,of\,the\,ADC}{System\,Voltage\,(V_s)} = \frac{ADC\,Reading}{Analog\,Voltage\,Measured\,(V_{out})}$$

Since the Arduino has a 10-bit ADC, it means it is able to detect 2^{10} discrete analog levels.

The complete equation to compute air flow speed using the *MPXV7002DP* sensor is

$$v = \sqrt{\frac{10000\left(\frac{ADC\,Reading}{2^{10}-1} - \frac{1}{2}\right)}{\rho}} \tag{4.6}$$

where the *ADC Reading* is the reading from the Arduino. The -1 has add to include 0, and this way create a range of $0 - 1023$ that corresponds to the voltage the pin is reading.

The coding of this sensor is complete with logical procedures to average the values in time steps. The coding and tests individual with *MPXV7002DP* were made for a constant density provided from bibliography.

Temperature Sensor

The sensor *DHT11* provides digital output of values in final user reading form. However, the *DHT* sensor library needs to be called in the code to relate the pins and the logical processing of the sensor. The code follows the most simple structure sequence of the Arduino IDE and the print output is temperature in °C and relative humidity in %.

Attitude Sensor

The *MPU-6050* sensor needs two libraries to configure the accelerometers and the gyroscopes. Consequently, the initialisation of the sensor prescribe an initial position, the default position of the sensor. However, the initial position should be a position set by the user. The additional *MPU6050_calibration* code was created to reset the sensor to a desired initial position. It returns six values with establish the actual sensor position, three values for the three accelerometers and another three for the three gyroscopes. Figure 4.13 (a) presents the output of the *MPU6050_calibration* script here the six offsets can be seen for an example test.

(a) Offset values from *MPU6050_calibration* script.   (b) Excerpt of the main code to insert offset values.

Figure 4.13: Reset the attitude sensor position to the current position.

These offsets are then introduced in a specific part of the *MPU-6050* code, see Figure 4.13 (b). This way, the actual position of the sensor is the reference for further computations.

The rest of the code was made to give to the user the variation of *yaw*, *pitch* and *roll* in degrees, measured form the initial position. The angle of attack and side-slip can be set with the variation of *pitch* and *yaw*, respectively, and then a new reset is made to analyse the response of the model to the flow interference with this variations.

4.3.2   Coupling of the Three Sensors

Each sensor was individually tested after the code been completed and validated, one Arduino had enough input pins and processing power and memory to handle the three sensors.

The first task to be made is the connection of sensor pins to the Arduino. Each sensor requires one power supply and one ground, the outputs pins vary with the sensor. The pressure sensor had one analog pin, the temperature sensor had one digital pin and the attitude sensor had three pins, two analog and one digital. The schematic wire connection to the Arduino is shown in Figure 4.14.
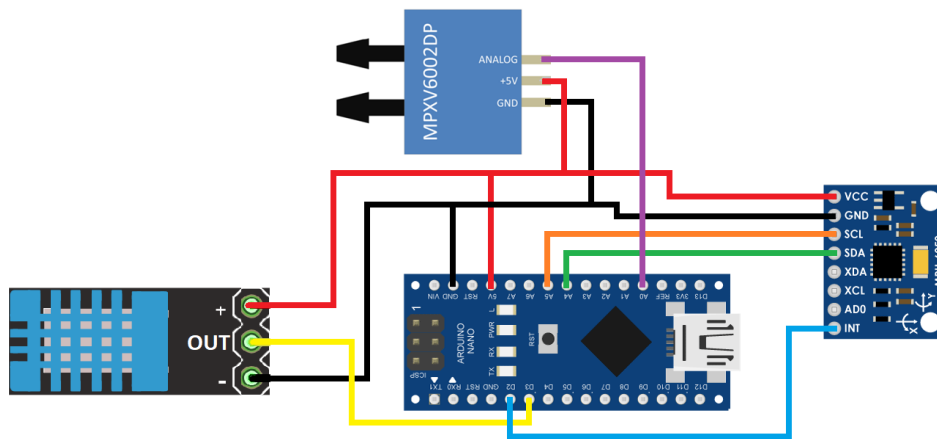
Figure 4.14: Wire connection scheme of the pressure, temperature and attitude sensor with the Arduino.

The final acquisition code is a merger of the three individual codes which process the three quantities at the same time in loop. A time step of 1 second was set to present the outputs. In this acquisition code, the measured temperature is used to compute the air density through the ideal gas law $p_s = \rho R_{specific} T \Leftrightarrow \rho = \frac{p_s}{R_{specific} T}$ where $R_{specific}$ is the specific gas constant. The pressure required to complete the computation is the static pressure. To measure and introduce the real time pressure in the system, a static pressure transducer should be implanted in the future. However, it was selected to introduce a constant static pressure in the acquisition computation provided by weather briefing for the day or by an off-the-shelf barometer.

4.3.3   Strain Gauge Signal Amplification Tests

To implement the DAQ built with amplifiers, the validation of the values produced from its was mandatory. Regarding this, experimental tests were made with one sensing bar using the *HX711* module and an Arduino.

The *HX711* module connects the Arduino to a sensing bar. The plug between the Arduino and the module is straightforward, power pin, ground pin and two digital pins. The other part of the system is the connection of the *Wheatstone* bridge with the module, a half-bridge was the selected bridge type and follows a particular scheme. The complete connections of the strain gauge acquisition system using a Arduino, a *HX711* modules and a half-bridge are depicted in Figure 4.15 (a).

(a) Electric circuit diagram.　　　　　　(b) Hardware implementation on breadboard.
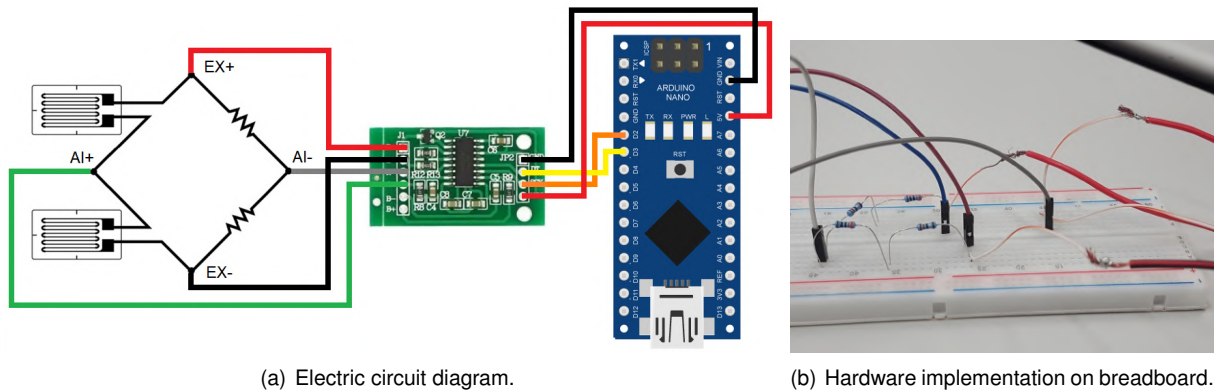
Figure 4.15: System to compute strain with a half-bridge, a *HX711* module and an Arduino.

The *HX711* module does not have an integrate circuit to compensate the lack of the two gauges as the *NI 9237* board. Therefore, a complete bridge was created with two active strain gauges from the sensing bar and two external passive gauges. The strain gauge has a nominal resistance of 350Ω but since resistances with this value are not common, each external passive gauge consisted of two resistances in series of 330Ω and 22Ω. Figure 4.15 (b) shows the created bridge with the two strain gauges and the four resistances.

Bridge Signal Measurements

Before any test, the developed bridge was tested with an oscilloscope by ISO-TECH, the *IDS 6022*. The signal variation between the power and the ground and between the two reading points was an approach to understand the orders of magnitude of the voltages measured in the bridge.

The measurement between the power and the ground gives a maximum voltage (V_{max}) of 3.73V and a voltage peak-to-peak (V_{pp}) of 40mV, see Figure 4.16 (a). From the measurement between these two point it was concluded that the power supply was constant, the V_{max} did not change and the V_{pp} had only occasional slight variations. This establishing was not defined a priori due to the power supply provided to the bridge comes from the Arduino and cross the amplification module. Electric power supplied by an external source can introduce signal variations.

The measurement between the positive and negative reading points was noisy in V_{max} and V_{pp}. The V_{max} varied between -1.6mV and 25.6mV, the V_{pp} varied between 9.6mV and 53.6mV. Figure 4.16 (b) shows an instance in the voltage measurement. This translates the large accuracy of the strain gauge, which introduces small voltage variations despite the sensing bar being static.

Operational Amplifier

The DAQ considered to the force balance was always digital processing. Consequently, a test with an operational amplifier (op-amp) was made to validate this initial assumption. An op-amp is an electronic device that amplifies the coupled direct voltage with a differential input and single output. The op-amp
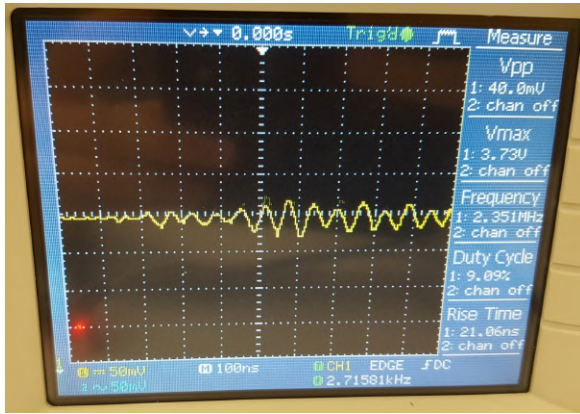
(a) Between the power and the ground pins.
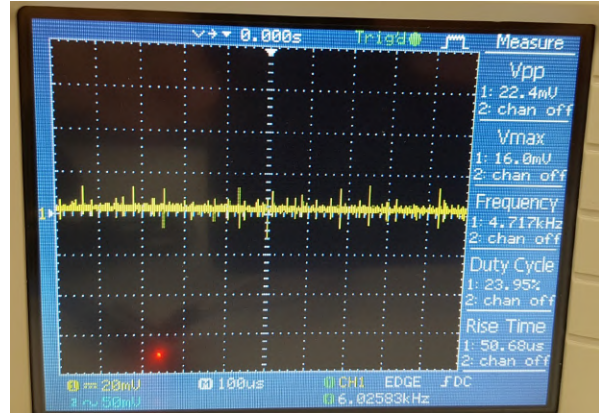
(b) Between the positive and negative reading pins.

Figure 4.16: Signal measurement in the bridge with the oscilloscope.

is very versatile and can be used to test the bridge in terms of signal amplification in this case. Figure 4.17 (a) shows the circuit diagram for a differential operational amplifier.
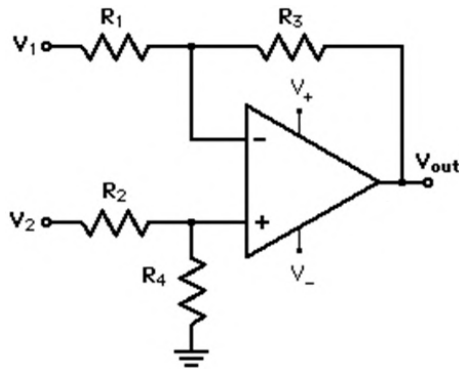
(a) Circuit diagram.
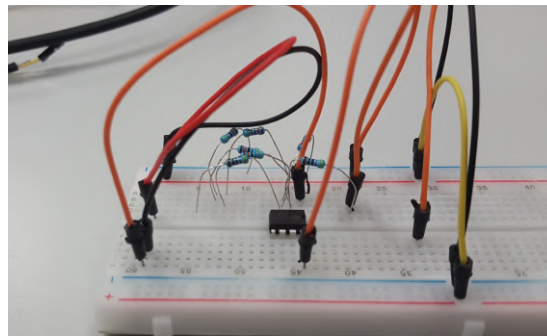
(b) Hardware implementation on breadboard.

Figure 4.17: Differential operational amplifier.

The selected resistances will set the gain of the amplifier. The gain obtained from the circuit analysis is

$$V_{out} = V_2 \frac{(R_3 + R_1)R_4}{(R_4 + R_2)R_1} + V_1 \frac{R_3}{R_1} \tag{4.7}$$

Given this, an differential operational amplifier was created with a *LMV358* operational amplifier and resistances of 470Ω and 470kΩ to obtained a gain of 1000, see Figure 4.17 (b). This op-amp was connected to the bridge reading pins and the V_{out} to an analog input of the Arduino. Some loads were applied to the sensing bar. But neither increments of 1N or increments of 10N had a response of voltage variation. As expected, the analog system does not have the resolution necessary to measure those weight increments with this bridge, although the gain is high. This problem is solved with a digital system. In addition, a feature that was not validated in this experiment is the stability of the response with a digit system, due to, the stepped and discrete signal provided by them.

HX711 Loading Tests

To test the *HX711* module, a load set was defined to confirm that this acquisition can detect 1N increments when loading the bar, as achieved with the *NI 9237* board and the external strain indicator. The load set consisted of nine weight increments in this specific order: the weights support of ≈ 2N, three

≈ 1N weights, three ≈ 2N weights, two ≈ 5N weights and one three ≈ 10N weight. As in the previous loading tests, all weights were calibrated in a high-precision scale before the loading sequence.

The *HX711* amplifies an analog input signal and outputs a digital signal in bits. This is the lowest level way to collect data from the module, in which each state of the module is linked to a byte. The loading tests should confirm if 1N increments are enough to change the current state/byte.

The output of the complete system was not as desired, since the measured values were not steady for a static bar test with no load. This is a consequence of the high accuracy of the strain gauge, the *noise signal* is not filtrated and is not as constant as it should be. In order to have a more reliable state value, a time step was defined for each load increment and the values averaged. This process was the same as the one used in the calibration of each sensing bar. The defined time step was 8 minutes, corresponding to around 5000 measurements from the system. Figure 4.18 (a) shows the bytes values obtain for the first loading test. From this first load set, it was concluded that the module does not have a successful response for increments of 1N. However, the increments of the second 5N and the 10N weights had a more linear response, despite the response of the first 5N was the opposite of what was expected.

(a) First load set.
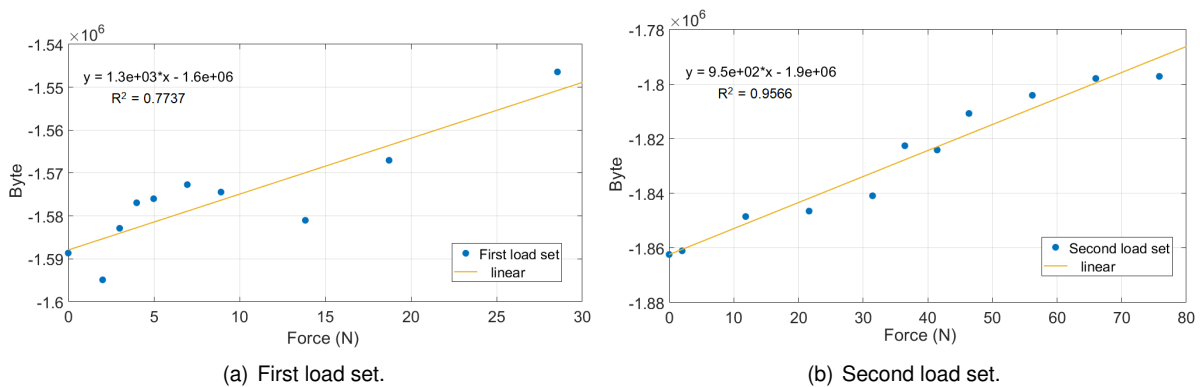
(b) Second load set.

Figure 4.18: Byte response of the *HX711*.

To validate the module for higher weight increments, a second load set was applied. This load set is a sequence of weight increments composed of: three 10N, three 5N and three 10N.

The response of the *HX711* for the second load test is presented in Figure 4.18 (b), showing acceptable response for higher loads, which is a completely expected since this module is designed for less sensitive systems such as weight scales for everyday use or loading tests with layers. However, both cases use a different approach to compute the deformation than the one used in this force balance. The weight scales use load cells that work in bending, creating more deformation and consequently a better measurement of the strain gauges. In the loading tests with layers, the object of study is placed over a test probe instrumented with strain gauges, the loads suffered by the object are transmitted to the testing probe that measures the deformation. These test probes are made of wood or cork composite to be very sensitive to deformations.

Despite the *HX711* module responding to higher loads, the signal is oscillatory. This type of signal response was also obtained with the *NI 9237* board when the calibration of each sensing bar was made. Figure 4.19 compares the response obtained with the module and the board for three increments of

10N, from the introduction of the first weight to the introduction of a fourth weight, and takes into account the time for each increment to average the values: 8 minutes using the *HX711* module, compared to 4 minutes using the *NI 9237* board.

(a) Response with the *HX711* module.

(b) Response with the *NI 9237* board.
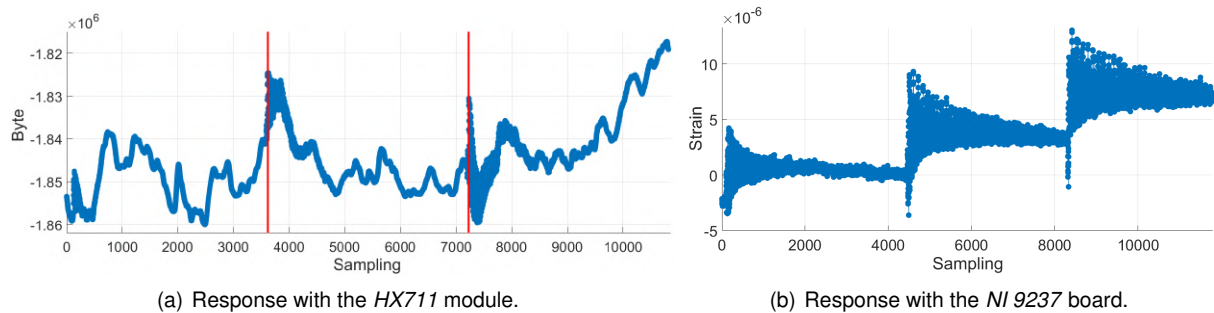
Figure 4.19: Response signal for a sequential increment of three weights of 10N.

The response of the *NI 9237* board is much more stable and faster than the response of *HX711* module. This happens because the *NI 9237* board is an amplifier with internal circuits integrated specifically to filter and clean the signal from a strain gauge bridge. In addition, the internal circuit to simulate a full-bridge is more accurate than using external resistances. The difference between both system is clearly visible and the price difference is justified by these features.

In conclusion, the *HX711* module is not an adequate data acquisition system and the same is applies to an operational amplifier alone. To make a DAQ more reliable and affordable from scratch, it is necessary to provide an amplifier with additional systems to create a more stable output from the bridge and frequency analyses to filter the noise, but this is out of the scope of this work.

4.4 Data Acquisition *NI 9237* Board

Given the analyses in the previous section, the *NI 9237* board provided by *National Instruments*[TM] was selected for data acquisition.

The board is available with two different input gate types, *DSUB* and *RJ50*. The pinout for the two board types is shown in Figure 4.20. The selected gate type was the *RJ50* due to its versatility and ease to connect the pins.

To correct a full-bridge, the connection is made like the connection of the *HX711* to the bridge, the pin EX+, EX-, AI+ and AI- are linked to each bridge wedge [28]. In the case of an half-bridge, this same connections can be made if it is made a complete bridge with external resistances. However, the *NI 9237* has a internal system with replace the use of external resistances to complete the bridge, this system is more stable and more practical to use. The connection of an half-bridge to the *NI 9237* board is depicted in Figure 4.21 (a). From this scheme, the half-bridge will use only the *RJ50* pin gate numbers 1,2,6,7 and 10.

To slip a *RJ50* gate into single gate pins inputs, a screw-terminal accessory can be used or an equivalent adapter. An example of RJ-50 to screw-terminal accessory is the *NI 9949*, see Figure 4.20 (b), by *National Instruments*[TM]. This accessory is useful to use different bridge configuration and testing
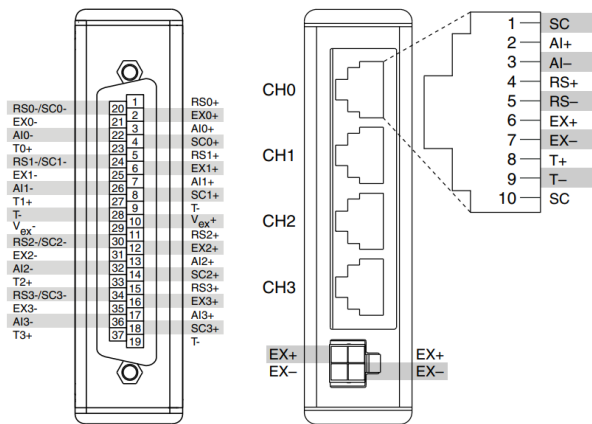
(a) *NI 9237* input signals [28].

(b) *NI 9949* RJ-50 to Screw-Terminal Accessory.

Figure 4.20: *National Instruments*[TM] instrumentation.
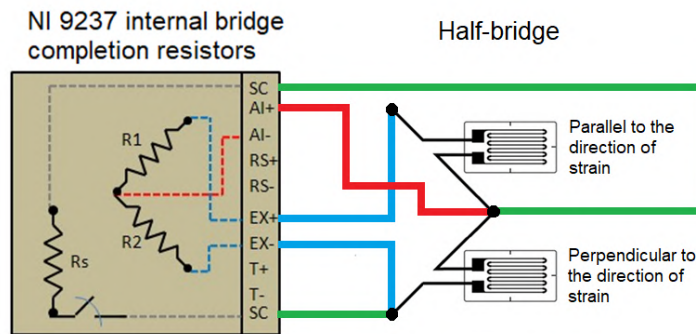
Figure 4.21: Connection between a half-bridge and a *RJ50* gate on the *NI 9237* board.

cases with the *NI 9237* board as it was the case of the calibration of each sensing bar and strain gauge system. However, the final solution for the aerodynamic force balance will use definitive *RJ50* plugs crimped to the sensing bar wiring for the connection to the *NI 9237* board.

4.5   User Interface

The user interface, created with *LabVIEW*[TM], gathers the necessary parameters to provide the aerodynamic forces and moments in the final form.

The set of the strain gauge options initialise the process. The interface is made to alternate the bridge type, the initial voltage, gage factor and resistance. In this way, the interface is adjustable to a larger part replacement options.

Regarding the operational process of *LabVIEW*[TM], two physical channels were created to read the signal from the two *NI 9237*, each channel collects three bridges data. The sequence of channels must be fixed due to the further computations where the channel is linked to a sensing bar strain gauge calibration formula to convert the strain reading into sensing bar force. The sensing bar forces, in turn, are computed into aerodynamic forces and moment by the calibration coefficients that will be introduced in Chapter 6.

The additional settings of the user interface define the number of samples per loop to average the

49

data, the clock of the *NI 9237* and extra features of the board to future implement if required. The user interface saves the three aerodynamic forces and the three aerodynamic moments into a *.TDMS* file that is opened with a support version of Microsoft™ Excel.

Figure 4.22 presents the user interface in *LabVIEW*™. The instantaneous values of forces and moments can be seen on numerical and graphical form. The saved file stores the numerical values of the aerodynamic quantities for all the samples into six columns, each column corresponds to a force or moment component.
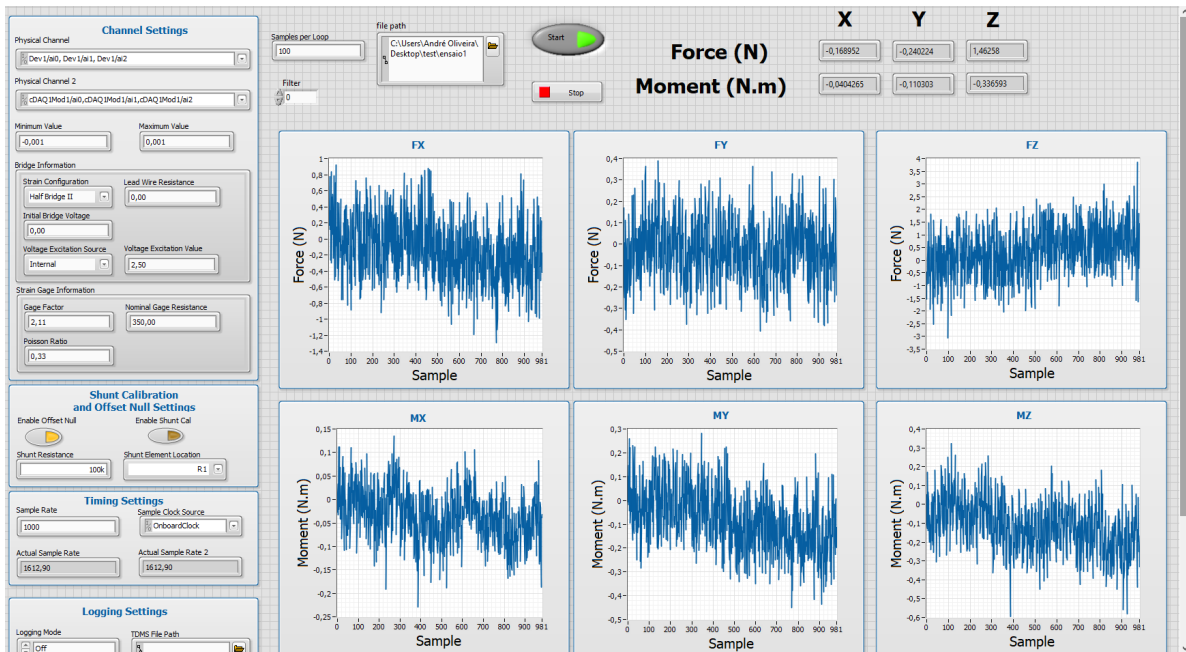
Figure 4.22: User interface.

The additional instrumentation process the data through different software. Therefore, the *Lab-VIEW*™ and the Arduino *IDE* should run at the same time. The additional instrumentation provides the air flow speed, temperature, humidity, and the model *yaw*, *pitch* and *roll* angles. Figure 4.23 shows how the output of this complementary instrumentation is presented to the user.
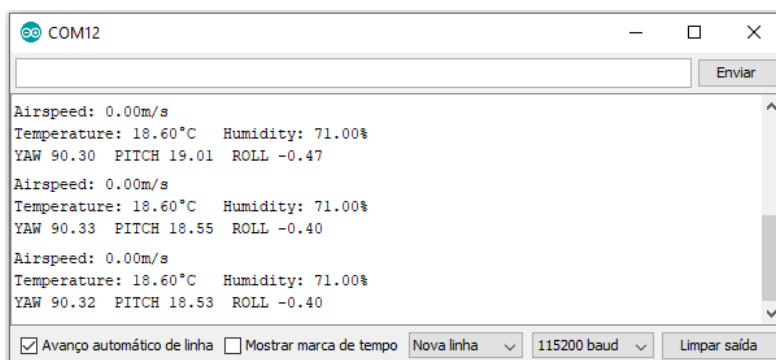
Figure 4.23: Outputs from the acquisition code for pressure, temperature and attitude sensor.

Chapter 5

Manufacturing and Assembly

This chapter presents the work required to build the aerodynamic force balance designed in the previous chapters. It includes two major sections, the manufacture and assembly. Manufacture involve the activities to develop the part components as a final product. Assembly is the coupling of all the parts to produce a final product, both mechanical assembly concerning all structural components and electrical assembly concerning the integration of the instrumentation.

5.1   Overview

The force balance is composed by several parts as described in Chapter 3. The acquisition of the parts were planed when the design was being carried out. Some of the designed parts correspond to an off-the-self product to simplify the acquisition. Therefore, the rest of the parts are manufactured.

The manufacture of the force balance parts can be outsourced or made in-house. The selection of manufacture is strongly dependent on the form in which the raw material is provided and the facilities required to machine it. Table 5.1 shows the type of acquisition for each force balance part previously identified in Figure 3.16 and a brief explanation of the manufacturing tasks.

5.2   In House Manufactured Parts

The manufacture is done in *Laboratório de Técnicas Oficinais* (LTO). LTO is a laboratory of Mechanical Engineering Department with several machines available, open for students to have a direct contact with workshop reality. The works are done by the students with the orientation and supervision of the responsible employees.

Only the manufacture of force balance components will be describe in this section, other works were done to create parts for integrating the components. These parts are introduced during the assembly description.

Table 5.1: Force balance parts, type of acquisition and description of manufacture tasks.

Item number	Part name	Quantity	Type of acquisition	Description
1	Fixed platform	1	Outsourced manufacturing	Cutting of a solid block with the respective dimensions.
2	Coupler	12	Outsourced manufacturing	Cutting and bending of a plate to component final dimensions
3	Rod end bearing-right	6	Purchase	Final product.
4	New moving platform	1	Outsourced manufacturing	Water jet cutting of a sheet with the respective dimensions.
5	Rod end bearing-left	6	Purchase	Final product.
6	New sensing bar	6	In-house manufacturing	Cutting and turning a tube to component final design.
7	Rotating collar	1	Purchase	Final product.
8	Table	1	Outsourced manufacturing	Cutting of a solid block with the respective dimensions.
9	New flange	1	In-house manufacturing	Turning and facing of solid block to component final design.
10	New strut	1	Purchase	Final product.
11	Alpha adjustment 1	1	Outsourced manufacturing	Cutting and bending of a plate to component final dimensions.
12	Alpha adjustment 2	1	Outsourced manufacturing	Cutting and bending of a plate to component final dimensions.

5.2.1 Sensing Bars

The manufacture of the sensing bar starts from a regular tube, with a inner diameter of 7mm, a outer diameter of 10mm and a length of 1m.

The first step is to cut the tube to the correct length of the sensing bar plus a small tolerance. This cut is made with an hacksaw and the precision of the cut is not important. The final length is set by facing both sides of the tube on a lathe.

The next operation is also on the lathe to reduce the middle section of the sensing bar by grooving. This process will cut the tube to a specific depth and applying an automatic advance will roughing a specific length. A typically turning tool is used complemented with a circular turning insert. The circular type was selected for grooving the 10mm of material without introducing sharp transitions in the tube. The created fillets lead to less stress concentrations than the predicted in the computational tests includes in Section 3.3.1 due to the chamfer stress theory [19]. The turning tool with a circular turning insert, the tube in the lathe and the manufacture process are depicted in Figure 5.1 (a).

The sensing bar manufacture is conclude with the opening of a left and right female thread in each side of the tube. This process is made with a tap tool corresponding to a *M8* left and right male threads,

respectively, see Figure 5.1 (b).

(a) Machining with a lathe and a circular turning insert.

(b) Creation of female thread with a tap tool.

Figure 5.1: Manufacture of the sensing bar.

5.2.2 Flange

The flange is manufactured from solid circular block of aluminium, see Figure 5.2 (a). The same lathe is used, and the tasks involve roughing, parting and facing processes to create the final design. Each process use different turning tools. The intermediate process creates a part with coupling three different cylinders. The cone is creates by roughing the middle cylinder with a diamond turning insert with the necessary slope for the desired geometry, see Figure 5.2 (b). The final dimensions of length are always set by facing the surfaces. Until the facing process, all the length dimensions have an associated tolerance. The internal flange hole, where the strut is placed, is made by drilling on the lathe.

(a) Solid aluminium block to machining.

(b) Turning on the lathe.

Figure 5.2: Manufacture of the flange.

The flange is concluded with six adjacent drills to fix the strut and the moving platform to it. A female thread is created in the three holes in the vertical cylinder to screw in three pins that will fix the strut. This female thread is made with a tap tool corresponding to a *M5* male thread, which is the size of the fixing pin screw.

5.2.3 Pitot Tube Support

The pitot tube support is a component that was not introduced in the design. The need of this component arose when the force balance was assembled to integrate the pitot tube. This instrument

must be placed in a section of uniform air flow but must not interfere with the model. The more beneficial region to place the pitot is below the alpha adjustment and above the lower limit of the wind tunnel nozzle. Therefore, the solution was to create an additional support attached to the table for the placement of the pitot tube, on the front of the force balance.

The pitot tube support is composed by a fixation part and a plate. The fixation part connects the plate to the table, and the pitot tube is placed on the top of the plate. The plate geometry was selected for reduced air resistance. The total length of the plate is 1m, but the plate and fixation have several pairs of holes which allows to set different heights from the table to the pitot tube, adjust for each type of test model. The support is made of steel, with a thickness of 5mm, to prevent the occurrence of flutter.

The fixation part is made from an angled beam. The main support manufacturing processes was cutting and milling, see Figure 5.3 (a). The other process was drilling two hole for fix the support on the table and four hole to fix the plate to the fixation. A female thread is created on the two hole that will fix the fixation on the table, the plate locking system is bolt and nut. Figure 5.3 (b) shows the fixation part of the pitot tube support that fix on the table and the plate.

(a) Milling of the pitot support fixation.   (b) Fixation part of the pitot support fixation.

Figure 5.3: Manufacture of the pitot support fixation.

5.3 Bill of Materials

Table 5.2 presents the materials required to manufacture the components, the purchased components, the purchased instrumentation and the additional parts for assembly. In this table, the cost is shown, as well as the supplier. Some specific tools were acquired but their costs are not considered for the cost of the force balance. The same applies to the test instruments, for instance the *HX711*.

Figure 5.4 presents the distribution of the aerodynamic force balance costs. The highest cost are the electrical parts, and the data acquisition system is the most expensive component of the force balance. As noticed before, an attempt to create a DAQ could markedly reduce the overall solution costs.

5.4 Assembly

The assembly is composed by mechanical, electrical and their coupling. The mechanical assembly was made entirely in LTO. The electrical assembly was made in the Mechanical and Material Tests

Table 5.2: Force balance costs breakdown.

	Product	Supplier	Quantity	Price (€)
Mechanical	Table	Peçolopes, Lda	1	121.52
	Fixed platform	Peçolopes, Lda	1	117.86
	Coupler	Peçolopes, Lda	12	210.18
	Alpha adjustment 1	Peçolopes, Lda	1	69.86
	Alpha adjustment 2	Peçolopes, Lda	1	69.37
	Rotating collar	Casauto, Lda	1	57.58
	Rod end bearing (INA GAL8-UK)	Enriel, S.L.	6	115.79
	Rod end bearing (INA GAR8-UK)	Enriel, S.L.	6	115.79
	New strut	Poly Lanema, Lda	1	9.84
	Tubo redondo $10\text{x}1,5$ mm (1m)$*$	Poly Lanema, Lda	6	9.84
	Circular block ø130mm (0.08m)$*$	Poly Lanema, Lda	1	36.75
	New moving platform	Poly Lanema, Lda	1	97.42
	Angle beam, plate and block $*$	Técnico	-	8.83
	Rubber supports for table	Borrachas E Plásticos Berna, Lda	8	11.32
	Bolts, nuts, rings, insulating tube, clamps	Aki[©] ; Leroy Merlin[©] ; Mário Mendes, Lda	-	18.37
Subtotal				1070.32
Electrical	Strain gauges (*1-LY13-6/350*)	HBM [©]	30	247.95
	Attitude sensor *MPU-6050*	PT Robotics, Lda	1	6.09
	Temperature sensor *DHT11*	PT Robotics, Lda	1	3.69
	Pressure sensor *MPXV7002DP*	Amazon, Inc	1	12.79
	Arduino nano	PT Robotics, Lda	1	11.00
	DAQ *NI 9237*	National Instruments[TM]	2	2790.00
	Cables, connectors, RJ50 plugs, boxes, hoses, USB hub, USB extension cable	PT Robotics, Lda ; Tetraluz, Lda ; HP modelismo, Lda ; Robert Mauser, Lda	-	55.87
Subtotal				3127.39
Total				4197.71

$*$ Raw material for the manufacture of the force balance component.
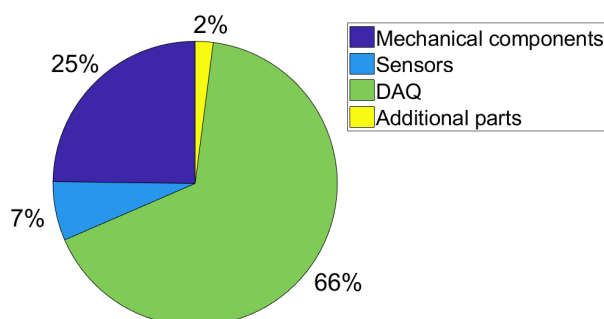
Figure 5.4: Distribution of the force balance costs.

Laboratory and the Aerospace Engineering Laboratory at Técnico. The final assembly was done in the Aerospace Engineering Laboratory.

5.4.1 Mechanical

Despite the outsourced manufacturing of components, some machining processes were required to finalise the components for the assembly.

It is the case of the table and the rotating collar. The fixation of these two components is made through bolts and nuts. Both of the components are not drilled, therefore, this process is made to create 6 matching holes for the two components. The table works are concluded with 8 more holes for coupling rubber supports for stability and elevate the metal sheet. This rubber support use a two nut system which provide the levelling of the table. Figure 5.5 (a) depict the assembly of the force balance until this stage.

The bottom base of the force balance was complete with the fixed platform and the 6 correspondent couplers. The drilling process was required again to the fixed platform and the rotating collar, the couplers were on the final form. The fixation was made through bolt and nut, ensuring that the coupler bolts did not to interfere with the table during any rotation movement. Figure 5.5 (b) shows the complete bottom base of the force balance.
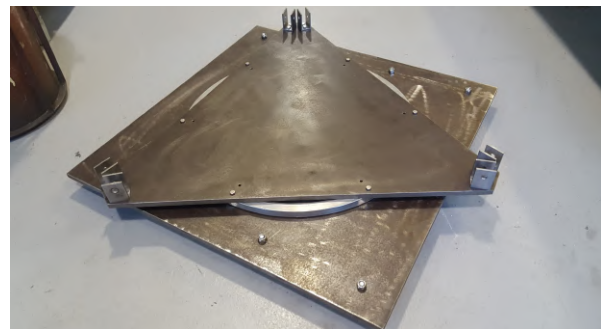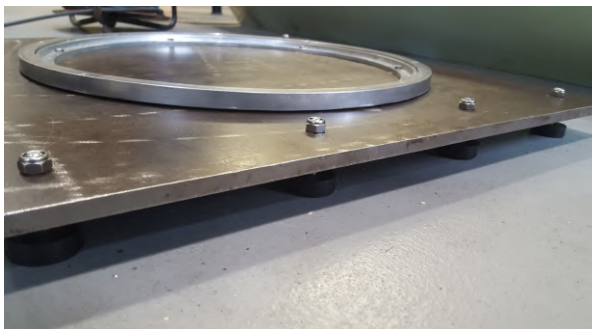
(a) Middle stage with rubber supports, table and rotating collar.

(b) Complete base with fixed platform and the 6 correspondent couplers.

Figure 5.5: Bottom base of the force balance.

The sensing bars and the rod end bearings were the next components to assemble. The strain gauges were already placed on the sensing bars through the procedure explained in Section 4.2. This strain gauges are very delicate to impacts and temperature so an insulating tube was used to cover the sensing bar. This coating tube was attached to a sensing bar using an adjustable plastic clamp in the upper end. The labelling of each sensing bar is done on the middle of the insulating tube. Figure 5.6 (a) shows the sensing bar # 1 with coating.

The good fixation of the rod end bearing and the sensing bar is crucial because rotation movements can introduce unscrewing of this system. Therefore, a special glue for threads was introduced in the rod end bearing male thread before the screwing. The screwing of the two rod end bearings for each sensing bar was simultaneous to ensure the totally of the male thread was screwed and the rod end bearing heads were align. Figure 5.6 (b) shows the glued fixation of the sensing bar and the rod end bearing.

The next part assembly completed the upper base of the force balance. The moving platform holes to couple the flange and couplers were drilled. The fixation was made by bolt and nut. Once again,

(a) Sensing bar coated with insulating tube.

(b) Fixation of sensing bar and rod end bearing using glue.

Figure 5.6: Assembly of the sensing bar and rod end bearing.

the length of the bolts was adjusted so as not to interfere with the rod end bearing moving underneath. Figure 5.7 (a) shows the assembled upper base.

During the assembly of the bottom base, the sensing bars and the upper base, it was found that some coupler edges of the upper base did not allow the complete assembly of the 6 sensing bars. The solution was adapt the upper base couplers, cutting the edges that created interference. This new design for the 6 couplers is presented in Figure 5.7 (b).

(a) Upper base with the initial couplers design.

(b) New design adapted for the couplers.

Figure 5.7: Assembly of the upper base of the force balance.

With the upper base ready, the final coupling of the sensing could be made. Some parts were required for this assembly. First, the pin which cross the coupler and truss the rod end bearing, the 12 pins were made of leftover bar available at the LTO. These pins require cut, sanded and drilled processes. The other parts necessary to assembly were brass rings to fix the rod end bearing in the middle of the pin with a tight fit. Figure 5.8 (a) shows the sensing bar rod end bearing system fix on the coupler pin by the two rings, the pin have two cotters to stop its slide. The 6 sensing bars were assembled first in the upper base. The next assembly with the bottom base was made with the help of an hoist, as seen in Figure 5.8 (b).

The strut and the alpha adjustment were the last parts to be assembled. The union between the flange and the strut was made by bolt. To fix the alpha adjustment on the strut, this type of unions are impossible to apply, therefore, part of the alpha adjustment was welded to the strut. The other complementary part of the alpha adjustment is fixed by bolt and nut. A inner ring was created and applied in the alpha adjustment so that it does not bend when the bolt is tightened. Figure 5.9 (a) shows the strut and the alpha adjustment configuration.

(a) Developed system to attach and fix the rod end bearing.

(b) Apparatus with hoist to assemble the upper base with the sensing bars mounted.
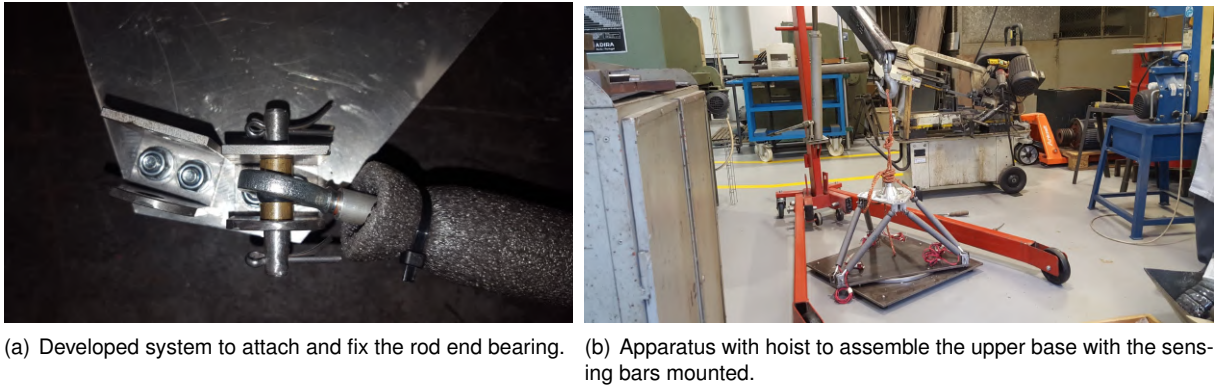
Figure 5.8: Assembly of both bases and sensing bars of the force balance.

The last mechanical task was to fix the rotating collar in a known position to set the reference side-slip ($\beta = 0°$). Two holes were made in the fixed platform and the table, each hole is placed in one symmetry axis of the horizontal plane of the component. A pin was manufactured to cross both holes and fix these two components, see Figure 5.9 (b).

(a) Strut and alpha adjustment.

(b) Rotation fixation pin.
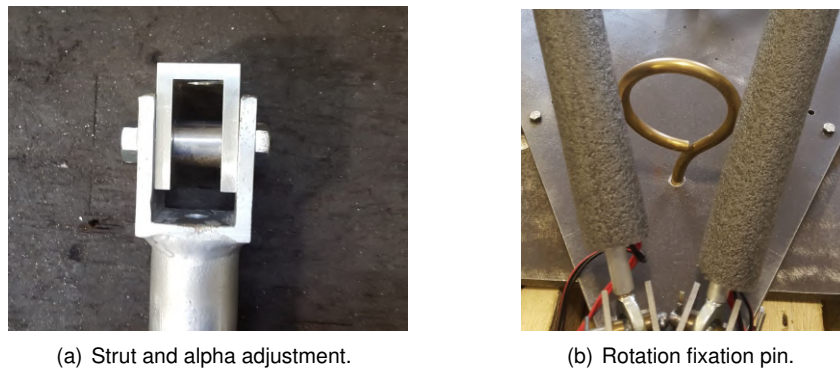
Figure 5.9: Finalisation of the mechanical assembly.

5.4.2 Electrical

The assembly of the sensor followed the wire scheme presented in Figure 4.14. The temperature and the pressure sensors did not need any additional wiring since they were placed on the fixed platform near the Arduino. An additional 2m cable added to the attitude sensor to allow its placement on top of the strut or on the aircraft model. Figure 5.10 shows the assembly of the three sensors on the Arduino. In this figure, the hose which connects the pressure sensor and the pitot tube is representative and was only used for instrumentation setup tests.

To connect the strain gauges to the data acquisition, *RJ50* plugs were made to replace the acquisition of 6 *NI 9949* accessories. According to the connections presented in Figure 4.21. Two steps assembly will implement this concept. First step was to create a *RJ50* plug by crimping a *RJ50* connector to a 10 components cable using a *RJ50* crimping plier, see Figure 5.11 (a). The second step was to weld the strain gauges wires to the corresponding 10 components cable wires, see Figure 5.11 (b). The assembly was completed by coating the welds using heat shrink tubing, a second coating of the entire
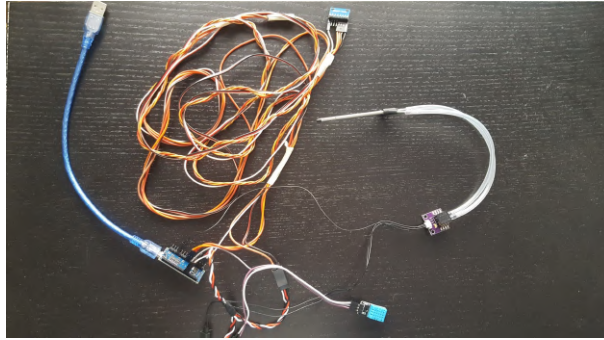
Figure 5.10: Assembly of the pressure, temperature and attitude sensor on the Arduino.

union and identifying the sensing bar corresponding to the plug. Figure 5.11 (c) shows the assembled cable required to provide the strain data from the gauges to the DAQ before the last coating.
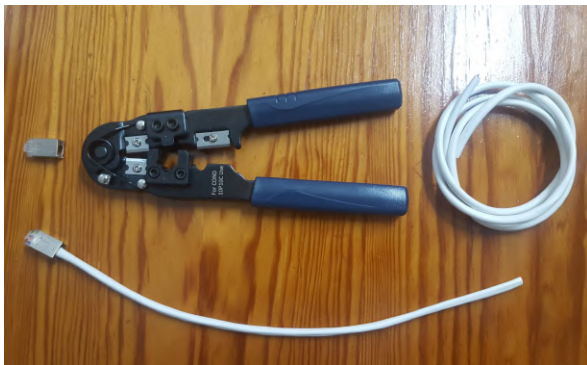
(a) Assembly of a generic *RJ50* gate using a crimping plier.
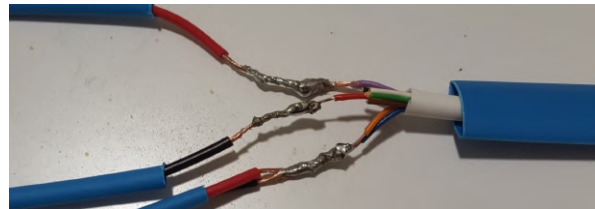
(b) Welding of strain gauge wires.
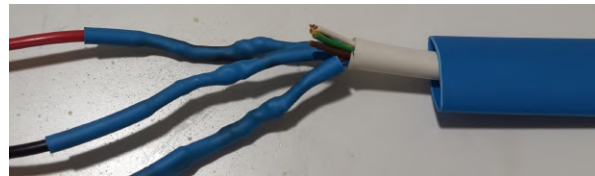
(c) Coating of each individual weld.

Figure 5.11: Coupling between the strain gauges and the data acquisition.

5.4.3   Finalisation of the Aerodynamic Force Balance

The final assembly integrated the mechanical and the electrical together and included additional parts such as the pitot tube support.

On the fixed platform, away from the stream, support plastic boxes were placed to store part of the instrumentation. The Arduino and the pressure sensor were placed inside the boxes. The temperature sensor was fixed in an external side of the box to measure the ambient temperature. The boxes also store the strain gauge and sensors cables to give a clean look keeping a practical handling. The attitude sensor is the only instrument with freedom of positioning. Figure 5.12 (a) present the fixed platform with the storage boxes and all the instrumentation set in it, including the DAQ boards and the USB hub.

The pitot tube support was set in the force balance. The pitot tube is set on the top of the plate with a direction parallel to the stream lines. The pitot tube direction can be adjust using the fixation screw. The two hoses which connect the pitot tube to the pressure sensor were taped on the side of the plate that does not have direct contact with the flow, to decrease drag and turbulence. Figure 5.12(b) depict

the assembly of the pitot tube on the plate and the hoses placement.
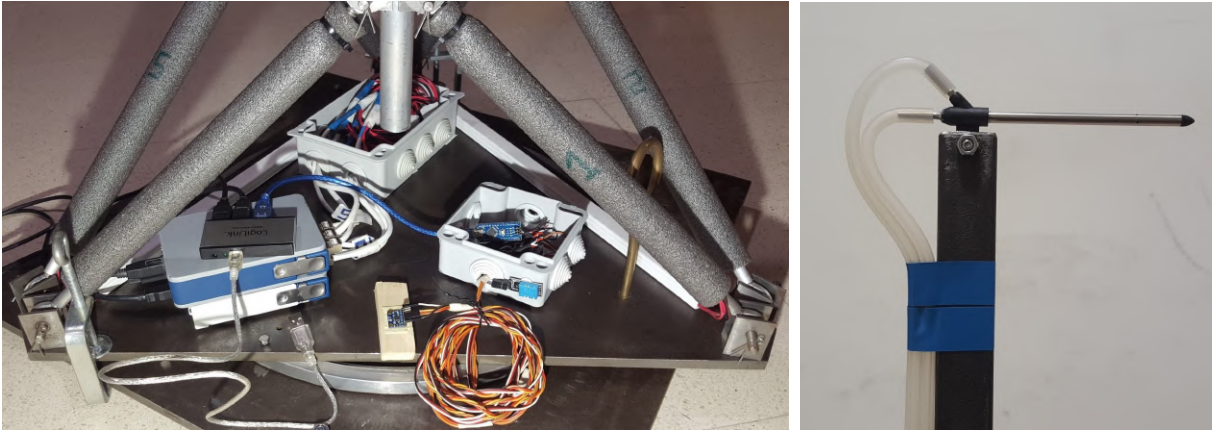
(a) Storage of instruments and cables.

(b) Pitot tube fixation and hoses placement.

Figure 5.12: Final assembly.

The aerodynamic force balance was then completely assembled and ready for experiments. Figure 5.13 shows the aerodynamic force balance in its final form.

Figure 5.13: Aerodynamic force balance.

Chapter 6

Calibration

At this point, the aerodynamic force balance is capable of providing the strain from the sensing bars and compute the corresponding forces through the characteristic fitting curves of each sensing bar strain gauge system. However, the six desired aerodynamics quantities (drag, lift and side forces; roll, pitch and yaw moments) cannot be computed due to the lack of relations between these quantities and the sensing bars strain gauges outputs. The calibration solves this final stage by creating a correlation between these two quantities.

6.1 Calibration Methodology

From start, a mathematical model of calibration is required to relate the aerodynamic components with the strain gauges outputs. The aerodynamic components are represented by f_i, being f_1 drag, f_2 lift, f_3 side, f_4 roll, f_5 pitch and f_6 yaw. The input variable of the model will be presented as r_j, with $j = 1, ..., 6$, and corresponding to the sensing bar force converted from voltage output of the strain gauge bridge.

The aerodynamic forces are dependent of the sensing bar forces and also of the calibration coefficients. The number of coefficients and the complexity of the model depend of the order of the model. The first and second-order models can be described as [29] [30]

$$f_i = \overbrace{\underbrace{\sum_{j=1}^{6} r_j a_{i,j}}_{1° Order} + \sum_{j=1}^{6}\sum_{k=j}^{6} r_j r_k b_{i,j,k}}^{2° Order} + \epsilon_i \tag{6.1}$$

where $a_{i,j}$ and $b_{i,j,k}$ are constant coefficients, and the ϵ_i is a random variable, common regarded as a measurement error.

Expanding and simplifying Equation (6.1) for a generic aerodynamic force component yields [31]

$$f_i = r_1 c_{i,1} + r_2 c_{i,2} + r_3 c_{i,3} + r_4 c_{i,4} + r_5 c_{i,5} + r_6 c_{i,6} + r_1^2 c_{i,7} + r_1 r_2 c_{i,8} + r_1 r_3 c_{i,9} + r_1 r_4 c_{i,10}$$
$$+ r_1 r_5 c_{i,11} + r_1 r_6 c_{i,12} + r_2^2 c_{i,13} + r_2 r_3 c_{i,14} + r_2 r_4 c_{i,15} + r_2 r_5 c_{i,16} + r_2 r_6 c_{i,17} + r_3^2 c_{i,18} \tag{6.2}$$
$$+ r_3 r_4 c_{i,19} + r_3 r_5 c_{i,20} + r_3 r_6 c_{i,21} + r_4^2 c_{i,22} + r_4 r_5 c_{i,23} + r_4 r_6 c_{i,24} + r_5^2 c_{i,25} + r_5 r_6 c_{i,26} + r_6^2 c_{i,27}$$

where $c_{i,1}...c_{i,27}$ are the calibration coefficients for an specific aerodynamic component.

The calibration model to describe the six aerodynamic components with the twenty seven inputs and consider second order can be describe in matrix form as

$$F = CR \Leftrightarrow \begin{bmatrix} f_1 \\ f_2 \\ f_3 \\ f_4 \\ f_5 \\ f_6 \end{bmatrix}_{6\times1} = \begin{bmatrix} a_1 & a_2 & \dots & \dots & a_{27} \\ b_1 & b_2 & \dots & \dots & b_{27} \\ \vdots & \vdots & \ddots & \ddots & \vdots \\ \vdots & \vdots & \ddots & \ddots & \vdots \\ \vdots & \vdots & \ddots & \ddots & \vdots \\ f_1 & f_2 & \dots & \dots & f_{27} \end{bmatrix}_{6\times27} \begin{bmatrix} r_1 \\ \vdots \\ r_1{}^2 \\ r_1 r_2 \\ \vdots \\ r_6{}^2 \end{bmatrix}_{27\times1} \tag{6.3}$$

The procedure consists of applying several well-know load sets and collect the response of the strain gauges facing each load set. The obtained calibration matrix depends on the simulation cases applied to obtain the relations between inputs and outputs, since, Equation (6.2) is an approximation and does not describe exactly the dependence of quantities.

However, the calibration set of all the possible combinations between aerodynamics components in the desired work range of the force balance is an unrealistic approach. Consequently, some methods of regression analysis are applied for a better data fitting of the simulations cases and thus minimise the required number of experiments to obtain a reasonable solution.

The Least Squares method is suggested for aerodynamic force balances using strain gauges in wind tunnel applications[29]. This method is useful to generate all the coefficients without follow a strict load sequence and combine all the possibilities, giving some freedom to select the load sets.

It is important to refer that our calibration procedure is made for a side-slip angle of $0°$, thus called an alpha calibration [32]. The results will limit the subsequent experimental tests to a side-slip of $0°$.

6.2 Ordinary and Weighted Least Squares Method Formulation

The least squares method provides a mathematical procedure that creates a model which fits better the experimental data. Lets use N sets of aerodynamics components, each set has a response of the 27 arrangements of the six r_j. The quantities are now represented as $f_{i,p}$ and $r_{p,m}$, where $p = 1, ..., N$ and $m = 1, ..., 27$.

The least squares searchs the coefficients by minimise the sum of squared errors. Taking Equation (6.2), the least squares function is [30]

$$S_i = \sum_{p=1}^{N} \epsilon_i{}^2 = \sum_{p=1}^{N} \left(f_{i,p} - \sum_{m=1}^{27} r_{p,m} c_{i,m} \right)^2 \tag{6.4}$$

To minimise the function S, the partial derivation is required with respect to each of the coefficients, and these partial derivatives must be zero $\frac{\partial S_i}{\partial c_{i,m}} = 0$. This procedure results in 27 equations and 27

unknowns for each f_i component,

$$-2\sum_{p=1}^{N}\left(f_{i,p} - \sum_{m=1}^{27} r_{p,m}c_{i,m}\right)r_{p,1} = 0$$

$$\ldots \tag{6.5}$$

$$-2\sum_{p=1}^{N}\left(f_{i,p} - \sum_{m=1}^{27} r_{p,m}c_{i,m}\right)r_{p,27} = 0$$

The matrix notation is more convenient to deal with multiple regression models. The model is describe in matrix notation as

$$f = Rc + \epsilon \Leftrightarrow \begin{bmatrix} f_1 \\ f_2 \\ \vdots \\ \vdots \\ f_N \end{bmatrix}_{N\times 1} = \begin{bmatrix} r_{1,1} & r_{1,2} & \ldots & \ldots & r_{1,27} \\ r_{2,1} & r_{2,2} & \ldots & \ldots & r_{2,27} \\ \vdots & \vdots & \ddots & \ddots & \vdots \\ \vdots & \vdots & \ddots & \ddots & \vdots \\ r_{N,1} & r_{N,2} & \ldots & \ldots & r_{N,27} \end{bmatrix}_{N\times 27} \begin{bmatrix} c_1 \\ c_2 \\ \vdots \\ \vdots \\ c_{27} \end{bmatrix}_{27\times 1} + \begin{bmatrix} \epsilon_1 \\ \epsilon_2 \\ \vdots \\ \vdots \\ \epsilon_N \end{bmatrix}_{N\times 1} \tag{6.6}$$

where the vector f corresponds to the observations, the matrix R has the sensing bar force in its rows for each calibration loading, the vector c is the regression coefficients, and ϵ represents the random errors.

To find the least squares estimator, the previous approach is repeated for the matrix form [30]

$$S_i = \sum_{p=1}^{N}\epsilon_i^2 = \epsilon^T\epsilon = (f - Rc)^T - (f - Rc)$$

$$= f^Tf - c^TR^Tf - f^TRc + c^TR^TRc = f^Tf - 2c^TR^Tf + c^TR^TRc \tag{6.7}$$

Applying the least-squares criteria that minimises S holds

$$\left.\frac{\partial S}{\partial c}\right|_{\hat{c}} = -2R^Tf + 2R^TRc = 0 \tag{6.8}$$

Simplifying and reorganise, the least-squares estimator of C is then

$$C = (R^TR)^{-1}R^Tf \tag{6.9}$$

Equation (6.9) is the solution of the least-squares normal equations [30], which completes the system presented in Equation (6.3) and defines the calibration model.

Although the generalised least square is a good data approximation method, the weighted least squares method adds some advantages [33]. The generalised method assume the weighting factors for all the data points are one, an assumption not very appropriate for this type of calibration.

The weighted least squares method considers an individual weighting factor for each data point. This weight can be computed by different approaches and introduces a more accurate experimental analysis. A simple linear regression, such as Equation (6.4), in weighted least-square function is

$$S_i = \sum_{p=1}^{N} w_p \left(f_{i,p} - \sum_{m=1}^{27} r_{p,m}c_{i,m}\right)^2 \tag{6.10}$$

The same approach can be replicated for this new interpretation of data. The created matrix W is a $N \times N$ diagonal matrix with diagonal elements of $w_1, w_2, ..., w_N$ [30].

The solution of the weighted least-squares normal equations results in the weighted least-squares estimator

$$C = (R^TWR)^{-1}R^TWf \tag{6.11}$$

6.2.1 Weighted Scheme

The formulation of the weighted matrix has many approaches concerning the references. The matrix W is an improvement of values precision but its computation methodology will set the complexity of the problem. As any estimation analysis, the weighting factors are always parameters with uncertainty but the lower this uncertainty is, the more trustful the results are.

The simplest approach for the W matrix is assume the identity matrix (I), which leads to the ordinary least squares approach. Most of the times, this approach is the initial step to get a general idea of the scatter of data. After that, variation models could estimate new weighting factor for the model. For instance, using the standard deviation to stipulate a new W matrix for subsequent interpolations [33].

The weighting matrix approach described in [32] is a current and extensive process to minimise the uncertainty of the applied loads and random errors in the measurement procedure. The construction of the weighted matrix considers two contributions to the uncertainties of the applied loads: the contributions of the sources of errors due to the application of weights in the calibration system V_W and the uncertainties in the readings of the bridges V_R, expressed as

$$W = (V_W + DV_R D^T)^{-1} \tag{6.12}$$

Matrix V_W

The matrix V_W is diagonal with dimensions of $N \times N$. Its elements are based on the uncertainties of the weights used in the loading sequence and an estimation of the uncertainties caused by the calibration system. This approach leads to the testing of the weights employed to verify its uncertainties. The second contribution is based on the quantification of the sources of error that affect the resolution of the calibration system, such as frictional forces and misalignment between cables and pulleys. To identify the second contributions, an additional experimental calibration with great precision is required to characterise the supplementary structures used in the main calibration. This extra experimental test makes the calibration more extensive and dependent of many tools and instruments.

The replacement method considers the standard deviation of the fit σ_i, expressed as

$$\sigma_i^2 = \frac{1}{N - m} \sum_{p=1}^{N} (f_{i,p} - \hat{f}_{i,p})^2 \tag{6.13}$$

where m is the number of parameters to be fitted (number of coefficients in Equation (6.2)). The standard deviation is initially computed by considering the identity matrix as W to obtain the first iteration. The matrix V_W is build up by adding the standard deviations corresponding to each aerodynamic component to the main diagonal, taking into account the number of loads for each component.

Matrix V_R

The uncertainty of the reading values can be mitigated by repeating the same calibration several times to build V_R that is diagonal symmetric. Several calibrations under repeatability conditions should be carried out over a short period of time. The diagonal elements of V_R are represented by the variances and the off-diagonal elements are the covariances between the readings of the six strain bridges. It

has dimensions $6N \times 6N$, where N lines are grouped corresponding to each force transducer. The formulation of matrix V_R is presented in Appendix E, Equation (E.1).

This matrix is calculated from the matrix R_{global}, of size $6N \times z$, where N is the number of sets and z the number of repetitions of the sets. The first N elements of column 1 correspond to the readings of the load cell r_1 from the first calibration loading condition, followed by the N elements of the readings of the load cell r_2 and so on. The same procedure is repeated for the remaining columns, using the data set from the other calibrations. In the present work, the calibration was repeated three times, thus $z = 3$. The matrix V_R is obtain by transpose and apply function "cov" in Matlab®.

Matrix D

The elements of matrix D ($N \times 6N$) correspond to the sensitivity coefficients, evaluated by taking the partial derivatives of Equation (6.2). For the aerodynamic force, f_1, the formulation of matrix D is presented in Appendix E, Equation (E.2).

In this computation, only the sensitivity coefficients whose second subscripts match, i.e. correspond to the same loading, have values different from zero. The matrix D is reduced to several block submatrices, being each block diagonal not null. Each element of the diagonal corresponds to the coefficients of the corresponding aerodynamic force component,

$$\frac{\partial f_{p,1}}{\partial R_{p,1}} = c_{1,1} \qquad \frac{\partial f_{p,1}}{\partial R_{p,2}} = c_{2,1} \qquad ... \qquad \frac{\partial f_{p,1}}{\partial R_{p,6}} = c_{6,1} \qquad (6.14)$$

Therefore, $DV_R D^T$ can only be obtained after the first iteration in the calibration procedure, where it is assumed that W equals to V_W^{-1}.

6.2.2 Goodness of Fit

The least squares method settles the hypothesis that by minimising the sum of squared errors (ssE), the optimum fitting of the data is obtained. The errors, in turn, can be described as the deviation of the data observations (f_i) and the estimated values from the fitting function ($\hat{f}_i$) [34]. Therefore, the sum of squares errors is equal to

$$ssE = \sum_{p=1}^{N} (\hat{\epsilon}_{i,p})^2 = \sum_{p=1}^{N} (f_{i,p} - \hat{f}_{i,p})^2 \qquad (6.15)$$

A good measurement of goodness of fit is the chi-square, χ^2, which provide a ratio between the computed difference and the variance σ^2 [33]. The χ^2 is described as [33][34]

$$\chi^2 = \frac{ssE}{\sigma^2} = \sum_{p=1}^{N} \left\{ \frac{1}{\sigma_i^2} (f_{i,p} - \hat{f}_{i,p})^2 \right\} \qquad (6.16)$$

This equation can be written in matrix form as

$$\chi^2 = (F - \hat{F})^T W (F - \hat{F}) \qquad (6.17)$$

The relation between quantities can be applied for the number of degrees of freedom for fitting the data point, $v = N - m$. This leads to the reduced chi-square,

$$\chi_v^2 = \frac{\chi^2}{v} = \frac{(F - \hat{F})^T W (F - \hat{F})}{N - m} \qquad (6.18)$$

The fitting function is a good approximation to the parent function if χ_v^2 is approximately unitary. That means the estimated variance of the fit should agree with the parent variance. Values of χ_v^2 greater than one translate large deviations and consequently large estimated variance, so the selected fitting function is not appropriate for describing the data. On the other hand, values of χ_v^2 less than one do not surely indicate a better fit, however indicate the existence of uncertainty in the estimation and the χ_v^2 will vary from experiment to experiment [33].

6.3 Calibration Procedure

The data provided from the strain gauges is converted to force by using the sensing bar formulas presented in Chapter 4. These values are used to compute the matrix R, where the second order terms are obtained by combination of the linear terms for each load state throughout the load set.

As mentioned, the first iteration requires the use of the identity matrix as W to make the estimation of the standard deviation possible, Equation (6.13). The matrix V_W can be used in further computations. The standard deviation requires the first estimation of the load set ($\hat{F}$).

The second iteration uses only the matrix V_W to obtain the matrix W. The separation of the weighted scheme, Equation (6.12), is useful to quantify the improvement of the fit. The next step is to compute the two last two matrices V_R and D, using Equations (E.1) and (E.2).

The third iteration uses the complete form of matrix W, Equation (6.9). The coefficients are obtained through the weighted least squares formulation, Equation (6.11). The Equations (6.17) and (6.18) are used to evaluate the goodness of fit.

Figure 6.1 schematises the calibration procedure described previously.
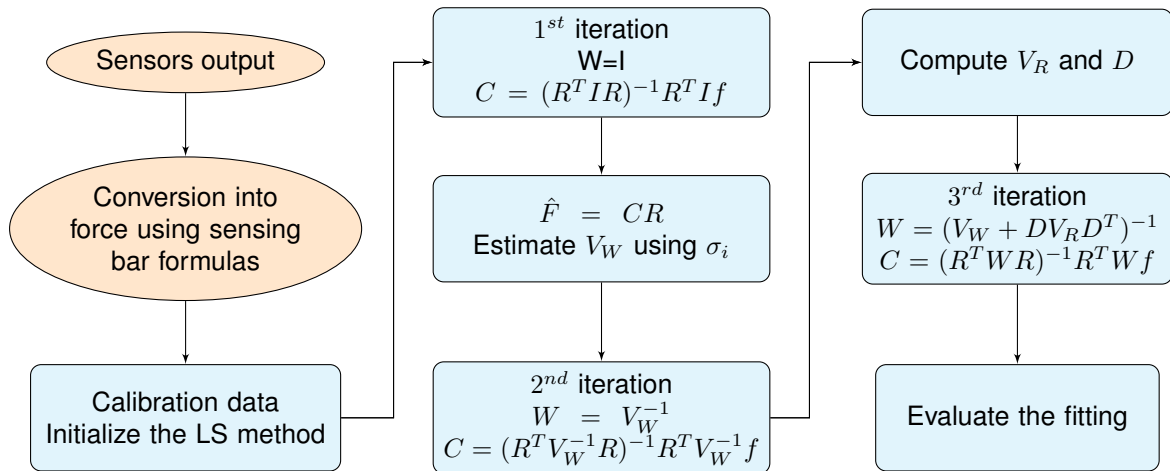
Figure 6.1: Calibration procedure flowchart.

6.4 Calibration Apparatus and Setup

The calibration is performed by applying a sequential weight load in the axes directions, Figure 3.2. In the Z direction the weights can be applied directly on top of the force balance. The X and Y directions

require the use of a pulley to transfer the vertical load into a horizontal load. The height of the pulleys must match the height of the force balance so that the cable which connects the alpha adjustment and the pulley are completely horizontal. The rotation axis must also be perpendicular to the defined axis, and the cable placed in order of ensure the same direction as the coordinate axis. Figure 6.2 (a) shows the apparatus used in the calibration tests to provide a F_X load.

(a) Configuration of pulley to create a F_X load.

(b) Additional arm used to create moment.
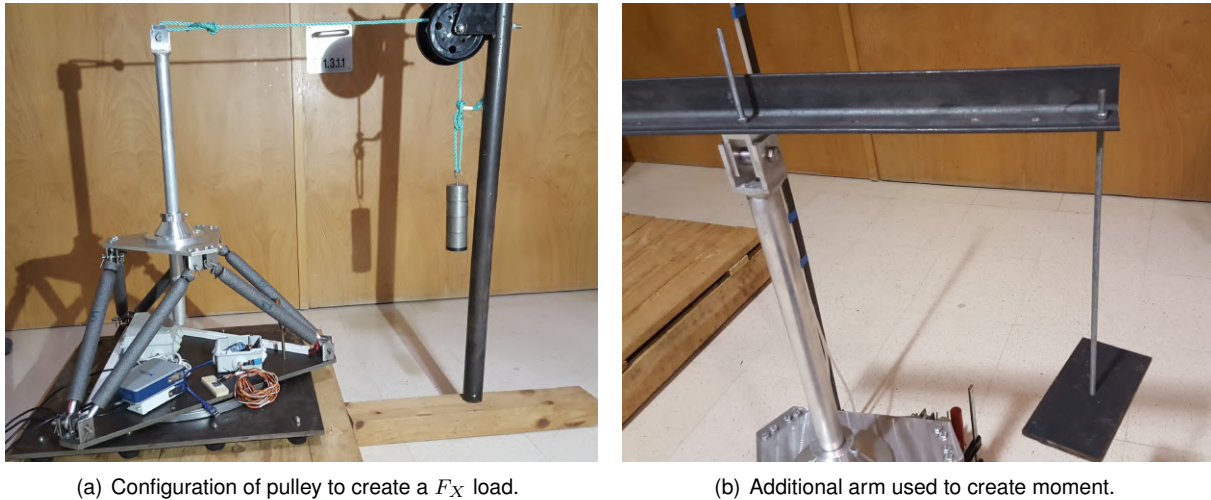
Figure 6.2: Apparatus to apply loads.

Pure moments can not be applied to the force balance calibration procedure due to lack of specialised tools for the task and the inability of creating symmetrical forces to obtain a pure moment as result. This last approach requires more complex system of pulleys and twice as much weights, neither of them are available. As result, pure moments are not applied in the loading cases. Instead, a composed load of one force and one moment is applied, where the moment is the result of applying the force to a selected length of the additional arm created for this effect, see Figure 6.2 (b).

The data provided by the bridges is processed by two *National Instruments*™ *NI 9237* boards, each one reads three strain bridges. As mentioned and used before, *LabVIEW*™ is the software adopted to treat the data. For this stage of development, an initial version of user interface was created to couple both *NI 9237* boards and synchronise them, in order to be able of read, display and save the data of the six bridges at the same time. This early user interface also process the strain output of each bridge using the respectively sensing bar strain gauge system calibration formula, the final quantity provided is the sensing bar force. The values are read at a sample rate of 1000Hz , the data is averaged in loops of 100 samples.

The collected data is processed following the method described in the previous section to obtain the calibration coefficients.

The calibration was composed by 87 loading combinations, divided in 11 loads for each axial force and 18 loads for each composed load. The loading sequence was applied 3 times under the same conditions. A pair of weights of approximately 10N, 17N, 44N, 50N and 100N was incremented sequentially using an adequate support for the loads. In composed loads, the pair of 100N was not used, and the length of the additional arm is 0.3m. All the weights and the support were accurately weighted in a pre-

cision scale with a resolution of 0.01g and accuracy of ±0.05g. The full set of the loading combinations is presented in Appendix E, Table E.1.

6.5 Calibration Results

Concluded the third iteration of calibration procedure, the calibration coefficients for the aerodynamic force balance were obtained, some of them are shown in Table 6.1. The complete coefficients matrix is presented in Appendix E, Equation (E.3).

Table 6.1: Calibration coefficients.

coefficient	F_X	F_Y	F_Z	M_X	M_Y	M_Z
$c_{i,1}$	-0,617896	0,090931	-1,238098	-0,088204	-0,229695	0,167224
$c_{i,2}$	-0,133195	0,043550	-1,538156	0,064625	-0,032167	0,049581
$\vdots$	$\vdots$	$\vdots$	$\vdots$	$\vdots$	$\vdots$	$\vdots$
$\vdots$	$\vdots$	$\vdots$	$\vdots$	$\vdots$	$\vdots$	$\vdots$
$c_{i,26}$	-0,006707	0,008181	0,008594	-0,002857	-0,002686	-0,003020
$c_{i,27}$	-0,000170	0,000569	0,004413	-0,000300	-0,000166	-0,001171

With the coefficients matrix, the fitting forces ($\hat{F}$) for the calibration loads conditions were obtained using Equation (6.3). These values are presented in Appendix E, Table E.2..

The evaluation of fitting using the χ^2 and χ_v^2 were computed with the values of $\hat{F}$ and Equations (6.17) and (6.18). The values are shown in Table 6.2.

Table 6.2: Goodness of fit χ^2 and χ_v^2.

Load cell	χ^2	χ_V^2
F_1	386.69	6.445
F_2	244.40	4.073
F_3	498.49	8.308
F_4	30.29	0.505
F_5	73.09	1.218
F_6	39.90	0.665

Some values of χ_v^2, which are not close to unit, suggest the experimental calibration procedure should be investigated. The reduced chi square of the estimated bar forces greater than expected can be a consequence of the quantification of the uncertainties. The lower number of loads, the high forces applied and the non-symmetry of the loading, compared with the other three load sets, can be the reason of the deviation. More composed loads, mixing two and three axial forces, could improve the data scatter, but this experimental tests are not easy to proceed in the available facilities.

Chapter 7

Testing

7.1 Experimental Procedure

The aerodynamic force balance will operate in the Técnico Aerospace Engineering Laboratory wind tunnel. The closed wind tunnel airspeed can be regulated by $v_w = 1.49f_w - 0.25$, where v_w stands for wind tunnel airspeed in (m/s) and f_w inverter frequency in (Hz).

This equation comes up from the linear regression made for the points of the experimental test carried out to calibrate the wind tunnel air stream speed and the inverter frequency that drives the fan motor, presented in Chapter 3. The R^2 of 0.9998 shows the evolution of airspeed is almost linearly proportional to the inverter frequency.

7.1.1 Experimental Apparatus

The force balance should be placed in the test section of the wind tunnel. Due to the wind tunnel being closed circuit, the flow is almost uniform in the entire test section. The proximity of the force balance and the nozzle can be adjusted for the needs of the test model. However, it is recommended to place the balance close to the wind tunnel nozzle to ensure the uniform flow conditions and a better alignment of the force balance X axis with the nozzle symmetry axis.

The centering of the force balance will influence the interaction of the turbulence mixing layer created by the flow separation on the nozzle wall and the model. The height of the force balance position can be regulated by adding spacers to ensure the flange is under the lower limit of the nozzle, ensuring that instrumentation and rough structures do not interact with the flow. This type of adjustment is made in order not to change the strut size, since changes of the strut height require new considerations on the moments values due to the calibration being made for the 445mm strut.

The 5m USB cable allows the connection between the USB hub and the computer placed outside the wind tunnel. This way, the test chamber is free of bodies that are not required for the testing.

Figure 7.1 shows the experimental apparatus with the force balance set in the wind tunnel.
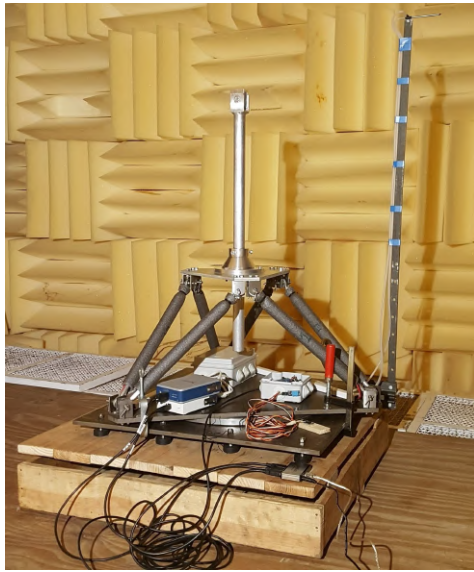
(a) Aerodynamic force balance set in wind tunnel test section.
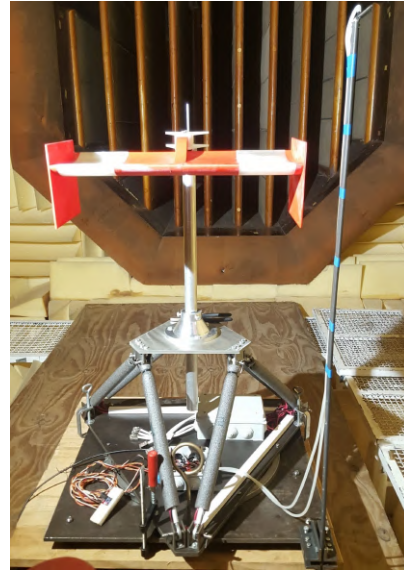
(b) Test model mounted on the force balance.

Figure 7.1: Experimental apparatus.

7.1.2 Procedure Guide

The following steps are required to initialise and operate the aerodynamic force balance:

1. Set the aerodynamic force balance inside the wind tunnel test near to the nozzle and over a additional structure to place the top of the flange exactly under the lower limit of nozzle;

2. Align the force balance with the nozzle so that the X axis of the force balance is parallel to the axis of symmetry of the nozzle. Then level the moving platform by adjusting the rubber supports at the bottom of the force balance, use a spirit level or similar on all edges;

3. Level the top of alpha adjustment with a spirit level or similar. Then, run the attitude sensor calibration script with the sensor on the current position of the top surface and aligned with the lateral surface edge. This reset the values of roll, pitch and yaw to zero;

4. Set the desired angle of attack using the pitch value of the attitude sensor as reference. The angle of side-slip follows the same methodology, but taking the yaw. The rotating collar is fix by three clamps in each vertex of the fix platform;

5. Mount the test model on the force balance and verify the nozzle limits influence on the model;

6. If the attitude of the model during the experiment is a parameter of study, the sensor should be placed in a part of the model that does not influence its aerodynamics (within the model if possible). Then reset the attitude sensor values for the current position running the calibration script again;

7. Place the pitot tube support in the front of the force balance and adjust the height to ensure the flow interference between plate and model do not occur. Then align the pitot tube with the flow;

8. Connect the sensing bars cable in the DAQ boards. Three sensing bars per DAQ board and follow the numeration of the cable $(1, 2, 3, 4, 5, 6)$ with the numeration of the two DAQ boards (ch0, ch1, ch2, ch0, ch1, ch2);

9. Connect the three USBs to the hub, power the hub and connect it to the computer outside;

10. Open the *LabVIEW*^{TM} file and verify that the first psychical channel corresponds to the DAQ board with the sensing bar #1, #2, #3 and the second physical channel to the other and check the order of the channels in each physical channel;

11. The force balance is ready for the experiments. Run both acquisition files in simultaneous and start with 0 airspeed. Change the frequency to the desired velocity. Take some time between velocities to identify the corresponding quantities and average them in data treatment;

12. Remove the test model and repeat the exact sequence to take the contribution of the structure under the influence of the flow to the forces and moments.

7.2   FST Rear Wing Demonstration

An experimental test was proceeded in order to analyse the complete apparatus. The test consists of performing part of the experimental analyses required for the master's thesis by Tiago Rocha [35], a colleague student of aerospace engineering.

The experimental test consists of an aerodynamic analyses on the rear wing of a racing car designed by the formula student team of Instituto Superior Técnico (FST). A small scale model of the rear wing was manufactures to execute the experimental test reference, see Figure 7.2 (a). This wing model integrates a support arm made specifically to be mounted on a force balance.

(a) Scale model of the FST rear wing.

(b) Flat endplates profile (Top view).

(c) Curved endplates profile (Top view).
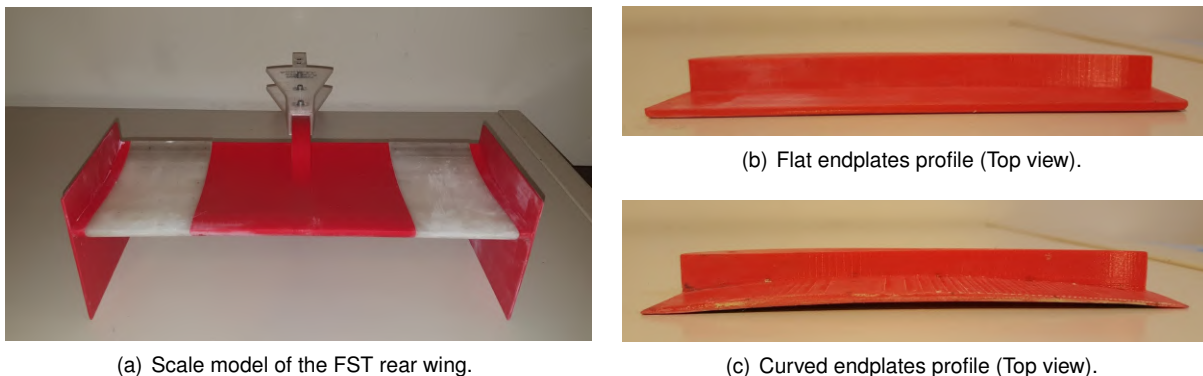
Figure 7.2: Experimental model for analysis.

The experimental analysis pretends to compare the influence in drag and downforce of the rear wing endplates. To this end, Rocha [35] created both flat endplates, see Figure 7.2 (b), that are a scale reproduction of the endplates used on the last racing car developed by FST, and also a second set of endplates with a profile that adopts a curved geometry following the *NACA 2402* airfoil properties, see Figure 7.2 (c), which is a most worthwhile airfoil from a CFD analysis with several airfoils.

The wind tunnel tests consider three different rear wing configurations, without endplates, flat and curve endplates and the quantities of study are the forces F_X and the F_Z and the moment M_Y, corresponding to drag, downforce and pitch moment, respectively, at an average velocity of the racing car in circuit, around 15m/s. This velocity must be converted to conserve the aerodynamic influence by means of Reynolds number, because the testing model has different dimensions than the racing car. The resulting equivalent velocity for the rear wing model is around 37m/s. Three additional velocities

were introduced in the experiment to gather more data about the response of the rear wing with the change in airspeed and the response of the force balance. Figure 7.3 presents the collected data from the experimental analysis provided by the aerodynamic force balance.

(a) Response in F_X.

(b) Response in F_Z.

(c) Response in M_Y.
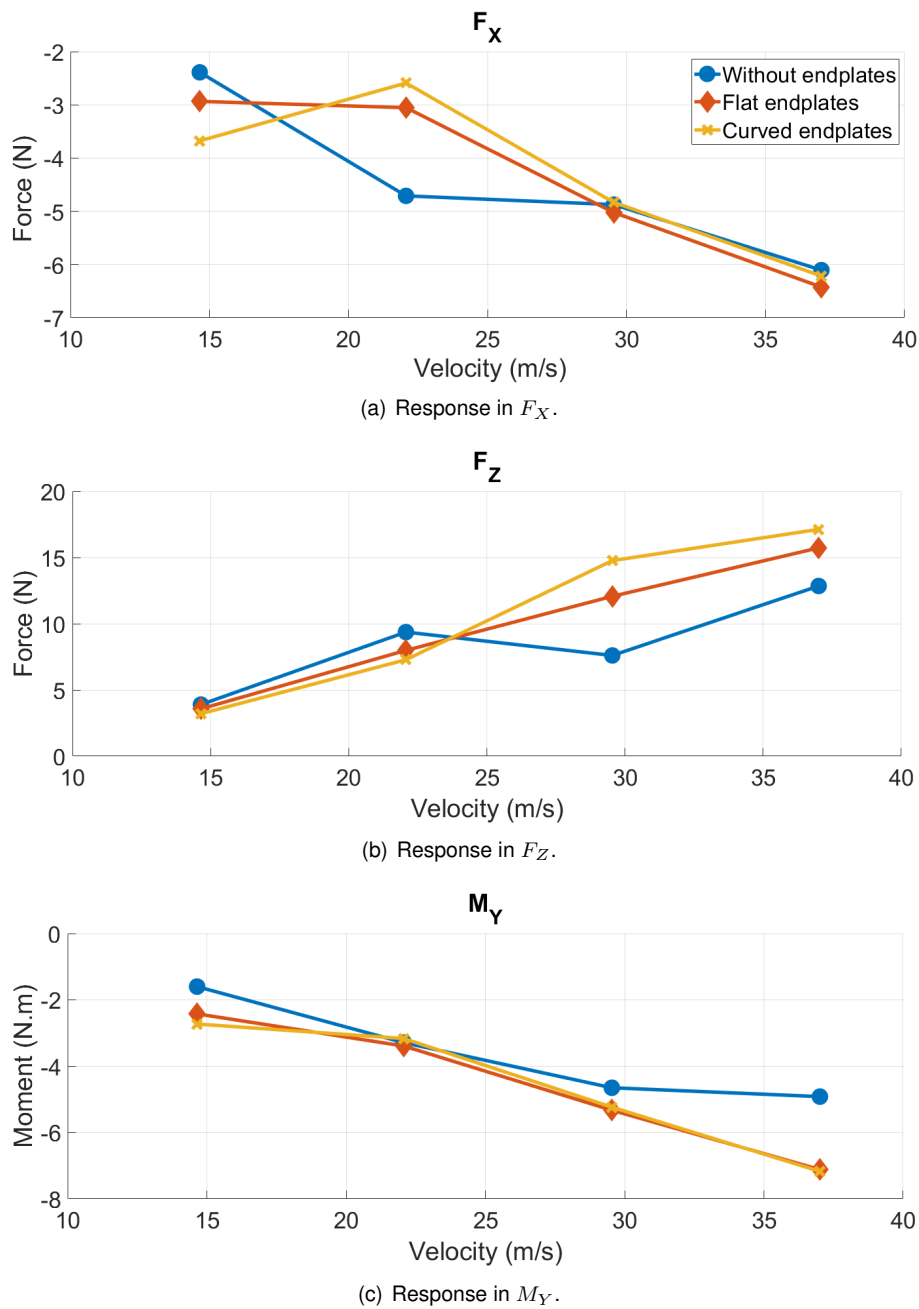
Figure 7.3: Results of experimental test with the three configurations.

The values can be converted to the dimensionless coefficients for rear wing using Equations (3.1) and considering 0.16m of chord (c), 0.4m of span (b) and 0.27m of support arm. The support arm length is used to remove the contribution of F_Z for the moment, only the contribution of the wing geometry is required. It was assumed that the center of pressure is located at $1/3$ of the chord. The Reynolds number is computed through Equation (2.1) and using the conditions of that day, air density (ρ) of 1.184kg/m^3 and dynamic viscosity (μ) of 1.841E-05kg/(m.s).

Figure 7.4 shows the C_D, C_L and C_m with characterise the three rear wing model configurations, the

C_D and C_L obtained from the CFD analyses for the three configurations [35] are also shwon.
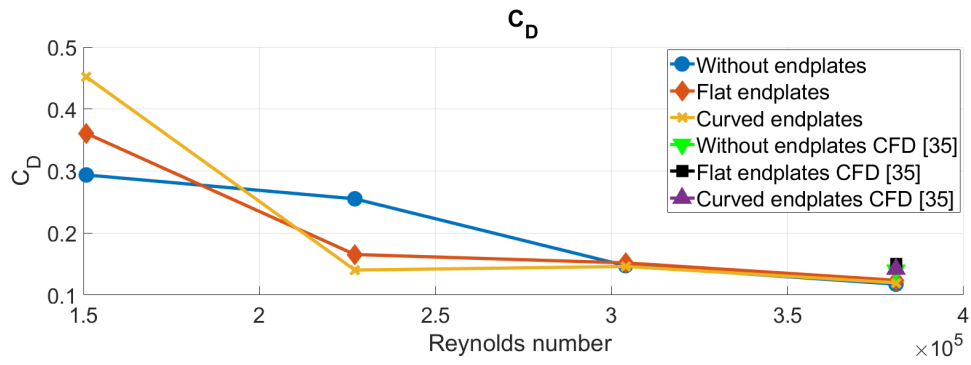
(a) Drag coefficient.
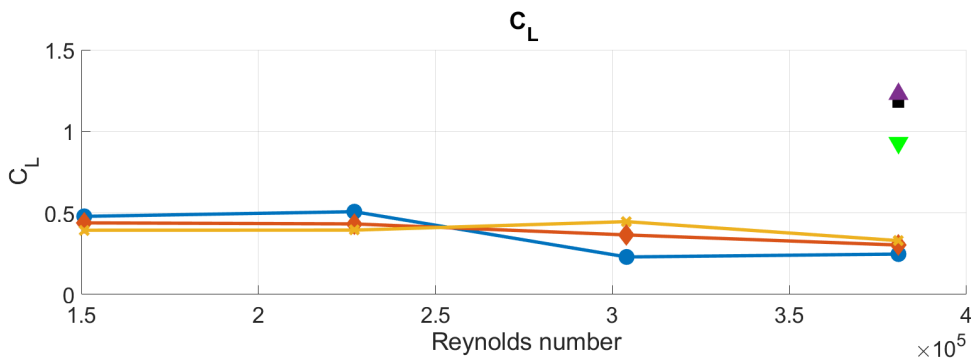
(b) Lift coefficient.
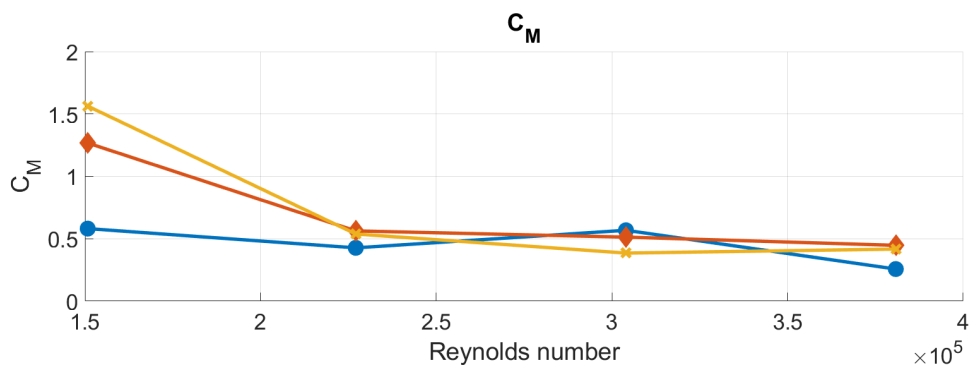
(c) Moment coefficient.

Figure 7.4: Dimensionless coefficients in relation of the Reynolds number for the three configurations.

Unfortunately, the last step of the procedure guide was not followed due to the time available to use the wind tunnel facilities. Therefore, the drag values and the drag coefficients cannot be interpreted in magnitude because the influence of the force balance structure is interrelated in values. However, the tendency of the values can be analysed, as well as the quantities with the same velocity or Reynolds number, the influence of structure is the same if the same conditions are applied.

The drag coefficient tendency for the required speed (37m/s) is in agreement with the CFD analysis. The direct reduction of drag was not the main goal in the endplate analyses, in fact, the almost equal drag obtained for the flat and curved endplates is in coherency with the CFD.

From a basic point of view, the introduction of more surfaces will create more drag, however the use of endplates is made to reduce the wingtip vortices and, this way, reduce the induced drag. The

reduction of induced drag will create an increment in lift or downforce, depending on the intention [36]. The proof of this effect is validated both with the results obtained experimentally and computationally.

The main goal, the improvement of lift using curved endplates instead of flat endplates is achieved. An increment of 4.15% of lift was obtained from the CFD, the experimental test complement with an improvement of 9%. Normally, a different between computational and experimental is expected, therefore the use of both techniques refine the analysis and improve the results.

From the results obtained for C_L and C_D throughout the variation of velocity, it is observed that the Reynolds number has a strong influence in the performance of the endplates. Further studies should be performed to detail the influence of the velocity on the different rear wings and analyse the range of velocities where the racing car perform to match results.

From the CFD and the experimental analysis, the results introduce a strong validation of the C_L/C_D improvement using endplates following a *NACA 2402* airfoil instead of simple flat endplates, at a speed of 37m/s. The results obtained from the two methodologies follow the same tendency and the relation between different configurations are similar. However, the quantities obtained were different in terms of magnitude.

This observation requires more tests with the force balance and analysis with CFD. As mentioned in Chapter 1, the CFD is not an unquestionable tool with unequivocal results. Furthermore, the flow conditions and properties during the experimental test were not replicated in the CFD analyses. However, the substantial disparity highlights the need of a more comprehensive calibration.

The use of simple loadings in the calibration can be in the origin of the variation of the values in magnitude. Since in this case of study, three active components (F_X, F_D and C_Y) form a compose loading not considered in the calibration.

To validate the previous conclusions, a simple static test was conducted to analyse the response of the force balance. This test consists in lay three weight increments of 5N over the top part of the balance, exact same procedure as the one used in static calibration of component F_Z. The response of F_Z for this test load is presented in Figure 7.5.
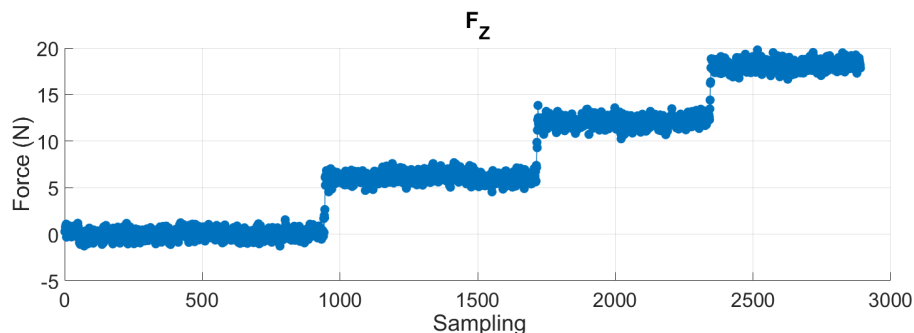
Figure 7.5: F_Z response to a static load test to validate the aerodynamic force balance.

The force response in increments after the average of the values are: 6.11N, 5.98N and 6.08N.

This test demonstrates the good response of the aerodynamic force balance when simple axial loads are applied and exhibits the good accuracy of the force balance.

Chapter 8

Conclusions

The main goal of this thesis was to endow Aerospace Engineering facilities with an aerodynamic force balance capable of measuring six components. Intermediate analyses and assumptions from the most varied fields were carried out to suit the aerodynamic force balance to the desired specifications and all the tasks were overcome to achieve a reasonable product. This result can be seen on the good values obtained throughout the present document and summarised in an operational aerodynamic force balance with a convenient total cost and considerably below the cost of a similar product if it was purchased.

The adaptation of the design to fulfil the requirements required a finite elements analysis which produced the accurate values to support redimensioning of components. Furthermore, the experimental tests performed in the design phase validated the subsequent implementation labours and proved to be a good practice in works with a more practical component.

The implementation of the strain gauges was made following the specifications and taking additional care. Despite all that, the strain gauge placement always has some variation from the ideal placement. Adding the fact of the material properties and geometry have a deviations from the considered baseline, due to tolerances associated with machines, among others, characterising a physical system in detail is complex and may be unattainable. Therefore, the characterisation of each assembled strain gauges and sensing bar has became a very favourable approach to dissipate some errors of this nature.

The experimental procedure to calibrate exposed the strong dependence between a good fitting value and a good execution and employment of specific apparatus. The adopted mathematical assumption takes into account the number of inputs and the problem nature, second order is the minimum to achieve positive fitting with reasonable computation effort. The introducing of the sensing bar strain gauge formula in the middle of the process was beneficial to scatter the uncertainties of the fitting coefficients. As a result, the calibration values held a lower uncertainty than the values obtained in calibration procedure reference [32].

The values obtained in the rear wing model experiment support the conclusions drawn from the CFD analysis and, this way, ensure that the new rear wing configuration will optimise the performance of racing race car when implemented in it. The influence of the velocity, and consequently the Reynolds, was

an additional beneficial result from the experimental analysis. Due to the reduced time in the facilities and lack of opportunity to perform further tests, some trials could not be executed, and some steps were excluded. For instance, the values of drag do not take the support drag into account. However, the dependence is linear, therefore, the evolution of drag is correct, despite the value does not correspond only to the influence of the rear wing.

8.1 Achievements

The major achievements of this thesis were:

- Validation of a CAD design with finite elements simulations and experimental test;
- Manufacture of part components and assembly of an aerodynamic force balance;
- Development of software to operate speed, temperature and attitude sensors;
- Experimental tests to characterise a *Wheatstone* bridge placed on a bar;
- Aerodynamic force balance calibration using least squares method through experimental analysis;
- Development of a user interface to control several strain gauges and collect data;
- Validation of mechanical and electrical system integration;
- Demonstration of usage in relevant test case.

8.2 Future Work

Although this thesis fulfils the objectives defined, some considerations will be presented to enhance the performance and functionalities of the aerodynamic force balance.

The major future work that has influenced some of the developments in the current work is the creation of a DAQ from scratch. This implementation will save more than half of the costs presented in Chapter 5. For this reason, the two *NI 9237* boards were the only force balance component that was not purchased. The tests with the *HX711* and the operational amplifier in Chapter 4 was the baseline of the development to conclude that is feasible with extensive analysis in frequency and amplification.

The accuracy of the force balance can be improved with better calibration. (This can be made with the current system and must be made if a new DAQ system is implemented). The calibration should consider more data points and symmetrical loads in each component of force and moment. It is also worthwhile considering pure moments in the calibration. However, the introduction of combined loads is the main reason for reviewing the calibration and will surely improve the fitting coefficients of the force balance. Tests with a third order model should also be pursued.

The strut is the main contributor to the induced drag that affects the results. This contribution can be reduced substantially if an airfoil profile covers the strut. Some symmetrical airfoils in streamline have a C_D around 0.02 compared to 1 for the cylinder.

Finally, the user interface should include the additional instrumentation. In this way, all the data provided by the force balance is presented in a single platform.

Bibliography

[1] D. P. Rayner. *Aircraft design: a conceptual approach*. American Institute of Aeronautics and Astronautics, Inc, 2nd edition, 1992. ISBN:0-930403-51-7.

[2] D. F. Young. Basic principles and concepts of model analysis. In *Experimental Mechanics*, volume 11, pages 325–336. Kluwer Academic Publishers, July 1971.

[3] J. B. Barlow, W. H. Rae, and A. Pope. *Low-Speed Wind Tunnel Testing*. Wiley, 3rd edition, 1999. ISBN: 978-0471557746.

[4] J. Tu, G. H. Yeoh, and C. Liu. *Computational Fluid Dynamics: A Practical Approach*. Butterworth-Heinemann, 3rd edition, 2018. ISBN: 978-0-08-101127-0.

[5] O. D. L. Mejia and J. A. E. Gomez. *Numerical Simulation of the Aerodynamics of High-Lift Configurations*. Springer International Publishing, 1st edition, 2018. ISBN: 978-3-319-62135-7.

[6] R. I. Emori and D. J. Schuring. *Scale Models in Engineering: Fundamentals and Applications*. Pergamon Press, 1st edition, 1977. ISBN:0-08-020860-6.

[7] C. Tropea, A. L. Yarin, and J. F. Foss. *Springer handbook of experimental fluid mechanics*. Springer Science & Business Media, 1st edition, 2007. ISBN:978-3662491621.

[8] M. Raffel, C. E. Willert, F. Scarano, C. J. Kähler, S. T. Wereley, and J. Kompenhans. *Particle Image Velocimetry. A Practical Guide*. Springer International Publishing, 3rd edition, 2018. ISBN:978-3-319-68851-0.

[9] B. F. R. Ewald. Multi-component force balances for conventional and cryogenic wind tunnels. *Measurement Science and Technology*, 11(6):R81, 2000. URL `https://iopscience.iop.org/article/10.1088/0957-0233/11/6/201`.

[10] B. Dasgupta and T. S. Mruthyunjaya. The stewart platform manipulator: a review. *Mechanism and Machine Theory*, 35(1):94–114, 2000. doi: 10.1016/S0094-114X(99)00006-3.

[11] R. Ben-Horin, M. Shoham, and S. Djerassi. Kinematics, dynamics and construction of a planarly actuated parallel robot. *Robotics and Computer-Integrated Manufacturing*, 14(2):163–172, 1998. doi: 10.1016/S0736-5845(97)00035-5.

[12] J. Lee. *Investigation of quality indices of in-parallel platform manipulators and development of Web-based analysis tool*. PhD thesis, University of Florida, 2000.

[13] M. V. Cook. *Flight Dynamics Principles*. Elsevier Ltd, 2st edition, 2007. ISBN: 978-0-7506-6927-6.

[14] B. Etkin and L. D. Reid. *Dynamics of Flight: Stability and Control*. Wiley, 3rd edition, 1995. ISBN: 978-0471034186.

[15] R. C. Nelson. *Flight Stability and Automatic Control*. McGraw-Hill, 2st edition, 1997. ISBN: 978-0070462731.

[16] Centro de ciências e tecnologias aeronáuticas e espaciais: Túnel aero-acústico, Accessed: Oct 2019. Online at: `https://fenix.tecnico.ulisboa.pt/investigacao/cctae/tunel-aero-acustico`.

[17] XFLR5, v6.40, Accessed: Oct 2019. Online at: `http://www.xflr5.tech/xflr5.htm`.

[18] J. T. P. Fernandes. Design of a wind tunnel force balance. Master's thesis, Instituto Superior Técnico, June 2018.

[19] R. G. Budynas and J. K. Nisbett. *Shigley's Mechanical Engineering Design*. McGraw-Hill Education, 10th edition, 2014. ISBN:9780073398204.

[20] C. SolidWorks. Help meshing, Accessed: Nov 2020. Online at: `https://help.solidworks.com/2018/english/SolidWorks/cworks/c_Background_on_Meshing.htm?id=fd537865fa9344d599de7b6e6a9bb063#Pg0`.

[21] *Fastenings*. Thread geometry - metric coarse, Accessed: Jan 2020. Online at: `https://www.trfastenings.com/products/knowledgebase/thread-geometry/metric-coarse-standard`.

[22] HBM. Ly linear strain gauges with 1 measuring grid, Accessed: Oct 2019. Online at: `https://www.hbm.com/en/4561/ly-linear-strain-gauges-with-1-measurement-grid/`.

[23] J. William N. Sharpe. *Springer handbook of experimental solid mechanics*. Springer Science & Business Media, 1st edition, 2008. ISBN:978-0-387-26883-5.

[24] *National Instruments*[TM]. Measuring strain with strain gauges, Accessed: Oct 2019. Online at: `https://www.ni.com/pt-pt/innovations/white-papers/07/measuring-strain-with-strain-gages.html`.

[25] C. M. Jha. *Thermal Sensors. Principles and Applications for Semiconductor Industries*. Springer Science & Business Media, 1st edition, 2015. ISBN:978-1-4939-2580-3.

[26] M. Kok, J. D. Hol, and T. B. Schön. Using inertial sensors for position and orientation estimation. *Foundations and Trends in Signal Processing*, 11(1-2):1–153, 2017. doi: 10.1561/2000000094.

[27] *National Instruments*[TM]. Ni 9237: datasheet, Accessed: Nov 2019. Online at: `http://www.ni.com/pdf/manuals/374186a_02.pdf`.

[28] *National Instruments*™. Getting started guide ni 9237, Accessed: Nov 2019. Online at: `http://www.ni.com/pdf/manuals/374186f.pdf`.

[29] AIAA. *Recommended Practice: Calibration and Use of Internal Strain-Gage Balances with Application to Wind Tunnel Testing*. American Institute of Aeronautics and Astronautics, 1st edition, 2003. DOI: 10.2514/4.476464.001.

[30] D. C. Montgomery, E. A. Peck, and G. G. Vining. *Introduction to Linear Regression Analysis*. John Wiley & Sons, Inc., 5th edition, 2012. ISBN: 978-0-470-54281-1.

[31] M. L. Reis, W. Vieira, I. Barbosa, O. A. Mello, and L. Santos. Validation of an external six-component wind tunnel balance calibration. *24th AIAA Aerodynamic Measurement Technology and Ground Testing Conference*, June 2004. doi: 10.2514/6.2004-2300.

[32] M. Reis, R. Castro, and O. Mello. Calibration uncertainty estimation of a strain-gage external balance. *Measurement*, 46(1):24–33, 2013. doi: 10.1016/j.measurement.2012.09.016.

[33] P. R. Bevington and D. K. Robinson. *Introduction to Linear Regression Analysis*. McGraw-Hill, 3rd edition, 2003. ISBN: 978-0072472271.

[34] A. Dean, D. Voss, and D. Draguljić. *Design and Analysis of Experiments*. Springer International Publishing, 2nd edition, 2017. ISBN: 978-3-319-52248-7.

[35] T. P. Rocha. Numerical and experimental study of wing tip endplates of a formula student car. Master's thesis, Instituto Superior Técnico, October 2020.

[36] J. D. A. Jr. *Fundamentals of Aerodynamics*. McGraw-Hill Education, 5th edition, 2011. ISBN: 978-0-07-339810-5.

Appendix A

Mechanical Design

Figure A.1(a) shows the nozzle of the Técnico wind tunnel. Figure A.1(b) shows a schematic representation of the nozzle and the corresponding dimensions, in cm. The grey parts are the foam wedges and the black part is a platform to support the force balance. Considering the growth of the shear layer from the nozzle exit, an effective 1m diameter uniform test section is expected.

(a) Nozzle of the wind tunnel.
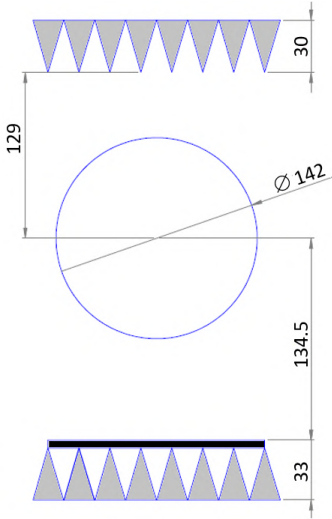
(b) Schematic representation of the nozzle.

Figure A.1: Nozzle of Técnico wind tunnel located in an anechoic chamber.

Figure A.2 shows the *NACA 4412* airfoil.
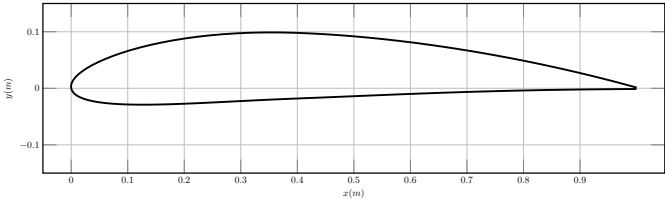
Figure A.2: Airfoil *NACA 4412* geometry.

Figure A.3 shows the response in C_l of *NACA 4412* airfoil to angles of attack from $-10°$ to $20°$, using XFLR5 v6.40 [17] as software.
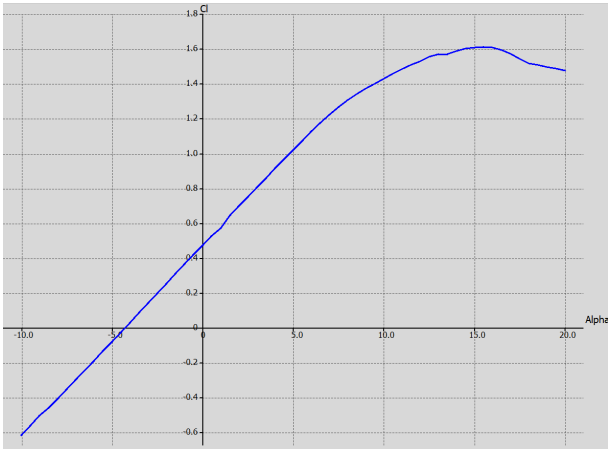
Figure A.3: Curve of $C_l-\alpha$ to *NACA 4412* airfoil.

The selected rod end bearings are made by *INA/FAG*: the *GAL8-UK* and *GAR8-UK*, being the former a rod end bearings with left male thread, and the latter a rod end bearing with a right male thread. Figure A.4 shows the CAD of this component, in which the light grey part corresponds to the spherical bearing with free rotation.
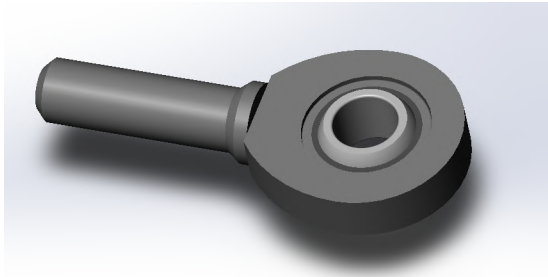
Figure A.4: *CAD* model of the rod end bearing.

The new convergence analysis to aircraft model force balance is presented in Figure A.5, and expose the total strain energy and time evolution throughout the refinement of mesh.
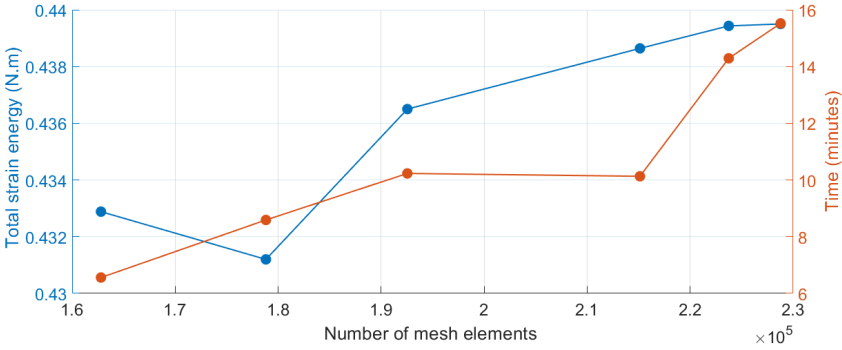
Figure A.5: Convergence validation to the new aircraft model force balance.

Figure A.6 shows the distance in X and Y coordinates of the interceptions of the six sensing bars with the moving platform.
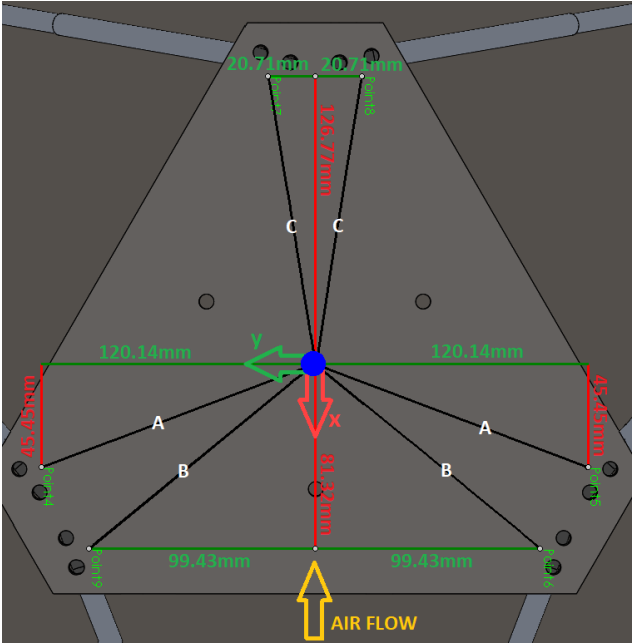
Figure A.6: Decomposition in X and Y coordinates of the six new sensing bars to compute moments.

Appendix B

Technical Drawings

In this appendix are present the technical drawings of all the parts of the force balance, as well as the corresponding dimensions. The previous Moving Platform is not presented due to the thickness of $5mm$ instead of $10mm$ being the only change compared to the New Moving Platform.

FixedPlatform

Coupler

New MovingPlatform

Ø6,60
Ø6,60
17,13
14,56
Ø110
60
230
60
24,51
11,65
Ø6,60
290

51,96
199,19
10
251,15

	NAME	SIGNATURE	DATE		TITLE:
DRAWN	André Oliveira		30/01/2020		
CHK'D					New MovingPlatform
APPV'D					
MFG					
Q.A			MATERIAL:	DWG NO.	

UNLESS OTHERWISE SPECIFIED:
DIMENSIONS ARE IN MILLIMETERS
SURFACE FINISH:
TOLERANCES:
  LINEAR:
  ANGULAR:
FINISH:
DEBURR AND BREAK SHARP EDGES
DO NOT SCALE DRAWING
REVISION

MATERIAL: Aluminium
DWG NO. 4
A4
SCALE:1:5   SHEET 1 OF 1

SensingBar

335

Ø10   Ø7

UNLESS OTHERWISE SPECIFIED:
DIMENSIONS ARE IN MILLIMETERS
SURFACE FINISH:
TOLERANCES:
  LINEAR:
  ANGULAR:
FINISH:
DEBURR AND BREAK SHARP EDGES
DO NOT SCALE DRAWING
REVISION

	NAME	SIGNATURE	DATE		TITLE:
DRAWN	André Oliveira		30/01/2020		SensingBar

MATERIAL: Aluminium
DWG NO. 6
A4
SCALE:1:2   SHEET 1 OF 1

NewSensingBar

335,00
117,50
100,00
117,50
Ø9,00
Ø10,00
Ø7,00

UNLESS OTHERWISE SPECIFIED:
DIMENSIONS ARE IN MILLIMETERS
SURFACE FINISH:
TOLERANCES:
  LINEAR:
  ANGULAR:
FINISH:
DEBURR AND BREAK SHARP EDGES
DO NOT SCALE DRAWING
REVISION

	NAME	SIGNATURE	DATE		TITLE:
DRAWN	André Oliveira		30/01/2020		NewSensingBar

MATERIAL: Aluminium
DWG NO. 6
A4
SCALE:1:2   SHEET 1 OF 1

Table

166
50
42,50
600
Ø5
Ø5
Ø8
Ø8
Ø399,50
Ø439
600
10

UNLESS OTHERWISE SPECIFIED:
DIMENSIONS ARE IN MILLIMETERS
SURFACE FINISH:
TOLERANCES:
  LINEAR:
  ANGULAR:
FINISH:
DEBURR AND BREAK SHARP EDGES
DO NOT SCALE DRAWING
REVISION

	NAME	SIGNATURE	DATE		TITLE:
DRAWN	André Oliveira		30/01/2020		Table

MATERIAL: Steel
DWG NO. 8
A4
SCALE:1:10   SHEET 1 OF 1

Drawing 1 (top-left): Flange

Ø 52
Ø 130
Ø 6,60
Ø 32
8
M5 Flat head
35

	NAME	SIGNATURE	DATE		TITLE:	
DRAWN	André Oliveira		30/01/2020			Flange
CHK'D						
APPV'D						
MFG						
Q.A						

UNLESS OTHERWISE SPECIFIED:
DIMENSIONS ARE IN MILLIMETERS
SURFACE FINISH:
TOLERANCES:
LINEAR:
ANGULAR:
FINISH:
DEBURR AND BREAK SHARP EDGES
DO NOT SCALE DRAWING
REVISION
MATERIAL: Aluminium
DWG NO. 9
A4
WEIGHT:
SCALE:1:2
SHEET 1 OF 1

Drawing 2 (top-right): NewFlange

Ø 6,60
Ø 32.00
Ø 100.00
Ø 130.00
Ø 52.00
50.00
35.00
10.00

	NAME	SIGNATURE	DATE		TITLE:	
DRAWN	André Oliveira		30/01/2020			NewFlange
CHK'D						
APPV'D						
MFG						
Q.A						

MATERIAL: Aluminium
DWG NO. 9
A4
SCALE:1:2
SHEET 1 OF 1

Drawing 3 (bottom-left): Strut(aircraft)

400
Ø 20
Ø 32

	NAME	SIGNATURE	DATE		TITLE:	
DRAWN	André Oliveira		30/01/2020			Strut(aircraft)
CHK'D						
APPV'D						
MFG						
Q.A						

MATERIAL: Aluminium
DWG NO. 10
A4
SCALE:1:2
SHEET 1 OF 1

Drawing 4 (bottom-right): Strut(half-wing)

130
Ø 32
Ø 20

	NAME	SIGNATURE	DATE		TITLE:	
DRAWN	André Oliveira		30/01/2020			Strut(half-wing)
CHK'D						
APPV'D						
MFG						
Q.A						

MATERIAL: Aluminium
DWG NO. 10
A4
SCALE:1:2
SHEET 1 OF 1

Drawing 1 — NewStrut(aircraft)

400

Ø 25   Ø 32

UNLESS OTHERWISE SPECIFIED:
DIMENSIONS ARE IN MILLIMETERS
SURFACE FINISH:
TOLERANCES:
   LINEAR:
   ANGULAR:

FINISH: | DEBURR AND BREAK SHARP EDGES | DO NOT SCALE DRAWING | REVISION

	NAME	SIGNATURE	DATE		TITLE:
DRAWN	André Oliveira		30/01/2020		**NewStrut(aircraft)**
CHK'D					
APPV'D					
MFG					
Q.A			MATERIAL: Aluminium	DWG NO. 10	A4

SCALE:1:2   SHEET 1 OF 1

Drawing 2 — NewStrut(half-wing)

130

Ø 25   Ø 32

UNLESS OTHERWISE SPECIFIED:
DIMENSIONS ARE IN MILLIMETERS
SURFACE FINISH:
TOLERANCES:
   LINEAR:
   ANGULAR:

FINISH: | DEBURR AND BREAK SHARP EDGES | DO NOT SCALE DRAWING | REVISION

	NAME	SIGNATURE	DATE		TITLE:
DRAWN	André Oliveira		30/01/2020		**NewStrut(half-wing)**
CHK'D					
APPV'D					
MFG					
Q.A			MATERIAL: Aluminium	DWG NO. 10	A4

SCALE:1:2   SHEET 1 OF 1

Drawing 3 — alphaAdjustment_1

Ø9   36   36   5   5   Ø9   30   45

UNLESS OTHERWISE SPECIFIED:
DIMENSIONS ARE IN MILLIMETERS
SURFACE FINISH:
TOLERANCES:
   LINEAR:
   ANGULAR:

FINISH: | DEBURR AND BREAK SHARP EDGES | DO NOT SCALE DRAWING | REVISION

	NAME	SIGNATURE	DATE		TITLE:
DRAWN	André Oliveira		30/01/2020		**alphaAdjustment_1**
CHK'D					
APPV'D					
MFG					
Q.A			MATERIAL: Aluminium	DWG NO. 11	A4

SCALE:1:1   SHEET 1 OF 1

Drawing 4 — alphaAdjustment_2

Ø9   26   31   5   Ø9   25   40

UNLESS OTHERWISE SPECIFIED:
DIMENSIONS ARE IN MILLIMETERS
SURFACE FINISH:
TOLERANCES:
   LINEAR:
   ANGULAR:

FINISH: | DEBURR AND BREAK SHARP EDGES | DO NOT SCALE DRAWING | REVISION

	NAME	SIGNATURE	DATE		TITLE:
DRAWN	André Oliveira		30/01/2020		**alphaAdjustment_2**
CHK'D					
APPV'D					
MFG					
Q.A			MATERIAL: Aluminium	DWG NO. 12	A4

SCALE:2:1   SHEET 1 OF 1

Appendix C

Technical Datasheets

C.1 Strain Gauges *1-LY13-6/350*

Specifications

Strain gage design

Carrier		Foil SG with embedded measuring grid
Material		Polyimide
Thickness	µm	50 ±15
Measuring grid		
Material		Constantan
Thickness	µm	approx. 3.8 or 5 (depending on SG type)
Covering		
Material		Polyimide
Thickness	µm	25 ±12
Connections		
Leads		Nickel-plated copper leads, 30 mm long
Integrated solder tabs		Size approx. 1.5 mm x 1.6 mm (depending on type)
Solder tabs with strain relief		Nickel-plated copper solder tabs
Nominal (rated) resistance	Ω	120, 350, 700 or 1000 (depending on SG type)
Resistance tolerance[1]	%	±0.3 without, ±0.35 with leads
Gage factor		approx. 2 (specified on each package)
Gage factor tolerance	%	±1.5 (with measuring grid length ≤1.5 mm) ±1.0 (with measuring grid length ≥3mm)
Temperature coefficient of the gage factor		Specified on each package
Transverse sensitivity	%	Specified on each package
Application temperature range	°C (°F)	-70 … +200 (-94 … +392) for static measurements -200 … +200 (-328 … +392) for dynamic measurements

Temperature response

	Code:	
α for ferritic steel	(1)	10.8 (6.0)
α for aluminum	(3)	23 (12.8)
α for austenitic steel	(5)	16 (8.9)
α for silica/composite	(6)	0.5 (0.3)
α for titanium	(7)	9 (5.0)
α for plastic	(8)	65 (36.1)
α for molybdenum	(9)	5.4 (3.0)
	ppm/K (ppm/°F)	

Maximum elongation

Positive direction	µm/m	Up to a maximum zero drift of +/- 30µm/m
Negative direction	µm/m	Up to a maximum zero drift of ±100µm/m
Fatigue life[2]		10⁶ load cycles at ±1,000 µm/m

Fatigue life[2]	
	10^6 load cycles at ±1,000 µm/m
	10^7 load cycles at ±1,000 µm/m
	10^4 load cycles at ±1,200 µm/m
	10^4 load cycles at ±2,200 µm/m
	10^2 load cycles at ±3,500 µm/m
	10^7 load cycles at ±1,000 µm/m

Minimum radius of curvature	0.3 mm for SG with leads 0.3 mm for SG with integrated solder tabs in measuring grid area 2.0 mm in solder tab area
Applicable adhesives	Z70, X60, X280, EP150 and EP310S

1) With measuring grid lengths of 0.3 and 0.6 mm, the nominal resistance may deviate by ± 1%. For XY9x, RY9x and the KY types (per chain) it is ±0.5%. ±0.75%. For XY9x, RY9x and the KY types (per chain) it is ±0.5%.
2) The data depend on the various parameters of the specific application and are therefore stated for representative examples only.

Series Y: LY1

Linear strain gage with leads below the measuring grid

Ordering number[1]	Pcs. per pack	Nominal (rated) resistance Ω	Dimensions [mm]				Vmax[3]	Solder terminals	Pre-ferred types[4]
			Measuring grid a	b	Carrier c	d			
1-LY1☐-0,3/120A[2]	10	120	0,3	0,9	2	1,2	0,6	LS7	1
1-LY1☐-0,6/120[2]	10	120	0,6	1	5	3,2	1,5	LS7	1,3
1-LY1☐-1,5/120	10	120	1,5	1,2	6,5	4,7	2,5	LS7	1,3
1-LY1☐-3/120	10	120	3	1,6	8,5	4,5	4	LS7	1,3
1-LY1☐-3/120A[5]	10	120	3	1,6	8,5	4,5	4	LS7	1,3
1-LY1☐-6/120	10	120	6	2,7	13	6	8	LS7	1,3
1-LY1☐-6/120A[5]	10	120	6	2,7	13	6	8	LS5	1
1-LY1☐-10/120	10	120	10	4,6	18,5	9,5	13	LS5	1
1-LY1☐-10/120A[5]	10	120	10	4,6	18,5	9,5	13	LS5	1
1-LY1☐-1,5/350[2]	10	350	1,5	1,2	5,7	4,5	4,5	LS7	1,3
1-LY1☐-3/350	10	350	3	1,6	8,5	4,5	7	LS7	1,3
1-LY1☐-3/350A[5]	10	350	3	1,6	8,5	4,5	7	LS7	-
1-LY1☐-6/350A[5]	10	350	6	2,8	13	6	13	LS5	1
1-LY1☐-6/350	10	350	6	2,8	13	6	13	LS5	-
1-LY1☐-10/350	10	350	10	5,0	18,5	9,5	23	LS5	1
1-LY1☐-10/350A[5]	10	350	10	5,0	18,5	9,5	23	LS5	-

Series Y: LY2

Linear strain gage with leads on both sides of the measuring grid

Ordering number[1]	Pcs. per pack	Nominal (rated) resistance Ω	Dimensions [mm]				Vmax[3]	Solder terminals	Pre-ferred types[4]
			Measuring grid a	b	Carrier c	d			
1-LY2☐-0,6/120[2]	10	120	0,6	0,6	3,5	6,4	1	LS7	1
1-LY2☐-1,5/120	10	120	1,5	1,5	4,7	8,3	2	LS5	-
1-LY2☐-3/120	10	120	3	2,8	7,5	10	6	LS5	1
1-LY2☐-6/120	10	120	6	6	11	16	12	LS4	-

1) Strain gages are available in various temperature matches (see codes, page 3). Insert the code in place of the placeholder "☐" to get the ordering number of the strain gage you need.
2) Only available in matches for aluminum, ferritic and austenitic steel
3) Maximum permissible effective supply voltage (specified for steel)
4) Preferred types (available from stock) with the temperature matches specified in the column
5) With application aid (cut-to-size polyimide adhesive strip for easy positioning)

C.2   Pressure Sensor *MPXV7002DP*

MPXV7002 Integrated Silicon Pressure Sensor On-Chip Signal Conditioned, Temperature Compensated and Calibrated

The MPXV7002 series piezoresistive transducers are state-of-the-art monolithic silicon pressure sensors designed for a wide range of applications, but particularly those employing a microcontroller or microprocessor with A/D inputs. This transducer combines advanced micromachining techniques, thin-film metallization, and bipolar processing to provide an accurate, high level analog output signal that is proportional to the applied pressure.

Features
*   2.5% Typical Error over +10°C to +60°C with Auto Zero
*   6.25% Maximum Error over +10°C to +60°C without Auto Zero
*   Ideally Suited for Microprocessor or Microcontroller-Based Systems
*   Thermoplastic (PPS) Surface Mount Package
*   Temperature Compensated over +10° to +60°C
*   Patented Silicon Shear Stress Strain Gauge
*   Available in Differential and Gauge Configurations

MPXV7002
-2 to +2 kPa (-0.3 to +0.3 psi)
0.5 to 4.5 V Output
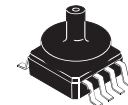
**MPXV7002GC6U/C6T1
CASE 482A**
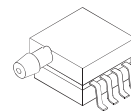
**MPXV7002GP
CASE 1369**
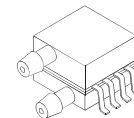
**MPXV7002DP
CASE 1351**

Small Outline Package

Top view

N/C	5	4	V_{OUT}
N/C	6	3	GND
N/C	7	2	V_S
N/C	8	1	N/C
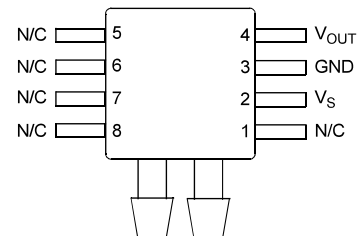
**Pinout
(Style 2, case number 98ASA99255D)**

ORDERING INFORMATION									
Device Name	Package Options	Case No.	# of Ports			Pressure Type			Device Marking
			None	Single	Dual	Gauge	Differential	Absolute	
Small Outline Package (MPXV7002 Series)									
MPXV7002GC6U	Rails	482A		•		•			MPXV7002G
MPXV7002GC6T1	Tape & Reel	482A		•		•			MPXV7002G
MPXV7002GP	Trays	1369		•		•			MPXV7002G
MPXV7002DP	Trays	1351			•		•		MPXV7002DP
MPXV7002DPT1	Tape & Reel	1351			•		•		MPXV7002DP

1 Operating Characteristics

Table 1. Operating Characteristics (V_S = 5.0 Vdc, T_A = 25°C unless otherwise noted. Decoupling circuit shown in Figure 3 required to meet specification.)

Characteristic		Symbol	Min	Typ	Max	Unit
Pressure Range[1]		P_{OP}	−2.0	—	2.0	kPa
Supply Voltage[2]		V_S	4.75	5.0	5.25	Vdc
Supply Current		I_o	—	—	10	mAdc
Pressure Offset[3] @ V_S = 5.0 Volts	(10 to 60°C)	V_{off}	0.25	0.5	0.75	Vdc
Full Scale Output[4] @ V_S = 5.0 Volts	(10 to 60°C)	V_{FSO}	4.25	4.5	4.75	Vdc
Full Scale Span[5] @ V_S = 5.0 Volts	(10 to 60°C)	V_{FSS}	3.5	4.0	4.5 V	Vdc
Accuracy[6]	(10 to 60°C)	—	—	±2.5[7]	±6.25	%V_{FSS}
Sensitivity		V/P	—	1.0	—	V/kPa
Response Time[8]		t_R	—	1.0	—	ms
Output Source Current at Full Scale Output		I_{o+}	—	0.1	—	mAdc
Warm-Up Time[9]		—	—	20	—	ms

1. 1.0 kPa (kiloPascal) equals 0.145 psi.
2. Device is ratiometric within this specified excitation range.
3. Offset (V_{off}) is defined as the output voltage at the minimum rated pressure.
4. Full Scale Output (V_{FSO}) is defined as the output voltage at the maximum or full rated pressure.
5. Full Scale Span (V_{FSS}) is defined as the algebraic difference between the output voltage at full rated pressure and the output voltage at the minimum rated pressure.
6. Accuracy (error budget) consists of the following:

   Linearity: Output deviation from a straight line relationship with pressure over the specified pressure range.

   Temperature Hysteresis: Output deviation at any temperature within the operating temperature range, after the temperature is cycled to and from the minimum or maximum operating temperature points, with zero differential pressure applied.

   Pressure Hysteresis: Output deviation at any pressure within the specified range, when this pressure is cycled to and from the minimum or maximum rated pressure, at 25°C.

   TcSpan: Output deviation over the temperature range of 10° to 60°C, relative to 25°C.

   TcOffset: Output deviation with minimum rated pressure applied, over the temperature range of 10° to 60°C, relative to 25°C.

   Variation from Nominal: The variation from nominal values, for Offset or Full Scale Span, as a percent of V_{FSS}, at 25°C.
7. Auto Zero at Factory Installation: Due to the sensitivity of the MPXV7002 Series, external mechanical stresses and mounting position can affect the zero pressure output reading. Auto zero is defined as storing the zero pressure output reading and subtracting this from the device's output during normal operations. Reference AN1636 for specific information. The specified accuracy assumes a maximum temperature change of ± 5°C between auto zero and measurement.
8. Response Time is defined as the time for the incremental change in the output to go from 10% to 90% of its final value when subjected to a specified step change in pressure.
9. Warm-up Time is defined as the time required for the product to meet the specified output voltage after the Pressure has been stabilized.

4 Pressure (P1)/Vacuum (P2) Side Identification Table

NXP designates the two sides of the pressure sensor as the Pressure (P1) side and the Vacuum (P2) side. The Pressure (P1) side is the side containing a gel die coat which protects the die from harsh media.

The Pressure (P1) side may be identified by using the following table:

Part Number	Case Type	Pressure (P1) Side Identifier
MPXV7002GC6U/GC6T1	482A-01	Side with Port Attached
MPXV7002GP	1369-01	Side with Port Attached
MPXV7002DP	1351-01	Side with Part Marking

Figure 4. Output versus Pressure Differential

Transfer Function:
$V_{out} = V_S \times (0.2 \times P(kPa)+0.5) \pm 6.25\% V_{FSS}$
V_S = 5.0 Vdc
T_A = 10 to 60°C

5 Minimum Recommended Footprint for Surface Mounted Applications

Surface mount board layout is a critical portion of the total design. The footprint for the surface mount packages must be the correct size to ensure proper solder connection interface between the board and the package. With the correct footprint, the packages will self align when subjected to a solder reflow process. It is always recommended to design boards with a solder mask layer to avoid bridging and shorting between solder pads.
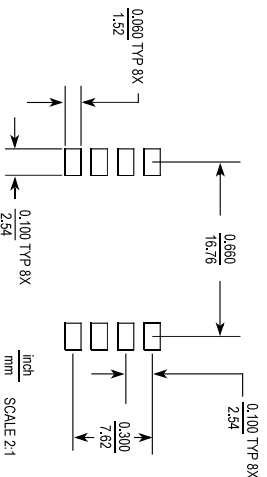
Figure 5. Small Outline Package Footprint

Appendix D

Sensing Bar Strain Gauge System Calibration

This appendix contains the strain data for the load set to calibrate the sensing bar strain gauge system. It is presented the complete output provided by DAQ and the adjustment analyses made for each sensing bar.

(a) Strain response for the complete load set.

(b) Force for average strain response.

Figure D.1: Sensing bar # 1

(a) Strain response for the complete load set.
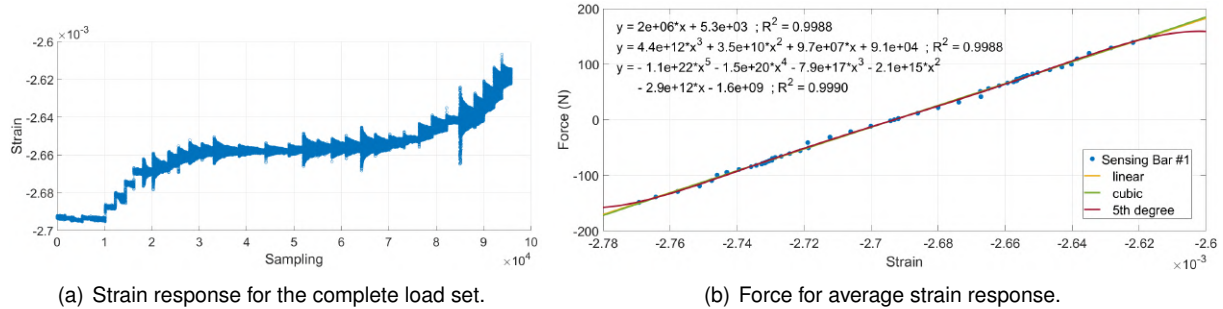
(b) Force for average strain response.

Figure D.2: Sensing bar # 2

(a) Strain response for the complete load set.
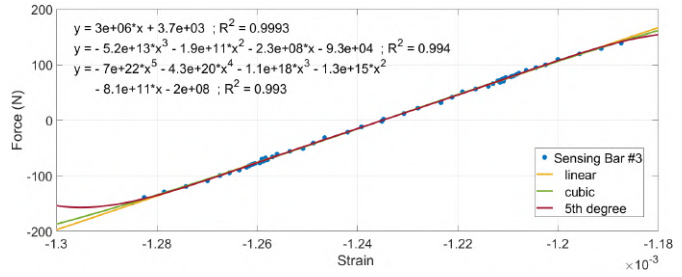
(b) Force for average strain response.

Figure D.3: Sensing bar # 3
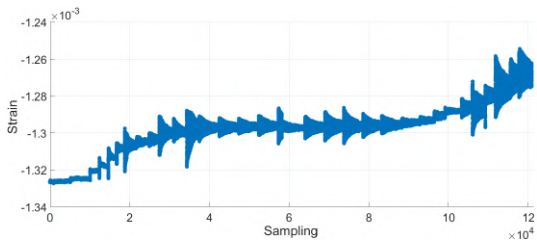
(a) Strain response for the complete load set.
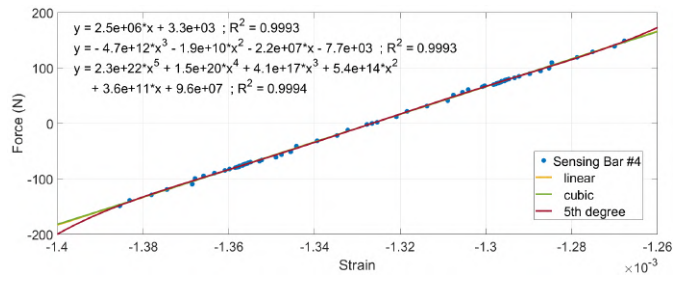
(b) Force for average strain response.

Figure D.4: Sensing bar # 4
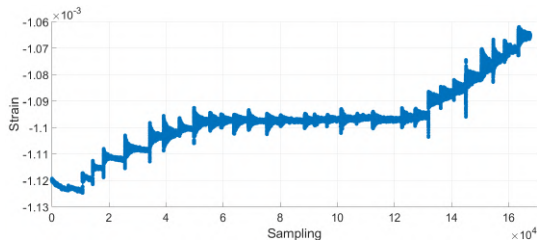
(a) Strain response for the complete load set.
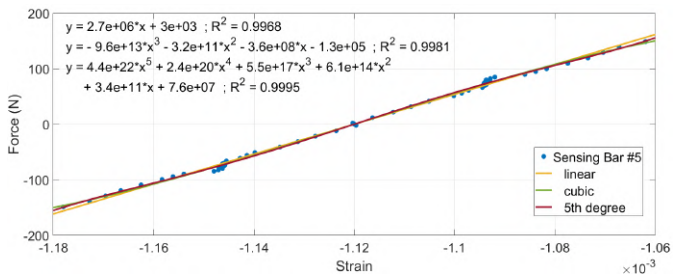
(b) Force for average strain response.

Figure D.5: Sensing bar # 5
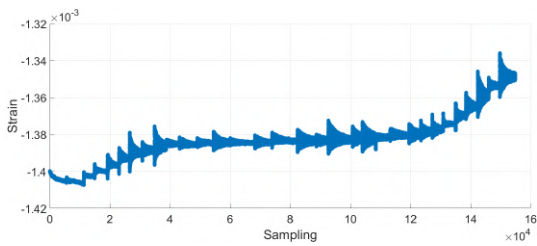
(a) Strain response for the complete load set.
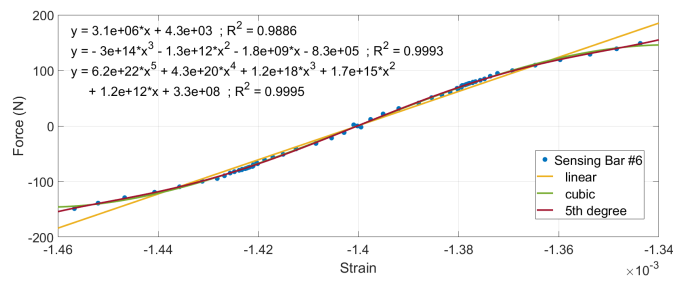
(b) Force for average strain response.

Figure D.6: Sensing bar # 6

Appendix E

Calibration

E.1 Weighted Scheme Matrices

Matrix V_R

$$V_R = \begin{bmatrix} u_{r_{1,1};r_{1,1}} & u_{r_{1,1};r_{1,2}} & \cdots & u_{r_{1,1};r_{1,N}} & u_{r_{1,1};r_{2,1}} & \cdots & u_{r_{1,1};r_{6,N}} \\ \vdots & \vdots & \ddots & \vdots & \vdots & \ddots & \vdots \\ u_{r_{1,N};r_{1,1}} & u_{r_{1,N};r_{1,2}} & \cdots & u_{r_{1,N};r_{1,N}} & u_{r_{1,N};r_{2,1}} & \cdots & u_{r_{1,N};r_{6,N}} \\ u_{r_{2,1};r_{1,1}} & u_{r_{2,1};r_{1,2}} & \cdots & u_{r_{2,1};r_{1,N}} & u_{r_{2,1};r_{2,1}} & \cdots & u_{r_{2,1};r_{6,N}} \\ \vdots & \vdots & \ddots & \vdots & \vdots & \ddots & \vdots \\ u_{r_{6,N};r_{1,1}} & u_{r_{6,N};r_{1,2}} & \cdots & u_{r_{6,N};r_{1,N}} & u_{r_{6,N};r_{2,1}} & \cdots & u_{r_{6,N};r_{6,N}} \end{bmatrix} \tag{E.1}$$

Matrix D

$$D = \begin{bmatrix} \frac{\partial f_{1,1}}{\partial R_{1,1}} & \frac{\partial f_{1,1}}{\partial R_{1,2}} & \cdots & \frac{\partial f_{1,1}}{\partial R_{1,N}} & \frac{\partial f_{1,1}}{\partial R_{2,1}} & \cdots & \frac{\partial f_{1,1}}{\partial R_{6,N}} \\ \frac{\partial f_{1,2}}{\partial R_{1,1}} & \frac{\partial f_{1,2}}{\partial R_{1,2}} & \cdots & \frac{\partial f_{1,2}}{\partial R_{1,N}} & \frac{\partial f_{1,2}}{\partial R_{2,1}} & \cdots & \frac{\partial f_{1,2}}{\partial R_{6,N}} \\ \vdots & \vdots & \ddots & \vdots & \vdots & \ddots & \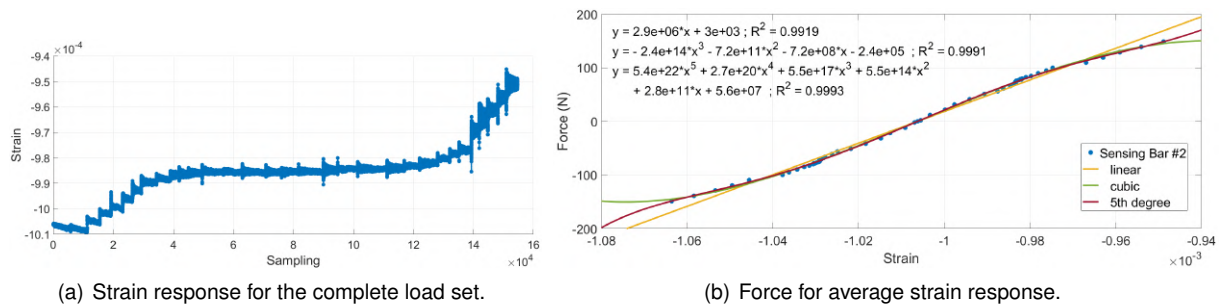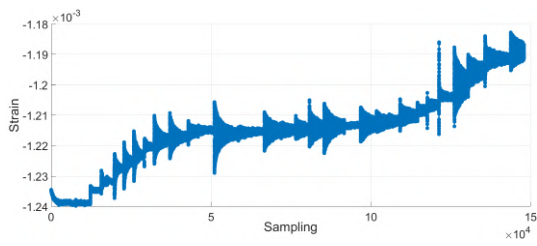vdots \\ \frac{\partial f_{1,N-1}}{\partial R_{1,1}} & \frac{\partial f_{1,N-1}}{\partial R_{1,2}} & \cdots & \frac{\partial f_{1,N-1}}{\partial R_{1,N}} & \frac{\partial f_{1,N-1}}{\partial R_{2,1}} & \cdots & \frac{\partial f_{1,N-1}}{\partial R_{6,N}} \\ \frac{\partial f_{1,N}}{\partial R_{1,1}} & \frac{\partial f_{1,N}}{\partial R_{1,2}} & \cdots & \frac{\partial f_{1,N}}{\partial R_{1,N}} & \frac{\partial f_{1,N}}{\partial R_{2,1}} & \cdots & \frac{\partial f_{1,N}}{\partial R_{6,N}} \end{bmatrix}. \tag{E.2}$$

E.2 Calibration Loading values

Table E.1: Applied calibration loads.

No.	F_X [N]	F_Y [N]	F_Z [N]	M_X [N.m]	M_Y [N.m]	M_Z [N.m]
1	0	0	0	0	0	0
2	9.82	0	0	0	0	0
3	19.64	0	0	0	0	0
4	36.81	0	0	0	0	0
5	54.01	0	0	0	0	0
6	98.19	0	0	0	0	0
7	142.4	0	0	0	0	0
8	193.34	0	0	0	0	0
9	239.44	0	0	0	0	0
10	339.5	0	0	0	0	0
11	438.58	0	0	0	0	0
12	0	0	0	0	0	0
13	0	12.61	0	0	0	0
14	0	22.43	0	0	0	0
15	0	39.6	0	0	0	0
16	0	56.8	0	0	0	0
17	0	100.98	0	0	0	0
18	0	145.19	0	0	0	0
19	0	196.13	0	0	0	0
20	0	242.23	0	0	0	0
21	0	342.29	0	0	0	0
22	0	441.37	0	0	0	0
23	0	0	0	0	0	0
24	0	0	12.61	0	0	0
25	0	0	22.43	0	0	0
26	0	0	39.6	0	0	0
27	0	0	56.8	0	0	0
28	0	0	100.98	0	0	0
29	0	0	145.19	0	0	0
30	0	0	196.13	0	0	0
31	0	0	242.23	0	0	0
32	0	0	342.29	0	0	0
33	0	0	441.37	0	0	0
34	0	0	0	0	0	0
35	0	0	12.61	3.783	0	0
36	0	0	22.43	6.729	0	0
37	0	0	39.6	11.88	0	0
38	0	0	56.8	17.04	0	0
39	0	0	100.98	30.294	0	0
40	0	0	145.19	43.557	0	0
41	0	0	196.13	58.839	0	0
42	0	0	242.23	72.669	0	0
43	0	0	0	0	0	0
44	0	0	12.61	-3.783	0	0
45	0	0	22.43	-6.729	0	0
46	0	0	39.6	-11.88	0	0
47	0	0	56.8	-17.04	0	0
48	0	0	100.98	-30.294	0	0
49	0	0	145.19	-43.557	0	0
50	0	0	196.13	-58.839	0	0
51	0	0	242.23	-72.669	0	0
52	0	0	0	0	0	0
53	0	0	12.61	0	3.783	0
54	0	0	22.43	0	6.729	0
55	0	0	39.6	0	11.88	0
56	0	0	56.8	0	17.04	0
57	0	0	100.98	0	30.294	0
58	0	0	145.19	0	43.557	0
59	0	0	196.13	0	58.839	0
60	0	0	242.23	0	72.669	0
61	0	0	0	0	0	0
62	0	0	12.61	0	-3.783	0
63	0	0	22.43	0	-6.729	0
64	0	0	39.6	0	-11.88	0
65	0	0	56.8	0	-17.04	0
66	0	0	100.98	0	-30.294	0
67	0	0	145.19	0	-43.557	0
68	0	0	196.13	0	-58.839	0
69	0	0	242.23	0	-72.669	0
70	0	0	0	0	0	0
71	-12.61	0	0	0	0	3.783
72	-22.43	0	0	0	0	6.729
73	-39.6	0	0	0	0	11.88
74	-56.8	0	0	0	0	17.04
75	-100.98	0	0	0	0	30.294
76	-145.19	0	0	0	0	43.557
77	-196.13	0	0	0	0	58.839
78	-242.23	0	0	0	0	72.669
79	0	0	0	0	0	0
80	-12.61	0	0	0	0	-3.783
81	-22.43	0	0	0	0	-6.729
82	-39.6	0	0	0	0	-11.88
83	-56.8	0	0	0	0	-17.04
84	-100.98	0	0	0	0	-30.294
85	-145.19	0	0	0	0	-43.557
86	-196.13	0	0	0	0	-58.839
87	-242.23	0	0	0	0	-72.669

E.3 Coefficients Matrix

$$C = \begin{bmatrix}
-0,617896 & 0,090931 & -1,238098 & -0,088204 & -0,229695 & 0,167224 \\
-0,133195 & 0,043550 & -1,538156 & 0,064625 & -0,032167 & 0,049581 \\
-0,341969 & 0,604012 & 0,722658 & -0,125678 & -0,002230 & -0,122717 \\
1,031359 & 0,628751 & -1,291951 & -0,296026 & 0,157145 & -0,050662 \\
-0,417295 & -0,551995 & -0,338450 & 0,276612 & -0,116642 & 0,038810 \\
0,267929 & -0,206126 & -0,038862 & 0,022595 & 0,194066 & -0,121846 \\
0,007431 & -0,002294 & -0,001745 & 0,000915 & 0,002072 & 0,000283 \\
0,014491 & -0,002948 & -0,020001 & 0,001619 & 0,005949 & 0,004447 \\
-0,009551 & -0,006129 & 0,010938 & 0,002370 & -0,003513 & -0,003574 \\
-0,001851 & -0,002975 & -0,003176 & 0,002770 & -0,000850 & -0,001443 \\
0,004779 & -0,001367 & -0,005669 & -0,001192 & 0,001949 & 0,002711 \\
-0,002660 & 0,002272 & -0,008151 & -0,000878 & -0,000200 & 0,002115 \\
0,000111 & 0,000649 & -0,005462 & -0,000132 & 0,000402 & 0,001170 \\
0,008948 & 0,001288 & 0,020209 & -0,000800 & 0,003672 & -0,002979 \\
0,024988 & 0,007164 & -0,015351 & -0,001826 & 0,009673 & 0,003248 \\
-0,018722 & -0,007151 & 0,013681 & 0,002275 & -0,006861 & -0,002794 \\
-0,012974 & 0,000266 & 0,016112 & -0,000111 & -0,004573 & -0,003309 \\
-0,010990 & -0,007112 & -0,017253 & 0,003303 & -0,005390 & 0,002319 \\
-0,021282 & -0,010796 & 0,019081 & 0,003465 & -0,008854 & -0,003799 \\
0,026341 & 0,010003 & -0,035898 & -0,002827 & 0,009567 & 0,006347 \\
0,009073 & 0,003488 & -0,013879 & -0,001473 & 0,002394 & 0,003471 \\
0,001003 & -0,002008 & -0,001469 & 0,001123 & 0,000127 & -0,000719 \\
-0,000186 & 0,004167 & 0,009605 & -0,002402 & 0,000413 & 0,000890 \\
-0,001286 & -0,005498 & 0,005422 & 0,001400 & -0,000653 & 0,000423 \\
-0,001898 & -0,001831 & -0,004560 & 0,000924 & -0,001420 & -0,001150 \\
-0,006707 & 0,008181 & 0,008594 & -0,002857 & -0,002686 & -0,003020 \\
-0,000170 & 0,000569 & 0,004413 & -0,000300 & -0,000166 & -0,001171
\end{bmatrix} \quad \text{(E.3)}$$

E.4 Fitting Values for the Calibration Loading

Table E.2: Fitting values $\hat{F}$.

No.	F_X [N]	F_Y [N]	F_Z [N]	M_X [N.m]	M_Y [N.m]	M_Z [N.m]	No.	F_X [N]	F_Y [N]	F_Z [N]	M_X [N.m]	M_Y [N.m]	M_Z [N.m]
1	-0.55	2.26	-1.11	-0.73	-0.09	0.01	44	1.44	1.41	15.25	-4.30	0.45	-0.22
2	11.44	-0.25	1.22	0.12	-0.18	0.60	45	0.73	1.11	24.30	-6.58	0.41	-0.13
3	20.50	-1.59	0.35	0.89	-0.32	0.87	46	0.03	-1.62	47.58	-10.82	-0.20	-0.54
4	36.56	-4.62	0.84	2.09	-0.70	0.80	47	1.54	-3.26	61.31	-15.31	0.49	0.02
5	55.30	-7.18	1.33	3.20	-0.95	0.41	48	5.44	-2.41	104.84	-28.95	1.56	0.79
6	99.81	-5.88	8.11	2.06	-2.08	-1.56	49	4.54	-1.65	150.95	-42.46	0.76	0.35
7	142.77	-2.59	12.67	0.62	-3.07	-2.41	50	8.53	-0.62	203.22	-58.23	1.87	0.20
8	195.11	1.81	4.85	-0.23	-1.19	0.33	51	3.24	-0.41	251.93	-71.96	0.20	-0.03
9	237.69	-0.69	8.86	1.41	-0.24	0.68	52	-0.72	2.21	-0.46	-0.75	-0.17	0.07
10	319.48	-2.15	12.88	2.33	-2.25	0.94	53	-3.27	1.05	17.11	-0.28	2.65	-0.77
11	423.04	-1.20	17.04	2.17	-2.84	-0.18	54	-6.21	-1.84	28.30	0.80	4.52	-0.80
12	-0.59	2.23	-2.25	-0.70	-0.14	0.08	55	-12.86	-2.89	42.27	1.58	7.33	-0.24
13	0.08	6.70	-0.01	1.30	-0.78	0.04	56	-15.59	-2.18	63.15	1.12	11.68	-0.61
14	0.08	13.12	-0.59	2.09	-1.06	0.17	57	-10.60	0.81	103.98	0.40	28.40	0.15
15	1.28	31.42	-2.78	2.11	-1.01	0.75	58	-1.81	1.08	143.15	-0.03	44.97	-0.05
16	0.51	52.21	-1.72	1.52	-1.01	0.78	59	-2.08	0.98	197.62	-0.09	59.58	0.16
17	-2.19	102.35	3.57	0.07	-0.53	-1.02	60	-2.22	-0.49	252.35	-0.08	72.00	-0.47
18	-3.20	146.73	8.78	-0.50	-0.53	-1.50	61	-0.47	2.22	-1.51	-0.72	-0.16	0.05
19	0.09	197.32	7.46	-0.69	-0.15	-0.19	62	2.42	1.22	11.97	-0.42	-3.17	0.99
20	6.97	240.50	-1.42	0.77	2.43	1.96	63	3.93	0.46	23.16	-0.44	-6.28	1.19
21	1.69	339.99	10.24	1.19	-0.29	-0.45	64	8.33	0.16	39.40	-0.28	-10.67	1.27
22	-2.68	445.21	2.92	-1.23	-1.95	0.25	65	11.57	-0.70	55.35	0.28	-15.26	1.49
23	-0.72	2.36	-1.60	-0.75	-0.20	0.05	66	14.45	-2.39	100.62	1.47	-28.52	1.25
24	-0.86	2.45	9.09	-0.75	-0.27	0.11	67	12.53	0.96	154.16	0.55	-43.22	-0.06
25	-0.58	2.20	20.03	-0.72	-0.24	0.13	68	16.08	-3.82	196.59	1.76	-57.63	1.29
26	-1.20	2.62	38.59	-0.81	-0.50	0.12	69	6.95	-0.06	246.80	0.38	-73.82	0.51
27	-1.22	2.78	57.20	-0.92	-0.67	0.00	70	-0.37	1.96	1.88	-0.73	-0.05	0.06
28	-3.54	3.79	103.21	-1.11	-1.55	-0.28	71	-15.35	-0.35	6.17	-0.04	-0.27	1.92
29	-3.42	2.58	146.52	-0.26	-1.29	0.06	72	-28.85	-1.86	11.15	0.77	-1.02	4.61
30	-2.16	0.51	195.40	1.08	-0.54	0.68	73	-49.77	-2.63	6.59	1.90	-0.55	12.20
31	-1.76	-0.85	240.67	2.14	0.15	1.05	74	-72.15	1.09	10.85	0.01	-1.96	17.13
32	-8.74	-0.35	346.48	2.10	-2.02	-0.36	75	-122.65	1.84	9.81	-0.40	-3.79	29.49
33	-7.02	-3.12	443.42	3.58	-1.87	0.08	76	-164.98	-1.40	14.72	1.06	-2.38	43.71
34	-0.58	2.37	-1.29	-0.77	-0.17	0.03	77	-207.18	0.53	13.66	0.91	-0.76	60.12
35	-0.55	0.47	13.30	3.56	0.12	0.39	78	-233.26	0.27	25.53	-0.37	1.22	71.63
36	1.00	-0.07	25.68	7.09	0.92	0.41	79	-0.89	2.36	-1.14	-0.76	-0.25	0.07
37	0.94	-1.38	42.72	12.77	0.75	0.29	80	-8.77	1.72	-3.12	-0.01	2.12	-2.22
38	-0.88	-1.01	58.32	17.73	0.04	0.39	81	-17.92	0.85	-6.84	0.47	2.00	-4.28
39	-5.25	-0.91	94.97	30.77	-1.73	0.80	82	-36.89	0.15	-4.52	0.21	2.29	-10.79
40	-6.15	1.81	134.71	43.10	-1.36	0.99	83	-53.24	-0.27	-0.62	-0.17	2.46	-16.67
41	0.29	-0.21	181.52	60.04	0.87	-0.86	84	-103.54	-0.26	9.67	-0.59	0.60	-31.43
42	10.21	-1.72	219.56	75.08	4.66	-0.41	85	-149.45	-1.37	7.35	0.00	0.46	-44.01
43	-0.48	2.20	-0.49	-0.77	-0.15	0.05	86	-199.79	1.57	0.79	-0.36	-0.03	-58.17
							87	-241.15	-1.51	2.83	0.71	0.12	-72.72